APPLIED COMPUTATIONAL ELECTROMAGNETICS SOCIETY JOURNAL

APRIL 2023 REVIEWERS

Rabah W. Aldhaheri
Guillaume Andrieu
Billel Bentouhami
Luigi Boccia
Syed Sabir Hussain Bukhari
Mahendran C.
Zaheer Ahmed Dayo
Zhai Fei
Nunzia Fontana
Nasr H. Gad
Anouk Hubrechsen
Pankaj Jha
Tarun Kumar
Brian LaRocca

Chenwei Li
Neng-Wu Liu
Zhong Longquan
Ali Madani Mohammadi
Antonino Musolino
Alfredo Gomes Neto
Jayakumar S.
Siva S. A.
Qurban Ali Shah
Junwen Tang
Wentao Yuan
Yun-Qi Zhang
Guang-Yu Zhu

THE APPLIED COMPUTATIONAL ELECTROMAGNETICS SOCIETY JOURNAL

TABLE OF CONTENTS

A Compact Circularly Polarized Crossed Dipole Antenna with Wide Bandwidth using Split Ring Resonator and Parasitic Patches

Hailong Yang, Zhiqiang Guo, Xuping Li, Yunqi Zhang, Xueyan Song, and Shanzhe Wang

School of Electronic Engineering

Xi'an University of Posts and Telecommunications, Xi'an, 710121, China

yanghl68@163.com, 1148958181@qq.com, lixuping@163.com, johnny_5@126.com, xysong6597@126.com, 14120032@bjtu.edu.cn

Abstract – A new compact broadband circularly polarized (CP) crossed dipole antenna using split ring resonator (SRR) and parasitic patches are presented. The proposed antenna is mainly composed of two orthogonal strip dipoles, two 90° phase delay lines, four SRRs, and four parasitic patches. The combination of the orthogonal strip dipoles and the delay lines forms a crossed dipole as the main CP radiator. The well-designed SRR can extend the current path and improve the current distribution of high-frequency without increasing the size of the antenna, thereby reducing the size of the antenna and increasing the axial ratio (AR) bandwidth of the high-frequency. The introduction of parasitic patches can improve the current distribution between the upper and lower cut-off frequency points of the bandwidth, and make up for the defects of the insufficient bandwidth of the crossed dipole and the SRR, thereby realizing broadband CP radiation. To verify the antenna, a physical prototype is fabricated. The measured results show that the impedance bandwidth (IBW) of 69.1% (1.38-2.84 GHz), and a wide AR bandwidth of 57.7% (1.43-2.59 GHz). In addition, the designed antenna achieves a stable gain in the working band and a certain band-edge selectivity. Such a single-fed, simple structure and the wideband CP antenna is an excellent candidate for communication systems such as ISM (2.4 GHz), WiBro (2.3-2.39 GHz) and Inmarsat.

Index Terms – Circularly Polarized (CP) antenna, crossed dipole, parasitic patches, Split Ring Resonator (SRR).

I. INTRODUCTION

Compared to linearly polarized antennas, circularly polarized (CP) antennas have received widespread attention due to their advantages of eliminating polarization mismatches and suppressing multipath interference. At the same time, there are no strict requirements for the direction of transmitting and receiving antennas, which can improve the flexibility between transmitting and receiving antennas. In recent years, with the development of miniaturization and integration of wireless communication systems, miniaturization and broadband CP antennas have attracted more and more attention.

The traditional CP crossed dipole antennas use a phase-delay ring to provide orthogonal phase and generate CP radiation [1]. The circumference of the ring is one-quarter of the waveguide wavelength corresponding to the center frequency, and its size is small and easy to design, with an axial ratio (AR) bandwidth of up to 15.6%. Although this bandwidth has a significant advantage over traditional circularly polarized patch antennas, it has only a single resonant mode, which is not competitive enough in modern wireless communication systems. There have been many papers [2]-[15] that have reported on further expanding the CP bandwidth of the crossed dipole antenna. In [2], Feng, et al. proposed a crossed dipole antenna loading an asymmetric cross-loop, and achieving a 53.4% CP bandwidth in the form of a multi-mode resonance. Similarly, by introducing structures such as parasitic magneto-electric dipoles [3], two parasitic patches [4], dual cavity [5], and parasitic modified patches [6], the bandwidths can reach 28.6%, 66%, 66.7%, and 72.7%, respectively. However, the introduction of the above-mentioned parasitic structures leads to an increase in the size of the antenna. In [7]-[10], by improving the early linear crossed dipoles, the rectangular crossed dipole [7], double bowtie crossed dipole [8], asymmetric bowtie crossed dipole [9], and L-shaped crossed dipole [10] are used. The matching of broadband is improved, and the final CP bandwidth reaches 27%, 26.3%, 51%, and 62.3%, respectively. In [11], a wideband and directional crossed dipole CP antenna is studied. By adding the parasitic patches and defecting the ground plane, the CP bandwidth is enhanced. In [12], the stepped dipole and L-shaped folded ground plate is designed to enhance the CP operation bandwidth of a crossed dipole antenna. Although, in [11] and [12], their CP bandwidths can reach 68.6% and 74.7%,

respectively, their sizes are 0.97 $\lambda_0 \times$ 0.97 λ_0 and 1.03 $\lambda_0 \times$ 1.03 λ_0, which is still relatively large. In [13] and [14], the size of the deformed crossed dipole antenna with four parasitic plates and the crossed dipole antenna using coupling stubs can reach 0.4 $\lambda_0 \times$ 0.4 λ_0 and 0.32 $\lambda_0 \times$ 0.32 λ_0, respectively. However, the CP bandwidths of these two antennas are only 52.6% and 45%, which is narrower than the antennas [11] and [12]. In [15], a wideband CP crossed dipole antenna with improved bandwidth and gain performance is presented. By designing parasitic elements, a cavity-backed reflector, and a circular ring reflector, good CP bandwidth and high gain are obtained. The size of the antenna in [15] is 0.6 λ_0 $\times$ 0.6 λ_0, and the CP bandwidth is 85.5%. Nevertheless, the structure of the antenna is complex and the assembly is difficult, which increases the difficulty of debugging the antenna. Therefore, it is of interest to design crossed dipole antennas with a simple structure, small size, and wide bandwidth.

In this paper, a crossed dipole antenna with a simple structure, small size, and wide CP bandwidth is proposed, and it has been validated in [16]. In this design, the well-designed SRR makes good use of its resonant properties to produce multiple resonant modes by coupling with the crossed dipole. The introduction of parasitic patches can improve the current distribution between the upper and lower cut-off frequency of the bandwidth, and make up for the defects of the insufficient bandwidth of the crossed dipole and the SRR, thereby realizing wide CP bandwidth. The size of the antenna is 0.66 $\lambda_0 \times$ 0.66 λ_0. The measured results reveal that the IBW of the antenna is 69.1% (1.38-2.84 GHz), the CP bandwidth is 57.7% (1.43-2.59 GHz) and the gain is stable within the working bandwidth. In addition, since the crossed dipole and the SRR adopt the narrow-band resonance mode, the antenna shows good band-edge selectivity in the upper and lower sidebands. In general, the antenna has good advantages in size, structure, and performance index, and can be used as an alternative product in the field of satellite communication and RFID.

II. ANTENNA DESIGN AND ANALYSIS

A. Antenna configuration

Figure 1 shows the configuration of the proposed compact broadband CP crossed dipole antenna, which is mainly designed on an FR4 substrate with relative dielectric constant εr = 4.4 and a thickness of 0.8 mm. The proposed antenna consists of two orthogonal strip dipoles, two symmetrical 90° phase delay lines, four SRRs, four parasitic patches, and a metal reflector plate. The orthogonal dipoles printed on the upper and lower sides of the substrate are connected by delay lines to realize CP radiation. The interaction of the four SRRs with the crossed dipole produces two resonant modes at high and low

(a)

(b)
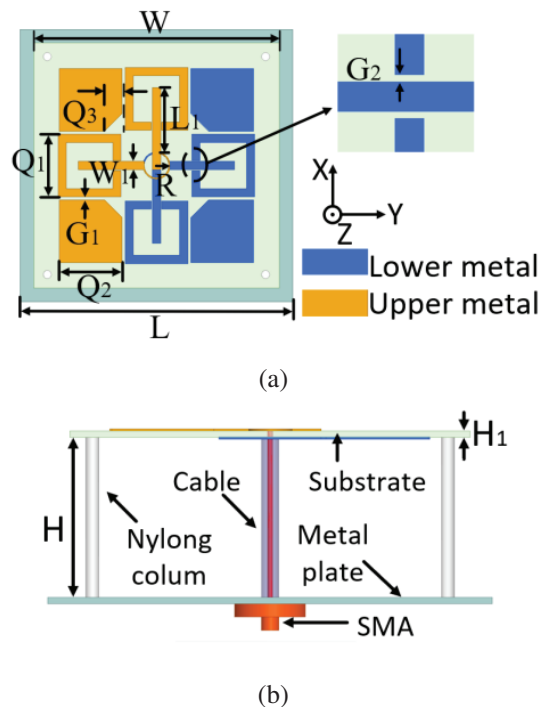
Fig. 1. Configuration of the proposed antenna. (a) Top view. (b) Side view.

Table 1: Antenna parameters (units: mm)

L	W	L_1	W_1	R	G_1
100	90	23	3.1	4.6	1.1
G_2	Q_1	Q_2	Q_3	H	H_1
0.2	23	17	6.6	36	0.8

frequencies, increasing the IBW as well as the axial ratio (AR) bandwidth. To obtain a better AR bandwidth, four rectangular patches with chamfered corners were introduced. In addition, the metal reflective plate of size L $\times$ L is added 1/4 λ below the dielectric plate, which can better enhance the unidirectional radiation performance of the antenna. The dielectric plate and the reflector are supported by four nylon columns to maintain the stability of the antenna. Finally, the optimal results are obtained by optimizing the parameter characteristics through HFSS. In the simulation optimization, the excitation type of the antenna adopts a lumped port setting, and the size of the radiation box is selected to be no less than a quarter of the working wavelength of the low frequency from the antenna edge. The optimal parameters of the antenna are shown in Table 1.

B. Antenna mechanism

To better explain the working mechanism of the antenna, Fig. 2 shows the evolution process of the antenna, and Fig. 3 shows the relationship between the corre-
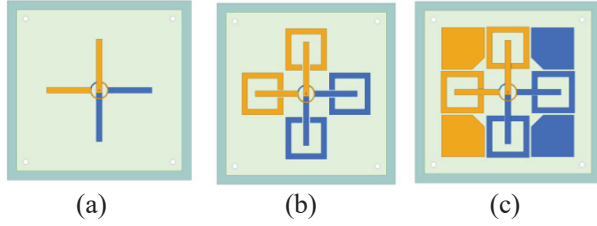
Fig. 2. Research process of the proposed antenna. (a) Antenna-I. (b) Antenna-II. (c) Antenna-III.
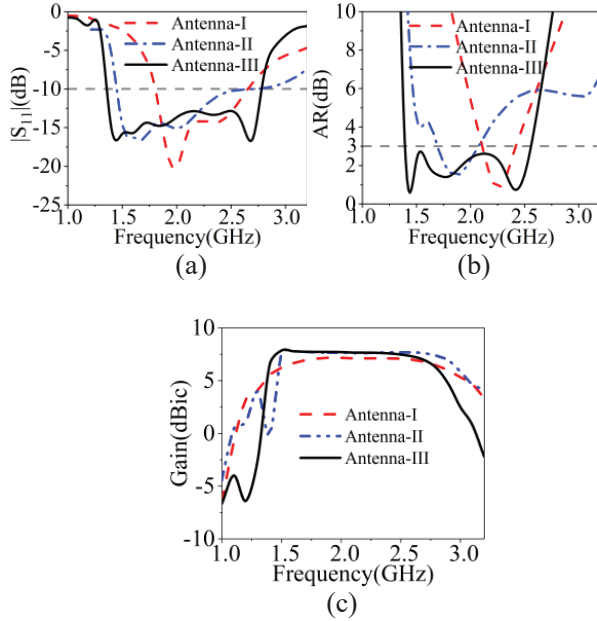
Fig. 3. Simulated results of the Antenna-I, Antenna-II, and Antenna-III. (a) $|S_{11}|$. (b) AR. (c) Gain.

sponding simulated reflection coefficient and the AR as a function of frequency. As shown in Fig. 2 (a), Antenna-I is an early crossed dipole antenna consisting of orthogonal dipoles connected with delay lines. The simulation results in Fig. 3 show that Antenna-I has only one resonant mode corresponding to the dipole length, the matching bandwidth and the AR bandwidth are relatively narrow, and the AR bandwidth is only 15.6%. As shown in Fig. 2 (b), the modified Antenna-II is composed of four SRRs interacting with the crossed dipole. On the one hand, this ingenious design can extend the low-frequency current path, reduce the electrical size of the antenna, and realize the compact of the antenna. On the other hand, the SRR resonant characteristic can increase the resonant frequency point and generate two resonant modes of high frequency and low frequency, thus realizing the expansion of the working bandwidth. As can be seen from Fig. 3, compared with Antenna-I, the matching bandwidth of the modified Antenna-II

is significantly enhanced, and a new AR bandwidth is introduced. However, between the high frequency and low frequency resonant frequency points, their AR is still not ideal.

To further obtain the wide AR bandwidth, four rectangular patches with chamfered corners are introduced, and the introduction of parasitic chamfered patches has a positive effect on the SRR current distribution, which can improve the resonant mode between high and low frequencies. The design of the chamfered corner is to further improve the amplitude ratio of the two orthogonal electric fields in the working frequency band and help the antenna to achieve a good AR bandwidth. In addition, it can be seen from Fig. 3 (c) that the introduction of the SRR causes the antenna to generate a radiation null at low frequency. This is because of the resonance characteristic of the SRR. To verify the radiation null, the equivalent LC resonant circuit of the SRR is shown in Fig. 4 [17], [18]. The L value depends on the length (Q_1 and Q_2) of the SRR, and the C value is determined by G_2. To illustrate the radiation null, the parameters Q_1 and Q_2 of Antenna-II are analyzed in Fig. 5. It is observed that the low-frequency radiation null point can be adjusted by the size of the SRR. Furthermore, the current distribution on the parasitic patch affects the SRR, which has excellent sideband selection characteristics at low frequencies, and a 3 dB drop at high frequencies. Thereby a better band-edge selectivity of the antenna is realized.

To verify the CP radiation characteristics of the designed antenna, Fig. 6 shows the current distribution diagrams of the antenna at 1.45 GHz, 1.8 GHz, and 2.4 GHz frequency points. It can be seen from Fig. 6 (a) that the vertical current components of the 0° phase SRR cancel each other at low frequency of 1.45 GHz, so the dominant current is synthesized by the horizontal current of the SRR and the vertical current of the dipoles. The dominant current in the 90° phase at low frequency of 1.45 GHz is composed of the vertical current of the SRR and the horizontal current of the dipole. Figure 6 (b) shows that the current direction at 1.8 GHz is dominated by dipoles. The SRR and the parasitic patch affect the vertical and horizontal current distribution, which is the main

Fig. 4. Equivalent LC circuit of the SRR.
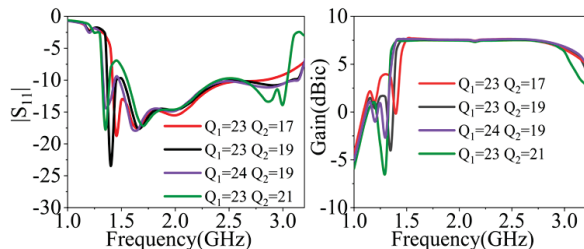
Fig. 5. The simulated $|S_{11}|$ and gain with different values of Q_1 and Q_2.
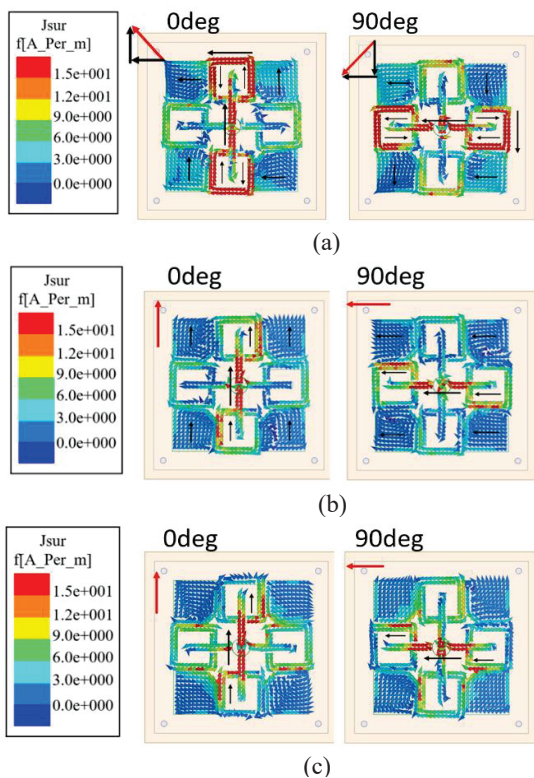
Fig. 6. Simulated current distributions of the antenna. (a) 1.45 GHz, (b) 1.8 GHz, and (c) 2.4 GHz.

factor to realize the CP mode. As shown in Fig. 6 (c), the current at 2.4 GHz is mainly distributed on the dipole. Therefore, the CP radiation is achieved mainly through dipoles and phase delay lines at high frequencies. As can be seen from Fig. 6, according to the rotation direction of the current, it can be concluded that the current flows in the counter-clockwise direction along the +z direction in the working frequency band, so the antenna generates right-handed circularly polarized (RHCP) waves.

III. SIMULATED AND MEASURED RESULTS

To verify the accuracy of the proposed antenna, a prototype was fabricated, as shown in Fig. 7 (a).

The reflection coefficient of the proposed antenna is measured by Agilent-89441A VNA, and the gains, ARs and radiation patterns are measured in a Far-field microwave anechoic chamber. As can be seen in Fig. 7 (a), the measured and simulated IBW of the proposed antenna are 69.6% (1.35-2.79 GHz) and 69.1% (1.38-2.84 GHz), respectively. The simulated results are in good agreement with the measured results. Figure 7 (b) shows the measured and simulated results of AR and gain. As illustrated in Fig. 7 (b), the measured and simulated 3 dB AR bandwidths are 57.7% (1.43-2.59 GHz) and 58.5% (1.4-2.56 GHz) respectively. Compared with the simulated results, the working frequency band is slightly shifted to the right in the measured results, which may be caused by the dielectric constant error of the substrate and the processing error. Figure 7 (b) illustrates the measured and simulated gain results are in good agreement, and the in-band fluctuation is less than 1.5 dB, which shows good in-band flatness. In addition, the reflection coefficient and gain of the antenna all show good sideband selection characteristics, which gives the antenna a certain filtering function. Figure 8 shows the measured and simulated radiation patterns for two principal planes (xoz and yoz) at 1.45 GHz, 1.8 GHz, and 2.4 GHz, respectively. The simulated results agreed well with the measured results. It can be observed that the RHCP waves are at least 15 dB larger than the left-handed Circularly Polarized (LHCP) waves, which means that the antenna radiates RHCP waves.

To highlight the novelty of the proposed antenna, Table 2 lists a comparison of the performance between this paper and other references [4], [6], [7], [11], [13] and [15]. Compared with the references in [6] and [11], the proposed antenna is smaller in size. In addition, the proposed antenna has a wider CP bandwidth than the antennas in [11] and [15], and has a higher gain than the antenna in [15]. Although the CP bandwidth in [7] is the same as the proposed antenna, the size of the antenna in [7] is larger than the proposed antenna. Moreover, the proposed antenna has good band-edge selectivity and stable radiation pattern in the working frequency band.
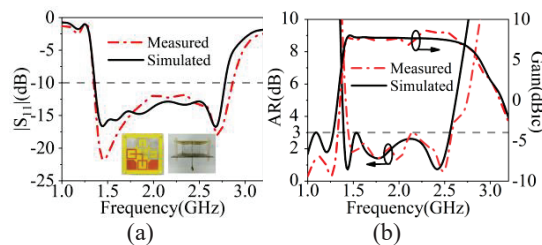
Fig. 7. Measured and simulated results of the proposed antenna. (a) $|S_{11}|$ (a prototype is shown as an insert). (b) AR and gain.
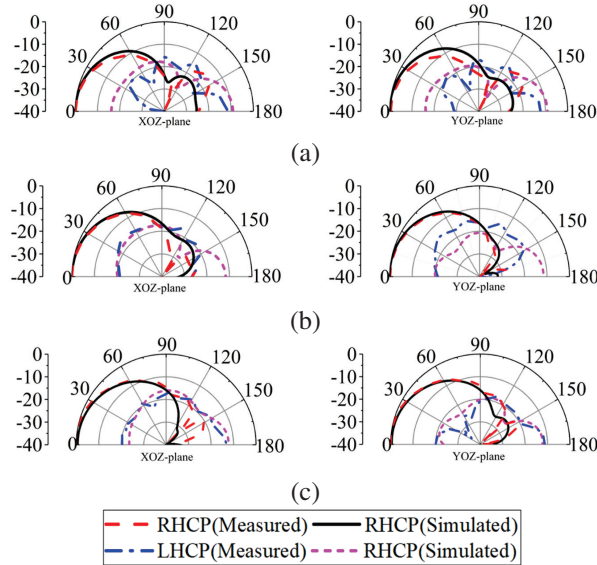
Fig. 8. Measured and simulated radiation patterns in xoz and yoz planes for the antenna at three frequencies. (a) 1.45 GHz. (b) 1.8 GHz. (c) 2.4 GHz.

Table 2: Comparison between the proposed and other works

Ref	Overall Size(λ_0^3)	IBW	ARBW	Band-edge Selectivity	Average Gain (dBic)
[2]	1.1×1.1×0.28	67.5%	53.4%	NO	8.0
[4]	1.04×1.04×0.26	77.6%	66%	NO	7.2
[5]	0.79×0.79×0.27	95.0%	58.6%	NO	8.2
[9]	0.88×0.88×0.23	78.3%	51%	NO	9.6
[11]	0.97×0.97×0.32	82%	68.2%	NO	8.0
[13]	0.4×0.4×0.13	68.9%	52.4%	NO	3.0
Pro	**0.66×0.66×0.25**	**69.1%**	**57.7%**	**YES**	**7.7**

λ_0: operating wavelength in free space at the center frequency.

IV. CONCLUSION

In this study, a compact wideband CP antenna using SRR and parasitic patches has been presented. By adding the well-designed SRRs close to the crossed dipoles, the current path and the current distribution can be well modified, also the size of the antenna and the AR bandwidth of the high-frequency can be improved. In addition, the introduction of parasitic patches can improve the current distribution between the upper and lower cut-off frequency points of the bandwidth, and make up for the defects of the insufficient bandwidth of the crossed dipole and the SRR, thereby realizing broadband CP radiation. The measured results show an IBW of 69.1% (1.38-2.84 GHz), and a wide AR bandwidth of 57.7% (1.43-2.59 GHz). Moreover, the designed antenna achieves a stable gain in the working band and good band-edge selectivity,

which can be used as a candidate for ISM band, WiBro and Inmarsat communication systems.

REFERENCES

[1] J. W. Baik, K. J. Lee, W. S. Yoon, T. H. Lee, and Y. S. Kim, "Circularly polarised printed crossed dipole antennas with broadband axial ratio," *Electron. Lett.*, vol. 44, no. 13, pp. 785-786, June 2008.

[2] G. Feng, L. Chen, X. Xue, and X. Shi, "Broadband circularly polarized crossed-dipole antenna with a single asymmetrical cross-loop," *IEEE Antennas Wireless Propag. Lett.*, vol. 16, pp. 3184-3187, Oct. 2017.

[3] S. X. Ta and I. Park, "Crossed dipole loaded with magneto-electric dipole for wideband and wide-beam circularly polarized radiation," *IEEE Antennas Wireless Propag. Lett.*, vol. 14, pp. 358-361, Oct. 2015.

[4] L. Wang, W.-X. Fang, Y.-F. En, Y. Huang, W.-H. Shao, and B. Yao, "Wideband circularly polarized cross-dipole antenna with parasitic elements," *IEEE Access.*, vol. 7, pp. 35097-35102, Mar. 2019.

[5] T. K. Nguyen, H. H. Tran, and N. Nguyen-Trong, "A wideband dual-cavity-backed circularly polarized crossed dipole antenna," *IEEE Antennas Wireless Propag. Lett.*, vol. 16, pp. 3135-3138, Oct. 2017.

[6] Z. Zhao, Y. Li, M. Xue, L. Wang, Z. Tang, and Y. Yin, "Design of wideband circularly polarized crossed-dipole antenna using parasitic modified patches," *IEEE Access.*, vol. 7, pp. 75227-75234, June 2019.

[7] Y. He, W. He, and H. Wong, "A wideband circularly polarized cross-dipole antenna," *IEEE Antennas Wireless Propag. Lett.*, vol. 13, pp. 67-70, Jan. 2014.

[8] M. Elsaid, K. R. Mahmoud, M. Hussein, M. F. Hameed, A. Yahia, and S. S. Obayya, "Ultra-wideband circularly polarized crossed-dual-arm bowtie dipole antenna backed by an artificial magnetic conductor," *Microw. Opt. Technol. Lett.*, vol. 61, no. 12, pp. 2801-2810, Aug. 2019.

[9] H. H. Tran and I. Park, "Wideband circularly polarized cavity-backed asymmetric crossed bowtie dipole antenna," *IEEE Antennas Wireless Propag. Lett.*, vol. 15, pp. 358-361, June 2016.

[10] X. Liang, J. Ren, L. Zhang, C. He, J. Geng, W. Zhu, and R. Jin, "Wideband circularly polarized antenna with dual-mode operation," *IEEE Antennas Wireless Propag. Lett.*, vol. 18, no. 4, pp. 767-770, Apr. 2019.

[11] Z. Guo, Z. Zhao, Y. Yang, and X. Ding, "A directional circularly polarized crossed dipole antenna with bandwidth enhancement," *Microw. Opt. Technol. Lett.*, vol. 60, no. 9, pp. 2161-2167, Sep. 2018.

[12] L. Wang, K. Chen, Q. Huang, L. Wang, K. Chen, Q. Huang, W. Shao, W. Fang, G. Lu, and Y. Huang, "Wideband circularly polarized cross-dipole antenna with folded ground plane," *IET Microw. Antennas Propag.*, vol. 15, no. 5, pp. 451-456, Apr. 2021.

[13] H. Zhang, Y. Guo, and G. Wang, "A design of wideband circularly polarized antenna with stable phase center over the whole GNSS bands," *IEEE Antennas Wireless Propag. Lett.*, vol. 18, no. 12, pp. 2746-2750, Dec. 2019.

[14] L. Wen, S. Gao, B. Sanz-Izquierdo, C. Wang, W. Hu, X. Ren, and J. Wu, "Compact and wideband crossed dipole antenna using coupling stub for circular polarization," *IEEE Trans. Antennas Propag.*, vol. 70, no. 1, pp. 27-34, Jan. 2022.

[15] Y. Feng, J. Li, B. Cao, J. Liu, G. Yang, and D. Wei, "Cavity-backed broadband circularly polarized cross-dipole antenna," *IEEE Antennas Wireless Propag. Lett.*, vol. 18, no. 12, pp. 2681-2685, Dec. 2019.

[16] Z. Guo, X. Li, H. Yang, J. Zhang, and C. Zheng, "Compact circularly polarized crossed dipole antenna with wide bandwidth and wide axial ratio," *13th International Symposium on Antennas, Propagation and EM Theory (ISAPE)*, Zhuhai, China, vol. 1, pp. 1-3, Dec. 2021.

[17] P. Jha, A. Kumar, A. De, and R. K. Jain, "Super ultra-wideband planar antenna with parasitic notch and frequency selective surface for gain enhancement," *Applied Computational Electromagnetics Society (ACES) Journal*, vol. 37, no. 7, pp. 757-764, Dec. 2022.

[18] P. Jha, A. Kumar, A. De, and R. K. Jain, "CPW-fed metamaterial inspired compact multiband antenna for LTE/5G/WLAN communication," *Frequenz*, vol. 76, no. 7-8, pp. 401-407, Aug. 2022.

Hailong Yang received his B.S. in Communication Engineering from Heze University, Heze, China, in 2012. He received his M.S. and Ph.D degrees in Communication Engineering from Xi'an University of Technology, Xi'an, China, in 2015 and 2019 respectively. He joined the faculty of the Electronic Engineering Department, Xi'an University of Posts and Telecommunications, in 2019. His research interests include wave propagation and antenna design.

Zhiqiang Guo was born in Henan Province, China, 1997. He is currently pursuing a Master of Engineering degree at the School of Electronic Engineering, Xi'an University of Posts and Telecommunications. His current research interests include circularly polarized antennas, filtering antennas and array antennas.

Xuping Li was born in Xi'an, Shanxi, China in 1981. He received his Ph.D. degree in Electromagnetic Fields and Microwave Technology from Xidian University, Xi'an, China, in 2015. His research interests are antenna theory and engineering.
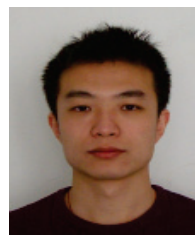
Yunqi Zhang was born in BaoTou, Inner Mongolia, China. He received his Ph.D. degree from Xidian University, Xi'an, China in 2015. He is currently working at the Xi'an University of Posts and Telecommunications. In 2017 he joined the school of Physics and Optoelectronic Engineering, Xidian University, as a post doctoral researcher. His research interests include GPS antennas, CP antennas, omnidirectional antennas and antenna array designs.

Xueyan Song   was born in Henan Province, China, 1989. She received her B.E. degree in Electronic and Information Engineering from Xidian University, Xi'an, China, in 2012. She received her Ph.D. degree in Electromagnetic Fields and Microwave Technology from Xidian University, Xi'an, China, in 2018.

She joined the School of Electronic Engineering, Xi'an University of Posts and Telecommunications in 2018. Her research interests include artificial magnetic conductors, low RCS antennas, low-profile antennas, frequency selective surfaces and reflector antennas.

Shanzhe Wang   received his M.S. degree in Electronic Science and Technology from Beijing Jiaotong University, Beijing, China, in 2017. He received his Ph.D. degree in Electronic Science and Technology from Beijing Jiaotong University, Beijing, China, in 2022.

He joined the School of Electronic Engineering, Xi'an University of Posts and Telecommunications in 2022. His research interests include fixed-frequency beam-scanning leaky-wave antennas.

A Three-dimensional Compact Propeller-shaped Circularly Polarized Ceiling Antenna

Jia-Xiang Chen, Hai-Tao Xing*, Jian-Mei Huang, Meng-Nan Wang, and Zhong-Hua Ma

School of Marine Information Engineering
Jimei University, Xiamen, Fujian, 361021, China
chenjx7335@jmu.edu.cn; xht2005@jmu.edu.cn; 202021112035@jmu.edu.cn;
202211810012@jmu.edu.cn; mzhxm@jmu.edu.cn
*Corresponding author: xht2005@jmu.edu.cn

Abstract – A three-dimensional compact propeller-shaped circularly polarized ceiling-mounted antenna loaded by inverted L-shaped slot is proposed in this paper. This three-dimensional structure has a small size, single feed and half-plane radiation mode. The antenna is composed of four alternately welded radiating elements and a disc reflector. Each radiating element is formed by etching a rectangular microstrip radiating patch and a trapezoidal microstrip radiating patch on the surface of the substrate. The four radiating elements are welded vertically on the disc reflector. The back of the disc reflector has the ground plane. The antenna is fed coaxially through the via in the center of the disc reflector. The result demonstrates that the 10-dB impedance fractional bandwidth achieves 66.3% (4.4-8.94 GHz). The 3-dB axial ratio fractional bandwidth is 2.2% (6.44-6.58 GHz). The radiation characteristic is close to half-space radiation on the xoz plane and the yoz plane. The peak gain of the antenna is 3.22 dBi. The simulation and measurement results are in good agreement. With its compact structure, effective coverage, miniaturization, etc., the antenna is very suitable for applications such as biomedical monitoring equipment and short-range radio communications.

Index Terms – axial ratio (AR), circular polarization (CP), coaxial feed, inverted L-shaped slot, three-dimensional.

I. INTRODUCTION

With the rapid development of modern wireless communications and the increasing number of communication systems, circularly polarized (CP) antennas have attracted more and more attention due to their excellent performance and have been widely used in wireless communication systems [1].The attractive benefit of CP antennas is that it can send and receive signals in all planes having strong absorption and reflection of radio signals [2]. Attributing to the requirement of great capacity and higher transmission rate of 5G in the future, it is difficult to find spectrum resources with large bandwidths of up to 100 MHz or even hundreds of megahertz for spectrum below 6 GHz. Spectrum above 6 GHz is an important source for 5G to find new frequency bands. The use of spectrum above 6 GHz for 5G has become a global consensus [3]. Because the antenna proposed in this article has good directivity and compact structure, it has potential application for indoor positioning, unmanned aerial vehicles (UAVs), automobiles and other point-to-point communication, or in subway stations and conference halls etc.

Circularly polarization characteristics of antenna can be achieved by many methods, such as cutting corners [4], rotated stacked [5] and stub line loading [6], selecting a suitable feed point location and multiple feeding ports [7]. The CP antenna can resist the interference of clouds, rain and fog in radar and satellite communication systems [8]. The correct information can be received by using CP antenna in devices that swing and roll violently [9]. CP antennas are used in TV and broadcasting systems to improve the quality of the receiving signal [10]. The CP antenna can eliminate the polarization distortion which is caused by the ionospheric Faraday rotation effect [11].

Compared with linearly polarized (LP) antennas, CP antennas have many advantages, which can be applied to a very wide number of fields. Therefore, a variety of new CP antennas with excellent performance have been proposed. Guo Qing-Yi et al. proposed a Fabry-Pérot cavity (FPC) CP antenna that works in the millimeter wave frequency band [12]. The antenna integrates a three-dimensional (3D) printed resonator with an inserted partial reflective surface to enhance the antenna's gain and CP bandwidth. This FPC antenna provides high directional radiation similar to a horn antenna. In [13], a novel CPW-fed microstrip antenna which uses two PIN diodes to switch between RHCP and LHCP, is introduced. This

antenna is designed to work in the center frequency of 2.4 GHz which is applicable in WLAN systems. However, due to its large size, it is not easy to conform to other equipment.

To enhance indoor communication quality and communication coverage, experts and scholars have designed various structure ceiling antennas. In [14], a 2×2 array of ceiling antennas for access point devices is proposed, which consists of a beamforming network and a four-sided clover-leaf antenna (clover-leaf antenna). The beamforming network includes four microstrip rat-race couplers and two 90° delay lines. The peak gain reaches 7.8 dBi, but there is a radiation zero point in the main radiation direction, and the structure is more complicated. Jang and Go [15] proposed a ceiling-mounted antenna composed of a cylindrical monopole, foam, a circular ground plane and an SMA connector. It can be applied to mobile and satellite communication systems, but there is a phenomenon of distortion of radiation characteristics. A monopole ceiling antenna based on asymmetric dipole offset feed, which reduced the radiation zero point and achieved low passive intermodulation (PIM) has been reported [16], mainly working at 60 GHz millimeter wave frequency band and LP radiation. A central coaxial feed monopole formed by placing three metal patches on a circular ground plane is reported in [17]. There are three shorting legs composed of coupling patches on the monopole to extend the lowest frequency, and the top of the coupling patch is loaded with a broadband omnidirectional antenna composed of a metal disk. Although higher gain and better efficiency are achieved, there is a radiation zero point in the radiation direction. The above-mentioned antennas provide good gain, impedance bandwidth and radiation pattern, but they are all in LP mode, which has some disadvantages for some specific application scenarios, such as drones, subways station, and halls, etc. For example, drones may cause communication interruption to base stations due to their instability and mobility, and they are often affected by fast fading. Multipath of subways and shaking of terminals will also cause the quality of communication to decrease. Although [18] designed CP polarized ceiling antenna with a multilayer spiral structure, this antenna is mainly used for indoor radio frequency identification at 900 MHz.

In this paper, a circularly polarized ceiling antenna with a three-dimensional propeller shape is proposed and implemented. The antenna consists of four substrates etched with rectangular microstrips and trapezoidal microstrips to form radiating patches, which are vertically welded on a disc reflector with ground on the back. Each radiating patch is loaded with an inverted L-shaped slot. A single-port coaxial feed is performed through the through hole of the disc reflector. This structure has good CP characteristics. A 50 Ω characteristic impedance SMA connector is located under the reflector that has little effect on the electrical characteristics of the antenna. This kind of antenna can be hung under the unmanned aerial vehicles, the top of the car or the roof to cover a larger area.

II. THE PRINCIPLE OF CIRCULAR POLARIZATION

During the propagation of electromagnetic waves in space, the electric field and magnetic field vectors keep reciprocating. Electromagnetic wave polarization usually refers to the trajectory projected by the end of the electric field vector on a plane perpendicular to the direction of propagation. Here, the change vector of the magnetic field does not need to be considered, because the magnetic field and the electric field have a fixed relationship. When the rotation direction of the electric field vector of a CP wave is clockwise, a right-hand circular polarization (RHCP) signal is generated. For a left-hand circular polarization (LHCP) wave, the electric field vector will rotate counter clockwise [19]. In order to realize that the track of the electric field vector as a function of time is a circle, it must be satisfied that the electric field must have two orthogonal linear components, the amplitude of the two components must be equal, the phase difference is an odd multiple of 90 [20]. If the complex voltage terms in the horizontal and vertical planes E_H and E_V are of equal amplitude and in phase quadrature ($\pm\pi/2$), these terms may be combined to express either the RHCP or LHCP wave components [21]:

$$E_{RHCP} = \frac{1}{\sqrt{2}}(E_H + jE_V), \qquad (1)$$

and

$$E_{LHCP} = \frac{1}{\sqrt{2}}(E_H - jE_V). \qquad (2)$$

The real and imaginary components of the horizontal and vertical response can be expressed as:

$$E_H = E_A \cos(H_p) + jH_A \sin(H_p), \qquad (3)$$

$$E_V = E_A \cos(V_p) + jV_A \sin(V_p). \qquad (4)$$

The horizontal and vertical amplitude (H_A, V_A) and phase components (H_P, V_P) are quantities that are measured at each angle in the far field of the antenna. Substitute formulas (1) and (2) into formulas (3) and (4) to obtain the polarization field:

$$E_{LHCP} = \frac{1}{\sqrt{2}}\left\{[H_A \cos(H_p) + V_A \sin(V_p)] + j[H_A \sin(H_p) - V_A \cos(V_p)]\right\}, \qquad (5)$$

and

$$E_{RHCP} = \frac{1}{\sqrt{2}}\left\{[H_A \cos(H_p) - V_A \sin(V_p)] + j[H_A \sin(H_p) + V_A \cos(V_p)]\right\}. \qquad (6)$$

The polarization of an antenna is related to the direction of the electric field radiated by the antenna. The radiation patterns that are generated by a CP antenna can be plotted by combining the amplitude and phase response of two orthogonals. In each hand of polarization, the power can be expressed by:

$$P(dB) = 10\log_{10}\left(\frac{E^2}{377}\right), \qquad (7)$$

where 377 Ω is the wave impedance in free space. A practical antenna normally generates a desired reference polarization in addition to an undesirable cross-polar component, which is polarized in the opposite hand. In the main beam, $|P_{RHCP}(dB)-P_{LHCP}(dB)|$ gives the cross-polar level at a given azimuth angle. AR is the ratio of the cross-polarized wave to the co-polarized wave, so for a perfect circular polarization conversion, the AR should be equal to one. The AR can be written as:

$$AR = 20\log_{10}(\frac{1+e}{1-e}), \qquad (8)$$

where $e=10^{-PdB/20}$ and P_{dB} is the cross-polar power.

A 3 dB point can be considered as the reference point for polarization conversion. When the values of AR are smaller than 3 dB, the structure can be used as a polarization converter. On the other hand, the frequency range for which the AR value is smaller than the reference value is called axial ratio bandwidth [22], [23].

III. ANTENNA STRUCTURE

The propeller structure of the CP antenna is shown in Figs. 1 (a) and (b). The radiation patch includes a rectangular microstrip patch and a trapezoidal microstrip patch, which are etched on rectangular dielectric substrate to form a radiating element. An inverted L-shaped slot is loaded on each radiating element. The four radiating elements are welded together in a staggered manner and placed vertically on the disc reflector to form a propeller shape as shown in Fig. 1 (a). The feed point is located in the center of the disc reflector structure by connecting 50-Ω SMA connector to realize the symmetry axis ratio and radiation pattern. Cross-placed inverted L-shaped radiating elements can produce two orthogonal polarization components, thereby synthesizing circularly polarized waves in the far field. Figure 1 (b) is the top view of the antenna structure.

The structure of the propeller is to generate mutually orthogonal electromagnetic waves in order to synthesize circularly polarized waves in the far field. Compared with other types of ceiling antennas, due to its special structure, it has a more compact structure and better directivity. However, this structure causes a certain amount of interference between patches placed orthogonal to each other, which will have a certain impact on reflection coefficient and radiation pattern. The interfer-

ence can be minimized by adjusting the length L_1 and width W_1 of the rectangular patch.
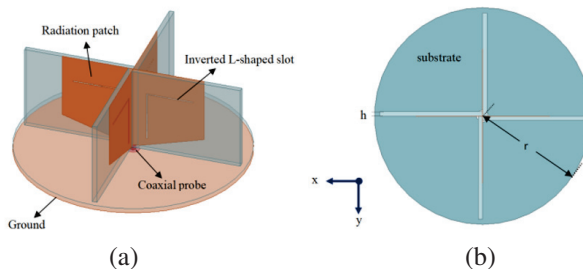
Fig. 1. Proposed antenna configuration. (a) Three-dimensional view. (b) Top view of the substrate.
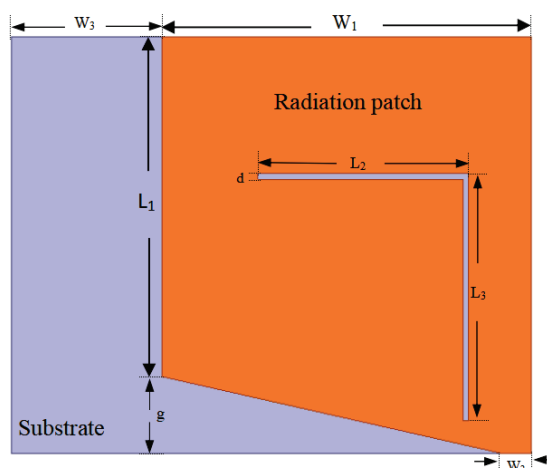
Fig. 2. Structure diagram of inverted L-shaped slot radiating element.

The structure of the radiating element loaded by the inverted L-shaped slot is shown in Fig. 2. The size of the rectangular patch is $W_1 \times L_1$. The bottom side of vertically placed trapezoidal patch is W_1, the upper bottom side W_2, and the height g. The length and width of the microstrip radiation patch are calculated by the following equations:

$$\mathrm{W} = \frac{c}{2f_o}\left(\frac{2}{\varepsilon_r+1}\right)^{1/2}, \qquad (9)$$

$$f_o = \frac{c}{2\sqrt{\varepsilon_e}(L+\Delta L)}, \qquad (10)$$

where ΔL is the extension caused by the edge effect, and ε_r is the relative dielectric constant of the substrate, ε_e is the effective dielectric constant. At 6.5 GHz operating frequency, the length (L_1) and the width (W_1) of the radiating microstrip patch are 12.2 mm and 15.2 mm by the equation (9) and (10), respectively. L is the equivalent length of the microstrip edge effect. The width W_2 of the 50 characteristic impedance microstrip is 2.2 mm. The coaxial probe is fed from the back of the circular

Table 1: Design parameters of the propeller shaped CP antenna (unit: mm)

W_1	W_2	W_3	L_1	L_2	L_3	g	d	r	h
13.4	2.2	6	12.8	7.7	8.8	2.9	0.2	20	1

reflector. The inverted L-shaped slot is used to change the current path on the radiating patch, thereby the radiation intensity of the antenna is enhanced in the +z direction. The inverted L-shaped slot has a horizontal length of L_2, the vertical length of L_3, and the slot width of d. The radiation pattern and impedance bandwidth of the antenna are optimized by adjusting the structural parameters of the antenna. The relevant structural parameters are shown in Table 1.

IV. SIMULATION DESIGN ANALYSIS

The proposed three-dimensional compact propeller-shaped CP ceiling-mounted antenna is designed by the High Frequency Electromagnetic Simulator software (HFSS). The low cost FR4 substrate is used in the design, with the thickness of 1 mm, the relative dielectric constant of 4.4, and the loss tangent of 0.02.

The width W_1 of the rectangular microstrip radiating patch is changed, the corresponding reflection coefficient and AR characteristics are shown in Figs. 3 (a) and (b), respectively. When the width W_1 of the rectangular microstrip radiating patch is reduced from 13.6 mm to 13.3 mm in step of 0.1 mm, the impedance bandwidth of the antenna is influenced obviously. The result of Fig. 3 (a) shows that only when W_1 is equal to 13.4 mm, the reflection characteristic in the band is optimal, meanwhile, the 10 dB impedance bandwidth reaches 4.54 GHz. When the value of W_1 deviates from 13.4 mm, the reflection coefficient begins to deteriorate in the lower frequency band, and the 10 dB impedance bandwidth decreases. This is caused by resonance between the patches. Figure 3 (b) shows the AR results when W_1 changes from 13.3 mm to 13.6 mm. It is observed that when W_1=13.4 mm, the 3 dB AR bandwidth achieves 185 MHz, and the AR value is 0.99 dB at the center frequency. When the value of W_1 increases or decreases from 13.4 mm, the AR will increase, and the 3 dB AR bandwidth will decrease rapidly. Obviously, the optimal width W_1=13.4 mm is selected to achieve good impedance matching of the antenna and the 3 dB AR operating frequency is included in the 10 dB impedance bandwidth.

Figure 4 shows the effect on the AR characteristics of the antenna when the horizontal length L_2 of the inverted L-shaped slot is gradually increased from 7.6 mm to 7.9 mm in steps of 0.1 mm. Among them, when L_2 is greater than 7.7 mm, the AR characteristic deteriorates, and the working frequency band shifts to the high frequency at the same time. When L_2 is less
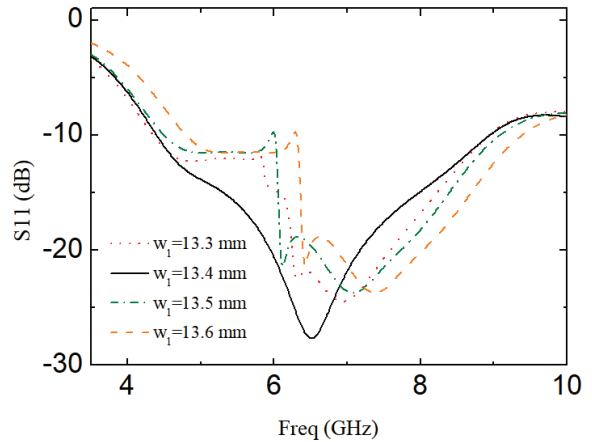
(a)
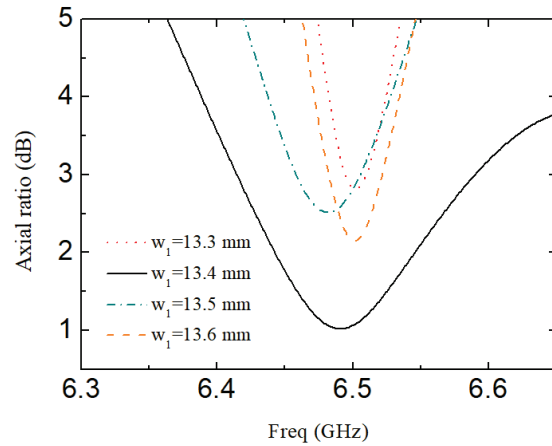
(b)

Fig. 3. Simulated results of the reflection coefficient and the AR with different W_1. (a) Reflection coefficient. (b) Axial ratio.
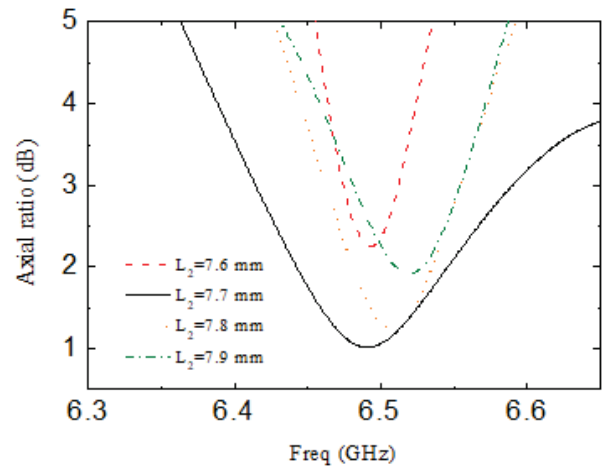
Fig. 4. Simulated results of the AR with different L_2.
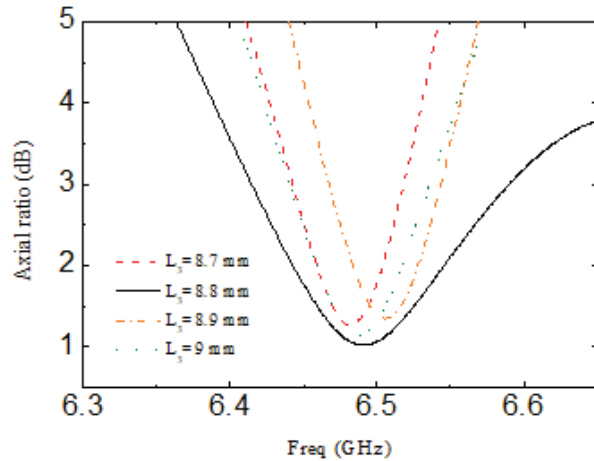
Fig. 5. Simulated results of the AR with different L_3.

(a)

(b)
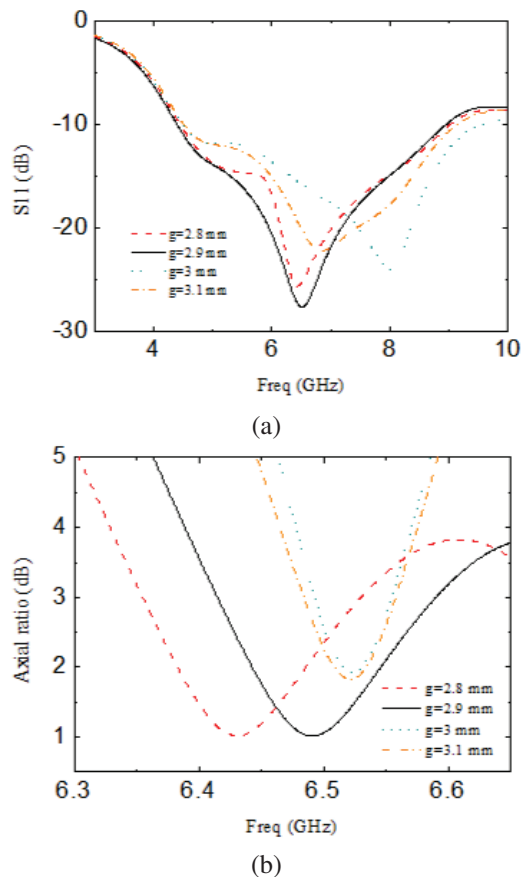
Fig. 6. Simulated results of the reflection coefficient and the AR with different g. (a) Reflection coefficient. (b) Axial ratios.

than 7.7 mm, the AR value slightly increases, and the 3 dB AR bandwidth decreases. When L_2=7.7 mm, the 3 dB AR bandwidth is the widest, and AR value of the center frequency is the smallest.

Figure 5 shows the AR results of the antenna when the vertical length L_3 of the inverted L-shaped slot changes. When L_3=8.8 mm, the axial ratio bandwidth is the widest, and the circular polarization characteristic is the best. When the length of L_3 deviates from 8.8 mm, the 3 dB AR bandwidth reduces sharply.

Figure 6 shows the simulation results of the reflection coefficient and the AR of the antenna when the height g of the trapezoidal microstrip is varied, respectively. Figure 6 (a) shows that when g is equal to 2.9 mm, there are excellent reflection coefficient and in-band characteristics. Figure 6 (b) shows that when g=2.9 mm, the center frequency is near 6.5 GHz. At this time, the antenna has a small AR value and the AR bandwidth is wide. When the value of g is less than 2.9 mm, the 3 dB AR frequency band moves to a low frequency. When the value of g is greater than 2.9 mm, the 3 dB AR frequency band moves to a high frequency. The AR bandwidth reduces rapidly and the performance in the band deteriorates.

V. EXPERIMENT RESULTS

To verify the simulation results, a propeller-shaped CP ceiling antenna was fabricated and measured. The actual measurement is conducted in an anechoic chamber with Agilent's vector network analyzer (VNA, Agilent E8362B). Figure 7 is the measurement photo of the CP antenna. Figure 8 is the simulation and measurement curve of the final antenna reflection coefficient. The measurement result shows that the frequency band with the reflection coefficient less than -10 dB is from 4.51 GHz to 9.01 GHz, and the bandwidth is 4.5 GHz, which is slightly smaller than the simulation result.

Figure 9 shows the measured AR characteristic curve. The frequency band range is from 6.44 GHz to 6.58 GHz with the AR less than 3 dB. The 3 dB AR bandwidth is 140 MHz and the 3 dB AR fractional bandwidth of the antenna is 2.2%. The measurement curve of the CP antenna gain and the radiation efficiency is

(a)   (b)
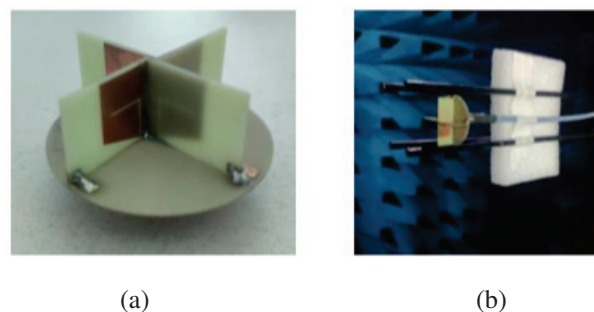
Fig. 7. Antenna photograph and anechoic chamber photograph. (a) Photograph of the fabricated CP antenna. (b) Measurement photograph of the CP antenna.
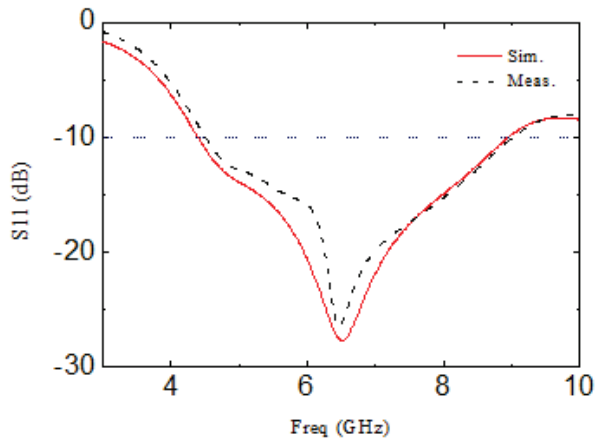
Fig. 8. Simulation and measurement results of the proposed antenna's reflection coefficient.
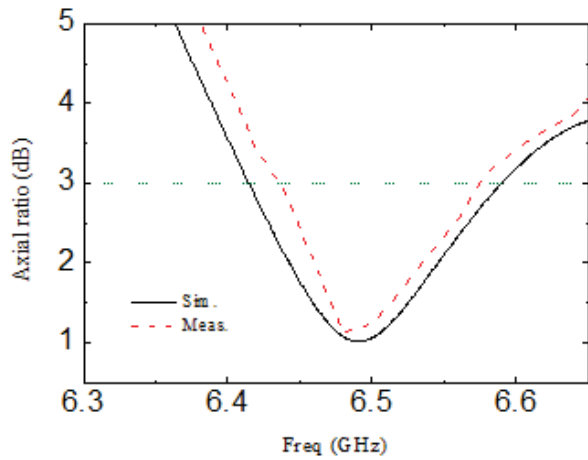
Fig. 9. Simulated and measured results of the AR curve of the proposed antenna.
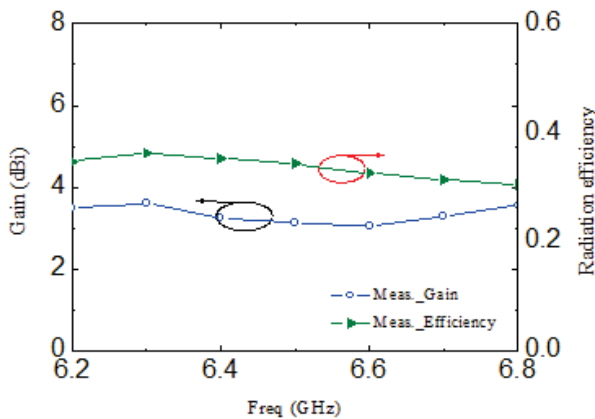
Fig. 10. Measured results of the antenna gain and radiation efficiency.

shown in Fig. 10. It is well known that as the size of the antenna is reduced, so does the efficiency. For the antenna proposed in this paper, in addition to the size of the antenna, the width d of the inverted L-shaped slot on the radiation patch and the dielectric constant of the substrate material will also affect the radiation efficiency measurement. The radiation efficiency of the antenna is 35% to 39% in the range of 6.2 GHz to 6.8 GHz in Fig. 10.

Figure 11 shows the simulated and measured xoz plane and yoz plane radiation patterns of far-field radiation at different working frequencies of 6.45 GHz,

(a)

(b)

(c)
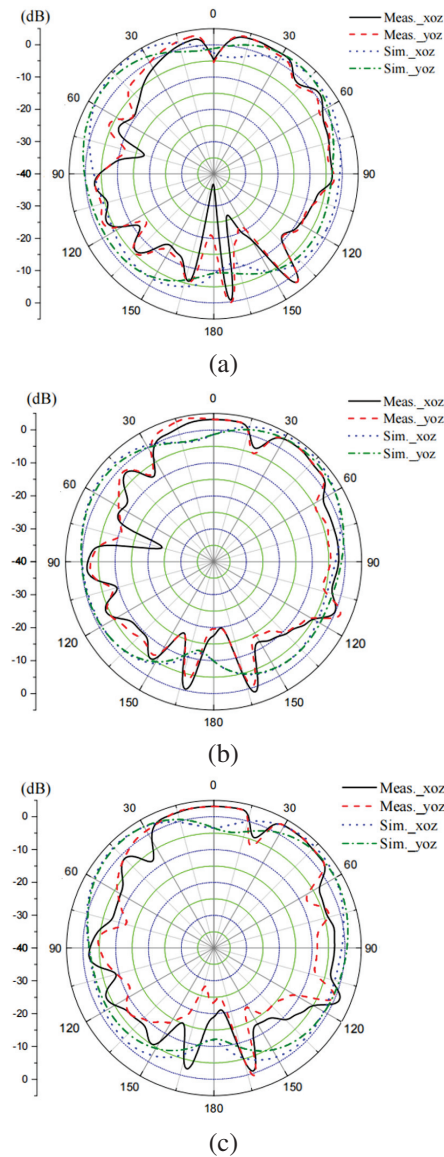
Fig. 11. The measured CP radiated patterns on xoz plane and yoz plane, respectively. (a) 6.45 GHz. (b) 6.5 GHz. (c) 6.6 GHz.

Table 2: Comparison of the published ceiling-mounted antennas

Ref.	IBW (S11<−10 dB) GHz	ARBW (AR<3 dB) GHz	Feeding Method	Radiation Zero Point	Antenna Size (λ_0^3)	Peak Gain (dBi)
[14]	2-2.9	-	Side	yes	1.6×1.6×0.35	7.8
[15]	1.98-3.55	-	Back	yes	0.07×0.07×0.85	3.5
[16]	0.698-0.960 1.35-3.8	-	Back	no	1.2×0.78×0.05	-
[17]	0.65-6	-	Back	yes	0.9×0.9×2.67	6
[18]	0.865-1.005	0.861-0.92	Back	no	0.3×0.9×0.9	4.3
[24]	2.41-2.47	-	Back	yes	0.5×0.5×0.65	0.4
This paper	4.4-8.94	6.44-6.58	Back	no	0.4×0.4×0.98	3.22

IBW=impedance bandwidth, ARBW=axial ratio bandwidth

6.5 GHz, and 6.6 GHz, respectively. The radiation patterns are all half-space radiation. Due to the size of the via of the reflector and the manufacturing process, a certain amount of radiation leakage occurs on the back side.

Table 2 compares the various types of ceiling antennas working in different frequency bands that have been published with the ceiling antennas proposed in this article. The key structural parameters and electrical parameters are listed in Table 2. Most of the ceiling-mounted antennas use coaxial back-feed excitation and the polarization characteristic is LP with a relatively large area. The fatal flaw in the comparison literature is that the ceiling-mounted antenna has a radiation zero point in the radiation direction. The propeller-type ceiling antenna proposed in this paper does not produce a radiation zero point in the radiation direction, meanwhile, it obtains a higher gain in a relatively small volume.

VI. CONCLUSION

In this paper, a novel ceiling-mounted CP antenna is proposed and implemented. The antenna is loaded with the inverted L slot structure on a microstrip radiation patch. Four cross-placed radiating elements are welded on the reflector substrate whose back has ground to realize half-space CP radiation. The measured impedance bandwidth reaches 4.5 GHz. The 3 dB AR bandwidth is 140 MHz. The gain fluctuated from 3.04 dBi to 3.22 dBi in the range of 6.2 GHz to 6.8 GHz. Because this propeller-shaped ceiling-mounted CP antenna has a compact structure and good directivity, it can be used in various wireless communication systems. It is especially suitable for, by way of example: UAVs, trains, airplanes or cabins, subway stations and other indoor places.

ACKNOWLEDGMENT

REFERENCES

[1] B. Qiu, Y. Xia, and Y. Li, "Gain-enhanced wideband circularly polarized antenna with a non-uniform metamaterial reflector," *Applied Computational Electromagnetics Society (ACES) Journal*, vol. 37, no. 3, pp. 281-286, 2022.

[2] I. Nadeem, M. Alibakhshikenari, F. Babaeian, A. Althuwayb, B. S. Virdee, L. Azpilicueta, S. Khan, I. Huynen, and F. Falcone, "A comprehensive survey on 'Circular Polarized Antennas' for existing and emerging wireless communication technologies," *Journal of Physics D: Applied Physics*, vol. 55, no. 3, pp. 033002, 2021.

[3] Y. Yang, B. Sun, and J. Guo, "A single-layer wideband circularly polarized antenna for millimeter-wave applications," *IEEE Trans. Antennas Propagat.*, vol. AP-68, pp. 4925-4929, 2020.

[4] N. Hussain, M. Jeong, A. Abbas, and N. Kim, "Metasurface-based single-layer wideband circularly polarized MIMO antenna for 5G millimeter-wave systems," *IEEE Access*, vol. 8, pp.130293-130304, 2020.

[5] J. H. Kim, C. H. Jeong, and W. S. Lee, "Rotated stacked yagi antenna with circular polarization for IoT applications," *Applied Computational Electromagnetics Society (ACES) Journal*, vol. 34, no. 8, pp. 1246-1249, 2019.

[6] B. Park and J. Lee, "Omnidirectional circularly polarized antenna utilizing zeroth-order resonance of epsilon negative transmission line," *IEEE Transactions on Antennas and Propagation*, vol. AP-59, pp. 2717-2720, 2011.

[7] B. Li, C. Hao, and X. Sheng, "A dual-mode quadrature-fed wideband circularly polarized dielectric resonator antenna," *IEEE Antennas and Wireless Propagation Letters*, vol. 8, pp. 1036-1038, 2009.

[8] C. Yang, L. Yang, and M. Wang, "Wideband circularly polarized antenna with L-shaped slot," *Journal of Microwaves*, vol. 28, pp. 94-96, 2012.

[9] Y. J. Zhang, X. J. Liang, and B. Zhao, "Design and realization of circular polarization cylindrical conformal antenna with omnidirectional radiation," *Manufacturing Automation*, vol. 31, pp. 1245-1249, 2010.

[10] R. E. Fisk and J. A. Donovan, "A new CP antenna for television broadcast service," *IEEE Transactions on Broadcasting*, vol. BC-22, pp. 91-96, 1976.

[11] Y. Shi and J. Liu, "Wideband and low-profile omnidirectional circularly polarized antenna with slits and shorting-vias," *IEEE Antennas and Wireless Propagation Letters*, vol. 15, pp. 686-689, 2016.

[12] Q. Y. Guo, Q. W. Lin, and H. Wong, "A high gain millimeter-wave circularly polarized Fabry–Pérot antenna using PRS-integrated polarizer," *IEEE Transactions on Antennas and Propagation*, vol. AP-69, pp. 1179-1183, 2021.

[13] V. Zarei, H. Boudaghi, M. Nouri, and S. A. Aghdam, "Reconfigurable circular polarization antenna with utilizing active devices for communication systems," *Applied Computational Electromagnetics Society (ACES) Journal*, vol. 30, no. 9, pp. 990-995, 2015.

[14] J. F. Keh, M. Chou, Z. C. Zhang, Q. X. An, and W. J. Liao, "A beamforming-network-based four-squint-beam array antenna for ceiling-mount access point," *IEEE Antennas and Wireless Propagation Letters*, vol. 18, pp. 707-711, 2019.

[15] Y. W. Jang and H. C. Go, "A low-profile broadband 16-mm-diameter post-type monopole antenna ceiling-mounted in a building," *Microwave and Optical Technology Letters*, vol. 41, pp. 395-397, 2004.

[16] K. J. Ng, M. T. Islam, A. Alevy, M. F. Mansor, and C. C. Su, "Azimuth null-reduced radiation pattern, ultralow profile, dual-wideband and low passive intermodulation ceiling mount antenna for long term evolution application," *IEEE Access*, vol. 7, pp. 114761-114777, 2019.

[17] L. Zhou, Y. Jiao, Y. Qi, Z. Weng, and L. Lu, "Wideband ceiling mount omnidirectional antenna for indoor distributed antenna system applications," *IEEE Antennas and Wireless Propagation Letters*, vol. 13, pp. 836-839, 2014.

[18] J. Choo, S. Yoo, and H. Choo, "Design of a ceiling-mounted reader antenna to maximize the readable volume coverage ratio for an indoor UHF RFID application," *Microwave and Optical Technology Letters*, vol. 59, pp. 2136-2141, 2017.

[19] B. Y. Toh, R. Cahill, and V. F. Fusco, "Understanding and measuring circular polarization," *IEEE Transactions on Education*, vol. 46, pp. 313-318, 2003.

[20] C. A. Balanis, *Antenna Theory: Analysis and Design*, 3rd ed, Harper & Row, New York City, 1982.

[21] G. E. Evans, *Antenna Measurement Techniques*, Artech House, Norwood, MA, 1990.

[22] O. Altintas, E. Unal, O. Akgol, M. Karaaslan, F. Karadag, and C. Sabah, "Design of a wide band metasurface as a linear to circular polarization converter," *Modern Physics Letters B*, vol. 31, no. 30, pp. 1750274, 2017.

[23] O. Akgol, O. Altintas, E. Unal, M. Karaaslan, and F. Karadag, "Linear to left-and right-hand circular polarization conversion by using a metasurface structure," *International Journal of Microwave and Wireless Technologies*, vol. 10, pp. 133-138, 2018.

[24] Y. T. Liu, C. W. Su, C. L.Tang, S. T. Fang, and K. L. Wong, "Radiation pattern control for an on-ceiling omnidirectional monopole antenna," *Microwave and Optical Technology Letters*, vol. 41, pp. 106-108, 2004.
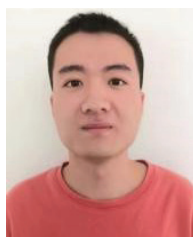
Jia-Xiang Chen was born in 1998 in Fujian Province, China. He received a bachelor's degree from Nanchang Hangkong University in 2020. He is currently working on his M.S. degree in Information and Communication Engineering at Jimei University, Fujian Province, China. His research interest is antenna techniques.

Hai-Tao Xing was born in 1983 in Shandong, China. In 2010, he obtained a master's degree in Communication and Information Engineering from Ningbo University. At present, his main research interests are embedded systems, artificial intelligence and IoT.

Jian-Mei Huang was born in 2002 in Fujian Province, China. She is currently pursuing a B.S. degree with the Department of Communication Engineering, Jimei University, Fujian Province, China. Her research interest is antenna techniques.

Meng-Nan Wang was born in 2000 in Henan Province, China. She received a bachelor's degree from Zhengzhou University of Aeronautics in 2022. She is currently working on her M.S. degree in Information and Communication Engineering at Jimei University, Fujian Province, China. Her research interest is chipless RFID sensors.

Zhong-Hua Ma was born in Gansu, Republic of China, in 1973. He received his Ph.D. degree in Microelectronics from Lanzhou University in 2018. His present research interests include antenna techniques, RF circuit design, RFID systems and IoT.

Equivalent Circuits of Dipole Antennas for Broadband Applications

Binwen Wang, Hui Ning, Youjie Yan, Chengyun Cao, and Meiqi Zhu

Northwest Institute of Nuclear Technology
Xi'an, 710024, China
srxh_bingwen@aliyun.com, ninghuisun@aliyun.com, pine976@163.com, caochenhyun12@163.com,
dtzmq_126@126.com

Abstract – In this paper distributed parameter equivalent circuits are developed for linear dipoles, dielectric coated dipoles and lumped loaded dipoles. Theoretical solutions for each distributed parameter and the reasonable non-uniform segmentation of antennas serve as the foundation for the derivation. The accomplished validations of the modeling procedures indicate that the given equivalent circuits are capable of correctly describing dipole antennas in frequency and time domains, with the advantages of wideband, frequency independence and unambiguous physical meaning. Relying on the presented equivalent circuits, broadband issues such as simulating input impedance, predicting equivalent lengths and computing transient responses of dipole antennas can be readily addressed. In addition, the circuit model provides helpful insights into the analysis and design for the loaded dipole antennas.

Index Terms – dipole antenna, distributed parameter, equivalent circuit, non-uniform segmentation, receiving antenna, transient response.

I. INTRODUCTION

Utilizing equivalent circuits to analyze an antenna has the advantages of fast operation speed, high efficiency and less consumption of computational resources. Precise and effective equivalent circuits have emerged as powerful methods for investigating antenna radiation characteristics [1–5], coupling effects between array elements [6–7], transient response problems [8–10], loaded antennas [11–13], and antenna design and optimization [14–20]. Equivalent circuit modeling is a significant area of interest within the field of antennas. Recent studies have demonstrated that the interests of equivalent circuit modeling are wideband, frequency-independent, simple circuit topology, ease of parameter computation, clear physical meaning, and the ability to explore transient issues. For example, reference [21] sought to acquire circuit element values with least amount of effort, references [2, 22] placed emphasis on wideband, precision and clear physical meaning, and equivalent circuits in [23–24] are frequency independent realized by the proposed empirical formulas.

Usual modeling procedures can be summarized from past literature as follows: first acquire the input impedance from antenna geometry, next deal with numerical methods, intuitive approaches or comprehensive methods, then circuit topologies are suggested and the element parameters are solved, and finally verification is undertaken. Relying on extensive optimization, numerical methods can give high accuracy, but at the expense of complicated circuit topologies and absence of physical meaning. As an example, with support of a genetic algorithm, reference [25] proposed a complex equivalent circuit for dipoles, but in which a negative capacitance was introduced. The key idea of intuitive approaches is to employ reasonable RLC circuits to match the resonance phenomenon of a dipole. In this way, the circuit configurations are always simple, such as the four-element circuit in [26] and the five-element circuit in [27], however, these circuits suffered from lack of wideband precision, and the parameter solution relies on empirical formulas [23, 28] or a large number of simulations [29]. Comprehensive methods employ flexible and suitable use of both intuitive and numerical approaches. For instance, the calculation of parameter values for a plasma dipole is conducted via a genetic algorithm [30]. A wideband circuit is modeled with eigenmode methods in [2], in which the Moment Method is utilized to compute the characteristic modes.

It is worth mentioning that the five-element equivalent circuit proposed by Humaid in [27] has triggered many studies due to its concise circuit topology and clear physical meaning. For example, equivalent circuits of a dipole in a lossy medium and dielectric coated wire antenna are developed by Liao in [23, 31]. The five-element circuit model is employed to explore the radiation characteristics of the plasma dipole and monopole in [1, 30] respectively. Moreover, transient responses of dipoles excited by EMP were investigated and revealed

in [8] on the basis of the five-element circuit. However, intuitive models only work with time-harmonic occasions [2, 27], broadband or transient problems remain poorly understood, despite being of wide concern in electromagnetic vulnerability. In addition, intuitive models for analyzing lumped-loaded antennas are still unclear.

Taken together, the methods mentioned above are knowing the results in advance, namely the impedance characteristics of the antenna, then exploring the modeling approaches from the "results". By contrast, the distributed parameter equivalent circuit can be attained from antenna geometry immediately, and theoretically there is a wideband and frequency independent model [33]. To investigate the radiation characteristics of a monopole and the propagating properties of voltage and current on a dipole, the distributed parameter equivalent circuits are developed in [4] and [34], respectively, and these studies highlight the potential advantages of the distributed parameter equivalent circuit in antenna transient analysis. However, previous studies have failed to address the question of modeling procedure, critical factors and parameter solutions, e.g. equivalent circuit with uniform segmentation in [4] could not accurately describe the details of the antenna, and only one radiation resistance is involved in the circuit in [34], which is inconsistent with reality.

This study systematically reviews the modeling approaches for antenna equivalent circuits, aiming to present a wideband circuit model with simple topology and clear physical meaning. The subsequent structure of this study takes the form of four sections. Section II demonstrates the theoretical calculation of distributed parameters of a dipole. Section III establishes the equivalent circuits of radiating and receiving dipole antenna and explores how the segmentation affects the modeling accuracy. In Section IV, the validation of the present equivalent circuits is operated through experiments and numerical simulations in frequency and time domains, respectively. The final section sets out further research on the distributed parameter equivalent circuits of the dielectric coated dipole and lumped loaded dipole, with some numerical results.

II. SOLUTION FOR DISTRIBUTED PARAMETERS

It is a widely held view that the distributed parameters of dipole antenna include distributed capacitance, inductance, resistance and negligible conductance, and these values are determined by dipole geometry. In the following discussions and calculations, it is assumed that a linear dipole is placed in the cylindrical coordinate system and along the z axis, with pole length l_0 and pole radius r_0.

A. Distributed capacitance

The uniqueness theorem states that the electrical potential φ around the dipole can be solved while the pole potentials and the zero-potential boundary are given. With the support of φ which meets the Laplace equation in free space, the charge density on the pole surface can be acquired. Therefore, the distributed capacitance of the dipole is obtained in terms of definition and electromagnetic constitutive relations,

$$C(z) = -\varepsilon_0 \frac{\pi r_0}{V_0} \frac{\partial \varphi(z)}{\partial n}, \qquad (1)$$

where ε_0 is the permittivity of vacuum, $\varphi(z)$ represents the potential around the dipole, and V_0 is the known pole potential. The Laplace equation in the cylindrical coordinate system is as follows, and only relating to r and z direction,

$$\nabla^2 \varphi = \frac{\partial^2 \varphi}{\partial r^2} + \frac{1}{r} \frac{\partial \varphi}{\partial r} + \frac{\partial^2 \varphi}{\partial z^2} = 0. \qquad (2)$$

Next, the central difference is utilized to replace the differential in equation (2),

$$\varphi_{i,j} = \frac{(\varphi_{i-1,j} + \varphi_{i+1,j} + \varphi_{i,j-1} + \varphi_{i,j+1})}{4}$$
$$+ \frac{(\varphi_{i+1,j} - \varphi_{i-1,j})}{8i}. \qquad (3)$$

Finally, the distributed capacitance of the dipole antenna can be calculated via equation (1) and (3).

Take a dipole antenna with pole length $l_0 = 0.1$ m and pole radius $r_0 = 0.001$ m as an example. Figure 1 plots the distributed capacitance per unit length varying along pole length. It is observed that the distributed capacitance at both ends grows sharply, while the middle part remains steady. Approximately, the dipole antenna can be divided into three sectors, the sector near the feeding gap with length of $0.2l_0$, the terminal sector with length of $0.1l_0$ and the medial sector with the remaining length. This variation suggests further studies to evaluate the impact of the two former sectors on the equivalent circuit modeling.

B. Distributed inductance

The dipole antenna is considered as a short wire with total length $L_0 = 2l_0$ to derivate the distributed inductance, including external and internal inductance.

The radial current distribution within the wire is concentrated on its axis to determine the external inductance. It is assumed that the magnetic induction density at point P outside the wire is dB, which is contributed by current element Idz on the dipole antenna. Hence, the total magnetic induction density B_p can be carried out via integrating dB along the short wire,

$$B_p = \int_0^{L_0} dB = \frac{\mu_0 I}{4\pi r_p} \left[\frac{L_0 - z_p}{\sqrt{r_p^2 + (L_0 - z_p)^2}} + \frac{z_p}{\sqrt{r_p^2 + z_p^2}} \right], \qquad (4)$$
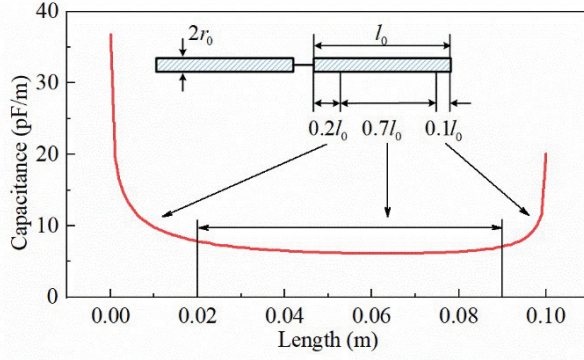
Fig. 1. Distributed capacitance per unit length of the dipole varying along the pole length.

where μ_0 is the permeability of vacuum, r_p and z_p are the position depiction of point P in the cylindrical coordinate system. Next, integrating B_p along the short wire to gain the total magnetic linkage outside the wire, then, the external inductance per unit length is derived as,

$$L_e = \frac{\mu_0}{2\pi} \left[\ln \frac{L_0 + \sqrt{L_0^2 + r_0^2}}{r_0} - \frac{\sqrt{L_0^2 + r_0^2}}{L_0} + \frac{r_0}{L_0} \right]. \quad (5)$$

Due to the dipole antenna operating at frequencies in the order of MHz and above, the surface effect depth is almost zero, which leads to little internal inductance. Therefore, the distributed inductance of a dipole antenna is principally its external inductance.

C. Distributed resistance

Resistance consumes power in the equivalent circuit to represent the thermal loss power and the radiated power of an antenna. Compared with the latter, the former can be omitted in circuit modeling, hence, only the radiation resistance is taken into account, and this is the major contributor that the dipole is deemed to be a lossy transmission line. From the previous perspective, the concerned resistance is also distributed, and can be derived approximately based on current distribution and other distributed parameters.

Ignoring the variation of current distribution caused by radiative process, the current on the dipole is similarly sinusoidal,

$$I(z) = I_0 \sin \left[\beta \left(l_0 - |z| \right) \right], \quad (6)$$

where I_0 refers to current amplitude and β is the propagation constant.

In an attempt to derivate the distributed resistance, the dipole antenna is separated into several segments of equal length, with each radiation resistance represented by R_f. Then, the total radiant power at the operating frequency of the dipole antenna is demonstrated as follows,

$$P_f = \int_0^{l_0} \frac{1}{2} I_0^2 \sin^2 \left[\beta \left(l_0 - |z| \right) \right] dz R_f. \quad (7)$$

The radiant power can also be described utilizing lumped radiation resistance R_l, which is usually 73 Ω at the first resonance frequency of the dipole antenna [35]. Thus, distributed radiation resistance is denoted as,

$$R_f = \frac{2R_l}{l_0 \left[1 - \sin \left(2\beta l_0 \right) / 2\beta l_0 \right]}. \quad (8)$$

Equation (8) reveals that the key to carry out the distributed resistance is the propagation constant β, which is related to the attenuation constant α,

$$\beta = \frac{2\pi}{\lambda} \sqrt{\frac{1}{2} \left[1 + \sqrt{1 + \frac{\alpha^2 \lambda^2}{\pi^2}} \right]}, \quad (9)$$

where λ is the operating wavelength of the dipole. The lossy transmission line theory shows that α is associated with antenna distributed resistance,

$$\alpha = \frac{R_f}{2Z_c} = \frac{R_f}{2\sqrt{L_e/C}}, \quad (10)$$

where L_e and C are the distributed capacitance and inductance respectively, Z_c is the characteristic impedance along the dipole, and which can be replaced approximately by the average characteristic impedance of the parallel two-wire transmission line,

$$Z_c \approx \overline{Z_c} = 120 \left(\ln \left(2l_0/r_0 \right) - 1 \right). \quad (11)$$

Substituting equation (11) into (10) and combining with equation (8), the attenuation constant can be derived as,

$$\alpha = \frac{R_l}{120 \left(\ln \left(2l_0/r_0 \right) - 1 \right) l_0 \left[1 - \sin \left(2\beta l_0 \right) / 2\beta l_0 \right]}. \quad (12)$$

Next, by substituting equation (9) into (12) and employing the numeric iteration, the attenuation constant is obtained. Finally, the distributed radiation resistance of dipole antenna can be attained from equation (10),

$$R_f = 2\alpha \cdot \sqrt{L_e/C}. \quad (13)$$

What stands out in these deduced results is that the solution of each distributed parameter is frequency independent. In particular, the complete calculation of the distributed radiation resistance is suggested, which is a significant result, this course not having previously been described.

III. EQUIVALENT CIRCUITS

Referring to the transmission line equivalent circuit, the distributed parameter equivalent circuit for a radiating dipole antenna is derived easily, as drawn in Fig. 2, containing n segments, and the circuit elementary cell is marked by a red dotted rectangular box.

The two branches up and down of the circuit in Fig. 2 signify the two poles of the antenna, which reveals a distinct physical meaning of geometry. V is the drive voltage on the feeding point and R_k is the feeding impedance, with the value of 50 Ω typically. C_1,
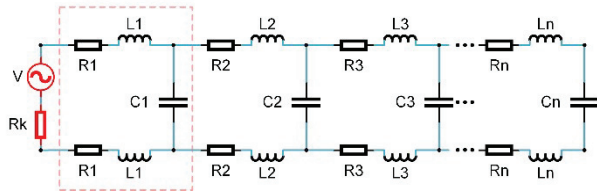
Fig. 2. Distributed parameter equivalent circuit model for radiating dipole antenna.

$C_2 \ldots C_n$ connected in parallel are the actual capacitances of each segment, determined by the corresponding segment length l_i and distributed capacitance:

$$C_i = \int_{l_i} C(l) \, dl. \tag{14}$$

The same is true of L_i and R_i in the distributed parameter equivalent circuit.

Equation (14) illustrates that the segmentation of the dipole antenna is the other decisive factor for accurate circuit modeling, which will be discussed in depth next, and then, the equivalent circuit for receiving dipole antenna are demonstrated.

A. Segmentation of dipole antenna

Obviously, the circuit topology grows more complicated as the segments increases, meanwhile cursory segmentation sacrifices the modeling accuracy. Hence, different segmentation ways are considered.

First check uniform segmentation. Four dipole antennas with different pole lengths ranging from 0.1 m to 0.3 m and with the same pole radius of 0.005 m are taken as examples, and uniform segmentations with different segment lengths are handled with these dipoles. Then, corresponding distributed parameter equivalent circuits are established to earn resonances. For easier comparison, the four dipole antennas are simulated utilizing the finite integration method. To measure the modeling accuracy, the absolute difference values between the first resonant frequencies of equivalent circuits and simulations are carried out, represented by Δf_1. Without loss of generality, the ratio of the segment length l_i to the minimum wavelength λ_{min} is employed to describe the level of uniform segmentation. The smaller the ratio, the tinier the segmentation. Figure 3 displays the curves that Δf_1 of the four dipoles vary with the ratio l_i/λ_{min}.

What stands out in Fig. 3 is that Δf_1 of different dipoles exhibit the same variation, approaching to zero as the ratio l_i/λ_{min} decreases. Peculiarly, while the ratio l_i/λ_{min} is lower than or equal to 1/10, the difference Δf_1 is less than 20 MHz, meaning that the first resonance points obtained by equivalent circuits are in good agreement with the simulated results. For most cases, the circuit of uniform segmentation with $l_i/\lambda_{min} \leq 1/10$ is adequate to accomplish time-harmonic problems for dipole antennas.
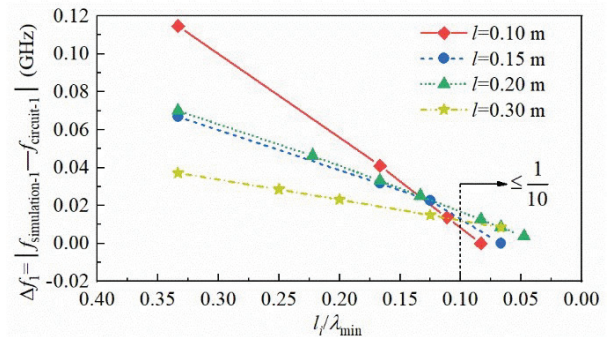
Fig. 3. Δf_1 of four dipoles varying with l_i/λ_{min}.

As inferred in Section II, distributed capacitance near the feeding gap and the terminal capacitance grows sharply, requiring fairly short segment length to handle the details mentioned. Uniform segmentation with pretty small l_i/λ_{min} can cope with this problem, but what follows is more intricate circuit topology containing massive RLC cells. Consequently, non-uniform segmentation is indispensable.

Take the antenna with pole length $l_0 = 0.1$ m in Fig. 3 as an instance, on the basis of uniform segmentation with l_i/λ_{min} less than 1/10, the sector near the feeding gap and the end sector are segmented again. Then, the circuit of non-uniform segmentation and the return loss are derived, and compared with other results in Fig. 4.
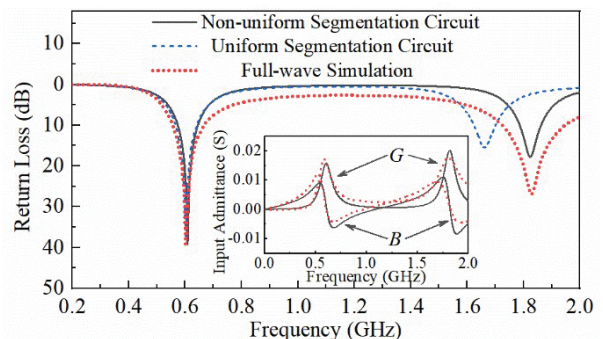
Fig. 4. Comparisons of return loss and input admittance obtained by simulation and equivalent circuits.

As can be seen from Fig. 4, consistency of the three methods at the first resonance point of the dipole antenna is achieved, which is a reasonable result and implies that further segmentation brings few effects to the first resonance. However, there is a significant difference at the second resonance, that is the circuit of non-uniform segmentation agrees well with the simulation, but differs from the circuit of uniform segmentation.

This phenomenon illustrates that simple uniform segmentation with the ratio l_i/λ_{min} less than 1/10 leads to

an equivalent circuit lack of wideband accuracy, and further segmentation to the sectors with distributed capacitance varying rapidly is of great significance in broadband equivalent circuit modeling. Meanwhile, the comparison of input admittance in Fig. 4 further proves that the equivalent circuit with the presented segmentation method exhibits wideband characteristics. Therefore, in order to handle the transient and broadband problems for a dipole antenna, the non-uniform segmentation is essential, and due to the middle sector of a dipole remaining unchanged in further segmentation, the complexity of circuit topology is reduced. However, previous reports make no attempt to consider the important role played by segmentation.

B. Equivalent circuit for receiving dipole

The principle of reciprocity in antenna theory states that the receiving mode characteristics are identical to those of transmitting mode. Thus, the distributed parameter equivalent circuit can also be employed to simulate the receiving antenna, with consideration of the induced electro motives generated by the incoming plane wave. As shown in Fig. 5, to construct the receiving equivalent circuit, the induced electro motives V_{ei} are added to the elementary cell marked in Fig. 2, with the element values unchanged.
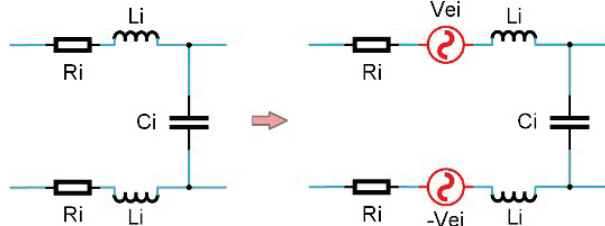
Fig. 5. Transformation of the elementary cell of equivalent circuit.

In general circumstances, the segment lengths are small enough, and each segment of the antenna can then be regarded as short dipole, leading to corresponding induced electro motives expressed approximately as follows:

$$V_{ei}(t) \approx E_i(t)l_i \cos\varphi, \qquad (15)$$

where E_i is the incident electromagnetic pulse, φ is the polarization angle, and l_i is the segment length. It is believed that the two branches up and down of the receiving circuit form a current loop, with the equal values and opposite signs of the induced electro motives of each segment.

IV. VALIDATION

To validate the presented equivalent circuit, two linear dipole antennas are measured and simulated in this

Table 1: Component values of the equivalent circuits for Dipole A and B

No.	Dipole A			Dipole B		
	C/pF	L/nH	R/Ω	C/pF	L/nH	R/Ω
1	0.058	2.81	0.97	0.110	8.17	2.64
2	0.040	3.28	1.47	0.056	7.66	3.30
3	0.033	3.28	1.62	0.093	15.33	7.23
4	0.026	2.81	1.46	0.084	15.33	7.66
5	0.050	6.09	3.33	0.079	15.33	7.90
6	0.046	6.09	3.48	0.15	30.65	16.15
7	0.085	12.19	7.29	0.074	15.33	8.13
8	0.073	11.25	6.92	0.075	15.33	8.08
9	0.073	11.72	7.35	0.078	15.33	7.91
10	0.072	11.72	7.42	0.098	15.33	7.09
11	0.072	11.72	7.44		—	
12	0.073	11.72	7.40		—	
13	0.079	12.19	7.53		—	
14	0.043	6.09	3.61		—	
15	0.055	6.09	3.20		—	

section. The two antennas are dipole A with pole length $l_a = 0.127$ m and pole radius $r_a = 0.0017$ m and dipole B with pole length $l_b = 0.156$ m and radius $r_b = 0.0013$ m. With the help of the theoretical solutions in the previous sections, the component values of the equivalent circuit for the two dipoles are displayed in Table 1, and the numerical simulations are operated via finite integration techniques.

A. Reflection coefficient

Reflection coefficients of dipole A and dipole B in frequency range of 1 MHz to 2 GHz are swept utilizing a VNA in microwave anechoic chamber. Then, the measurements are compared with the results carried out by equivalent circuits and simulations in Fig. 6. It is quite clear that, for the two dipoles, the results of equivalent circuits are consistent with the measurements and simulations.
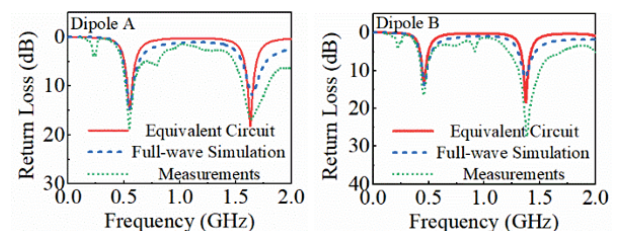
Fig. 6. Comparison of reflection coefficients for the two dipole antennas.

B. Effective length

The effective length of the antenna is usually employed to determine the induced voltage on the open-circuit terminals and also it is related to the far-zone field radiated by the antenna [35]. Both the equivalent circuit and numerical simulation can easily reveal effective lengths of the two dipoles. Measurements are handled based on the two-antenna method, and the measurements scene is shown in Fig. 7.
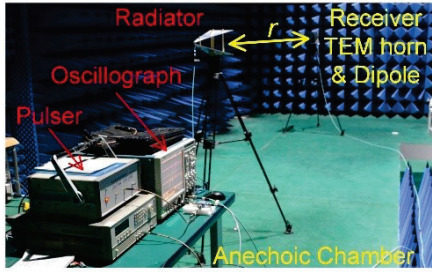
Fig. 7. Measurements scene of effective length.

Firstly, two identical TEM horns are adopted as radiating and receiving antennas respectively, and then the effective length of the TEM horn antenna can be derived via the two-antenna method as follows,

$$h_e(\omega) = \sqrt{\frac{2\pi r Z_t S_{21-t}(\omega)}{-j\omega\mu}} e^{-jkr}, \qquad (16)$$

where r is the distance between radiating and receiving TEM horns, $Z_t = 50\ \Omega$ is terminal load of the receiving horn, $S_{21-t}(\omega)$ is the transmission coefficient between the two horns which is measured by vector network analyzer, μ is the permeability of vacuum.

Keeping the measurement configuration unchanged, replace the receiving horn by dipole A and B in sequence. Then, the corresponding transmission coefficients are measured. On combining the measured results with $h_e(\omega)$, we deduce the effective lengths of the dipoles,

$$h_d(\omega) = S_{21-d}(\omega) \frac{2\pi r Z_t}{-j\omega\mu e^{-jkr}} \frac{1}{h_e(\omega)}. \qquad (17)$$

Comparisons of the effective lengths for dipole A and B are depicted in Fig. 8. It is indicated that the effective lengths derived by equivalent circuits are mainly consistent with the simulated and measured results, only a few discrepancies are observed between the measurements and the other two methods, which may be caused by measurement inaccuracies.

C. Transient response

To examine the suitability of handling with broadband problems via equivalent circuit, transient responses of the two dipoles are demonstrated in this section. The experiment configuration is the same as Fig. 7.
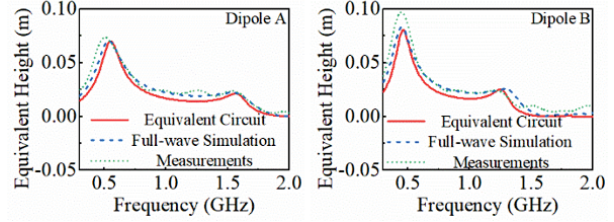
Fig. 8. Comparisons of the derived effective lengths for dipole A and B.
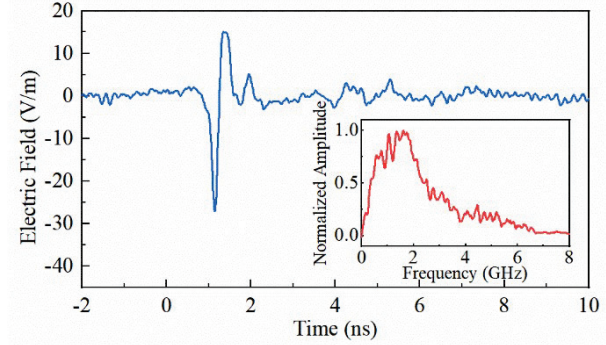
Fig. 9. Incident E-field wave and the normalized spectrum.

Figure 9 shows the measured incident E-field, generated by an ultra-wideband pulser and a radiator. Transient responses are attained with polarization matching and the arrival direction aiming at the maximum reception direction of dipoles, and compared with simulated and circuital transient responses, as depicted in Fig. 10.
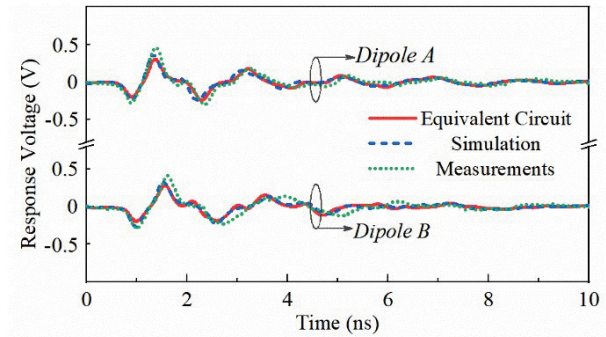
Fig. 10. Transient voltage responses of the two dipoles.

From the graph above, we can see that, for each dipole, good coherence of the transient response variations obtained by three methods are observed, both the pulse of duration and oscillating feature positions on waves.

These validations highlight that the solutions of distributed parameters directly from antenna geometry and

the modeling procedure are proper on the whole. Also, it proves that the presented equivalent circuit exhibits wideband accuracy, which is capable of being utilized to predict effective length and to investigate transient problems for dipoles.

V. APPLICATION

In this section, the distributed parameter equivalent circuits for a dielectric coated dipole and a lumped loaded dipole are derived and discussed as an application of the presented circuit model.

A. Circuit for dielectric coated dipole

Dielectric coating can protect antennas from corrosion, and is also widely applied to antenna miniaturization. For dipole antennas, dielectric coating just brings mutations to the distributed parameters, with the circuit topology unchanged, for radiating and receiving roles.

First derive the distributed parameters. A dielectric coating dipole can be transformed into a dipole with a purely magnetic coating, as demonstrated in [36], using a quasi-static approximation method. A purely magnetic coating causes little impact on capacitance of the dipole, so that a dielectric coated dipole can be further transformed into a dipole without any coating to solve its distributed capacitances. Figure 11 draws the cross sections of the three mentioned dipoles and the equivalence relationships among them. Notably, the materials considered here are homogenous, isotropic and low-loss.
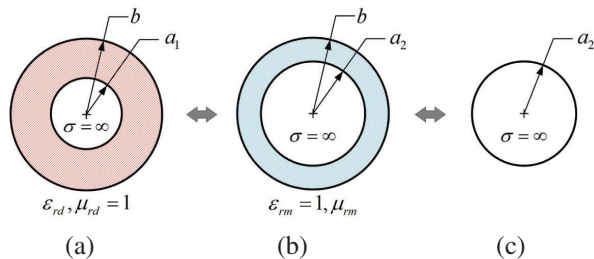
Fig. 11. Cross sections of dipoles. (a) dipole with coating dielectric, (b) dipole with coating magnetic material, and (c) dipole without any coating.

As shown in Fig. 11, the dipole with a coating of magnetic material is the equivalent one to the dipole in Fig. 11 (a), with the outer radius of coating b unchanged, and the inner radius a_1 is changed to a_2,

$$a_2 = b \left(a_1/b \right)^{1/\varepsilon_{rd}}, \qquad (18)$$

ε_{rd} becomes $\varepsilon_{rm} = 1$, and μ_{rd} becomes μ_{rm},

$$\mu_{rm} = \varepsilon_{rd}\mu_{rd}. \qquad (19)$$

Taking away the magnetic coating, the dipole in Fig. 11 (b) is transformed to the third dipole antenna, without changing the radius a_2. Next, relying on the presented method in Section II.A, the distributed capacitance of the dielectric coating dipole can be obtained by

calculating the distributed capacitance of the dipole without any coating in Fig. 11 (c).

The distributed inductance of the dielectric coated dipole comprises the inductance of the dipole in Fig. 11 (c) and the additional inductance per unit length brought by the magnetic coating in Fig. 11 (b). The former represented by L_m can be calculated via equation (5), and the latter has been induced in [37],

$$L_a = \frac{\mu_0}{2\pi} [\mu_{rm} - 1] \ln \left(\frac{b}{a_2} \right). \qquad (20)$$

In general, distributed resistance engenders little effect to antenna resonances, so that the solution of distributed resistance for a dielectric coated dipole is the same as the dipole without any coating.
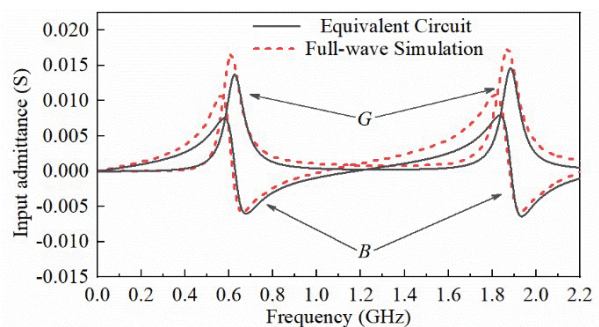
Fig. 12. Input conductance (G) and susceptance (B) of the dielectric coated dipole.

The considered sample geometry is a center-driven wire antenna with pole length of 0.1 m and pole radius of 0.001 m, covered with dielectric material of relative permittivity $\varepsilon_{cd} = 3$ and outer radius is 0.002 m. Finite integration techniques are employed to simulate the input admittances of the antenna and then compared with the results gained by the distributed parameter equivalent circuit, as drawn in Fig. 12, in which reasonable agreements are observed for the two methods.

To investigate the transient response of a receiving role, a Gaussian pulse with the rise time of 0.3 ns and amplitude of 1 kV/m is utilized as the incident E-field. Figure 13 compares the output voltage responses attained by full wave simulation and its equivalent circuit, agreements are achieved, and only the amplitudes are slightly discrepant.

B. Circuit for lumped loaded dipole

Loading lumped elements can significantly improve radiation performances [38–41]. In most situations, lumped loading position is not reflected by a lumped parameter equivalent circuit precisely, but it can be achieved by a distributed parameter equivalent circuit, relying on clear geometric physical meaning. Thus, it is
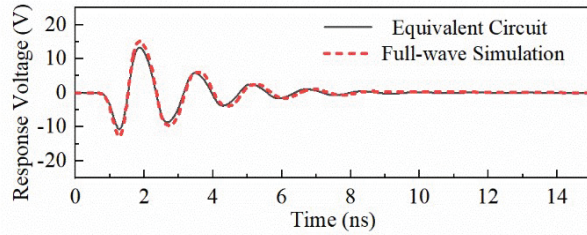
Fig. 13. Time domain responses of the dielectric coated dipole excited by Gaussian pulse.

foreseeable that the distributed parameter equivalent circuit is a convenient and efficient way to investigate the lumped loaded dipole antenna.

In this section, a dipole loaded with a parallel RLC resonant circuit is demonstrated. The RLC resonant circuit is located at the symmetrical positions of the antenna poles, as shown in Fig. 14, in which the loaded component values are $R_0 = 1$ kΩ, $L_0 = 20$ nH, $C_0 = 5.5$ pF.
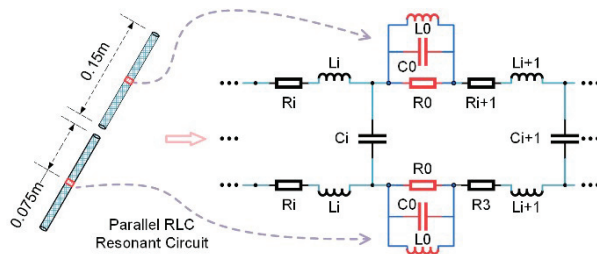
Fig. 14. A dipole loaded with parallel RLC circuit.

The input admittances of the antenna gained by simulation and the equivalent circuit are plotted and compared in Fig. 15, where the agreements and three resonances are observed, two of them are the intrinsic resonant points of the dipole antenna, and the other one is the resonance caused by the loaded RLC resonant circuit.

Using the same Gaussian pulse in Section V.A as the incident E-field, the output voltage responses and the voltages in loaded resistance are carried out by numerical simulation and equivalent circuit, and compared in Fig. 16. It is indicated that the transient voltage responses obtained by the two methods are grossly consistent, so are the voltages on R_0, while the amplitudes are slightly different.

This section demonstrates two applications of the distributed parameter equivalent circuit, for simulating a dielectric coated dipole and a lumped loaded dipole respectively. Final results indicate that the equivalent circuits can accurately describe the performances in frequency and time domain of the two antennas. In par-
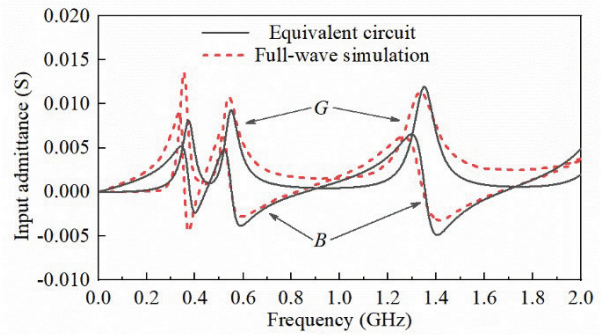
Fig. 15. Input conductance (G) and susceptance (B) of the lumped loaded dipole antenna.
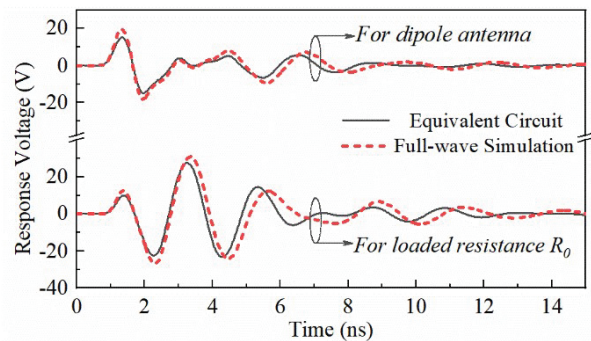
Fig. 16. Time domain responses of lumped loaded dipole excited by Gaussian pulse.

ticular, the presented equivalent circuit provides useful insights into the design of a lumped loaded dipole, e.g. the loading component values and loading position can be optimized by parameter sweeping utilizing circuit simulation software quickly and efficiently, with less computational time and resources.

VI. CONCLUSION

The aim of this paper is to contribute to the systematic and complete understanding and modeling of distributed parameter equivalent circuits for dipoles. All distributed parameters have been theoretically derived as the modeling foundation, and reasonable non-uniform segmentation is employed to increase available bandwidth and reduce the complexity of circuit topology. The validations operated in frequency and time domains proves that the presented equivalent circuits and modeling approaches are accurate and have the advantages of broadband, frequency independence and clear physical meaning, which meets modeling expectations. Utilizing this equivalent circuit, broadband problems such as simulating input impedance and investigating transient responses can be carried out. Finally, we extend the distributed parameter equivalent circuit to dielectric

coated dipoles and lumped loaded dipoles, which provides useful insights into the analysis and design for the two dipoles.

Future work focuses on modeling distributed parameter equivalent circuits for wideband antennas, as well as predicting the near-field radiation characteristics distribution of radiating antenna and investigating the out-of-band coupling characteristics of receiving antenna based on distributed parameter equivalent circuits.

REFERENCES

[1] F. Sadeghikia, "Analysis of plasma monopole antenna using numerical method and an equivalent circuit," *IEEE Antennas Wireless Propagt. Lett.*, vol. 16, pp. 1711-1714, 2017.

[2] J. J. Adams and J. T. Bernhard, "Broadband equivalent circuit models for antenna impedances and fields using characteristic modes," *IEEE Trans. Antennas Propagat.*, vol. 61, no. 8, pp. 3985-3994, Aug. 2013.

[3] M. H. Ucar, A. Sondas, and Y. E. Erdemli, "Dual-band loop-loaded printed dipole antenna with a wideband microstrip balun structure," *Applied Computational Electromagnetics Society (ACES) Journal*, vol. 27, no. 6, pp. 458-465, June 2012.

[4] J. Bemardes, F. Peterkin, B. Hankla, and J. Latess, "Antenna circuit model for time-domain transient analysis," *IEEE 12th International Pulsed Power Conference*, Monterey, CA, pp. 260-263, June 1999.

[5] M. H. Ucar and Y. E. Erdemli, "Triple-band microstripline-fed printed wide-slot antenna for WiMAX/WLAN operations," *Applied Computational Electromagnetics Society (ACES) Journal*, vol. 29, no. 10, pp. 793-800, Oct. 2014.

[6] Y. Tak, J. Park, and S. Nam, "Equivalent circuit of a two-element spherical small antenna," in *IEEE International Symposium on Antennas and Propagation*, North Charleston, SC, pp. 1-4, June 2009.

[7] B. Riviere, H. Jeuland, and S. Bolioli, "New equivalent circuit model for a broadband optimization of dipole arrays," *IEEE Antennas Wireless Propagt. Lett.*, vol. 13, pp. 1300-1304, June 2014.

[8] Y. Liao, X. J. Ying, G. C. Shi, and Y. Wang, "Time domain response analysis with equivalent circuit models for dipole antennas under EMP," *IEEE 6th International Symposium on Antennas and Propagation and EMC Technology*, Shanghai, pp. 379-382, Oct. 2015.

[9] Y. Xiao, F. Zhu, S Zhuang, and Y. Yang, "Research on EMI of traction network transient current pulse on shielded cable terminal load," *Applied Computational Electromagnetics Society (ACES) Journal*, vol. 37, no. 4, pp. 485-496, Apr. 2022.

[10] B. Li, J. J. Wang, X. W. Song, and D. L. Su, "Equivalent circuit model of frequency-domain responses with external field," *IEEE International Symposium on Electromagnetic Compatibility*, Dresden, pp. 761-766, Aug. 2015.

[11] B. R. Strickland and N. F. Audeh, "Diode-loaded dipole antenna modeling and design," *IEEE Trans. Antennas Propagat.*, vol. 41, no. 3, pp. 333-337, Mar. 1993.

[12] B. R. Strickland and N. F. Audeh, "Numerical analysis technique for diode-loaded dipole antennas," *IEEE Trans. Electromagn. Compat.*, vol. 35, no. 4, pp. 480-483, Nov. 1993.

[13] S. Palud, F. Colombel, M. Himdi, and C. L. Meins, "Circuit modeling of a small broadband conical antenna," *IEEE Antennas Wireless Propagt. Lett.*, vol. 8, pp. 96-99, Jan. 2009.

[14] R. Li, T. Wu, B. Pan, K. Lim, J. Laskar, and M. M. Tentzeris, "Equivalent-circuit analysis of a broadband printed dipole with adjusted integrated balun and an array for base station applications," *IEEE Trans. Antennas Propagat.*, vol. 57, no. 7, pp. 2180-2184, July 2009.

[15] M. Ojaroudi and E. Mehrshahi, "Bandwidth enhancement of small square monopole antennas by using defected structures based on time domain reflectometry analysis for UWB applications," *Applied Computational Electromagnetics Society (ACES) Journal*, vol. 28, no. 7, pp. 620-627, July 2013.

[16] H. C. Jing, X. J. Xu, and Y. E. Wang. "Direct antenna modulation (DAM) with switched patch antenna performance analysis," *Applied Computational Electromagnetics Society (ACES) Journal*, vol. 29, no. 5, pp. 368-382, May 2014.

[17] J. Zolghadr, Y. Cai, and N. Ojaroudi, "UWB slot antenna with band-notched property with time domain modeling based on genetic algorithm optimization," *Applied Computational Electromagnetics Society (ACES) Journal*, vol. 31, no. 8, pp. 926-932, Aug. 2016.

[18] K. H. Yeap and W. Ismail, "Analytical model for E-shaped microstrip patch antenna," *Applied Computational Electromagnetics Society (ACES) Journal*, vol. 32, no. 4, pp. 332-338, Apr. 2017.

[19] P. Nayeri, A. Elsherbeni, R. Hasse, and D. Kajfez, "Half-loop segmented antenna with omni-directional hemispherical coverage for wireless communications," *Applied Computational Electromagnetics Society (ACES) Journal*, vol. 33, no. 2, pp. 123-126, Feb. 2018.

[20] N. R. Kumar, P. D. Sathya, S. K. A. Rahim, and A. A. Eteng, "Reduced cross-polarization patch

antenna with optimized impedance matching using a complimentary split ring resonator and slots as defected ground structure," *Applied Computational Electromagnetics Society (ACES) Journal*, vol. 36, no. 6, pp. 718-725, June 2021.

[21] T. L. Simpson, "A wideband equivalent circuit electric dipoles," *IEEE Trans. Antennas Propagat.*, vol. 68, no. 11, pp. 7636-7639, Nov. 2020.

[22] T. L. Simpson, "Equivalent circuits for electric dipoles," *IEEE International Symposium on Antennas and Propagation and North American Radio Science*, Montreal, QC, pp. 443-444, July 2020.

[23] Y. Liao, T. H. Hubing, and D. L. Su. "Equivalent circuit for dipole antennas in a lossy medium," *IEEE Trans. Antennas Propagat.*, vol. 60, no. 8, pp. 3950-3953, Aug. 2012.

[24] O. O. Olaode, W. D. Palmer, and W. T. Joines, "Characterization of meander dipole antennas with a geometry-based, frequency-independent lumped element model," *IEEE Antennas Wireless Propagt. Lett.*, vol. 11, pp. 346-349, 2012.

[25] B. Long, P. Werner, and D. Werner, "A simple broadband dipole equivalent circuit model," *IEEE International Symposium on Antennas and Propagation and National Radio Science*, Salt Lake City, UT, pp. 1046-1049, July 2000.

[26] T. G. Tang, Q. M. Tieng, and M. W. Gunn, "Equivalent circuit of a dipole antenna using frequency-independent lumped elements," *IEEE Trans. Antennas Propagat.*, vol. 41, no. 1, pp. 100-103, Aug. 1993.

[27] M. Hamid and R. Hamid, "Equivalent circuit of dipole antenna of arbitrary length," *IEEE Trans. Antennas Propagat.*, vol. 45, no. 11, pp. 1695-1696, Nov. 1997.

[28] B. H. Li and Q. Zhu, "Equivalent circuits of dipole and periodic metal rod array," *IEEE MTT-S International Microwave Symposium*, Baltimore, MD, pp. 1-4, June 2011.

[29] K. Rambabu, M. Ramesh, and A. T. Kalghatgi, "Broadband equivalent circuit of a dipole antenna," *IEE Proc.-Microw. Antennas Propagt.*, vol. 146, no. 6, pp. 391-393, Dec. 1999.

[30] M. M. Badawy, H. A. E. Malhat, S. H. Zainud-Deen, and K. H. Awadalla, "A simple equivalent circuit model for plasma dipole antenna," *IEEE Trans. Plasma Sci.*, vol. 43, no. 12, pp. 4092-4098, Dec. 2015.

[31] Y. Liao, T. H. Hubing, and D. L. Su, "Equivalent circuit with frequency-independent lumped elements for coated wire antennas," *IEEE Trans. Antennas Propagat.*, vol. 60, no. 11, pp. 5419-5423, Nov. 2012.

[32] B. W. Wang, H. Ning, Y. J. Yan, Z. Liu, F. H. Huang, and C. Y. Cao, "Analyzing out-of band response characteristics of dipole antenna by equivalent circuit," *Modern Applied Physics*, vol. 9, no. 1, pp. 75-81, Mar. 2018.

[33] H. Zhang, J. H. Wang, and W. Y. Liang, "Study on the applicability of extracted distributed circuit parameters of non-uniform transmission lines by equivalent circuit method," *Journal of Electromagnetic Waves and Applications*, vol. 22, no. 5, pp. 839-848, 2008.

[34] J. H. Wang, "Analysis of the propagating properties of pulse voltage and current on dipole antennas by equivalent circuit method," *Acta Physica. Sinica.*, vol. 49, no. 9, pp. 1693-1701, Sept. 2000.

[35] C. A. Balanis, *Antenna Theory: Analysis and Design*, John Wiley & Sons, Hoboken, NJ, USA, 2005.

[36] B. D. Popović and A. Nešić, "Generalisation of the concept of equivalent radius of thin cylindrical antennas," *IEE Proceedings*, vol. 131, no. 3, pp. 153-158, June 1984.

[37] J. Moore and M. A. West, "Simplified analysis of coated wire antennas and scatterers," *IEE Proc.-Microw. Antennas Propag.*, vol. 142, no. 1, pp. 14-18, Feb. 1995.

[38] W. Samuel and A. V. Pham, "The ultrawideband elliptical resistively loaded vee dipole," *IEEE Trans. Antennas Propagat.*, vol. 68, no. 4, pp. 2523-2530, Apr. 2019.

[39] Y. Xia, Y. Li, and W. Xue, "A low profile miniaturization low frequency wideband antenna using passive lumped elements loading," *Applied Computational Electromagnetics Society (ACES) Journal*, vol. 35, no. 1, pp. 31-37, Jan. 2018.

[40] W. Kang, K. W. Kim, and W. Kim, "A broad-band conductively-loaded slot antenna for pulse radiation," *IEEE Trans. Antennas Propagat.*, vol. 62, no. 1, pp. 33-39, Jan. 2013.

[41] W. Kang, K. W. Kim, and I. Kim, "Implementation and analysis of discretely loaded resistive dipoles using planar resistor technology," *IEEE Trans. Antennas Propagat.*, vol. 63, no. 11, pp. 5088-5093, Nov. 2015.

Binwen Wang was born in Gansu, China, in 1993. He received his B.S. degree in Nuclear Science from Xi'an Jiaotong University, Xi'an, China, in 2015, and his M.S. degree in Electro-magnetic Field and Microwave Technology from the Northwest Institute of Nuclear Technology, Xi'an, China, in 2017. He is currently an Engineer at the Northwest Institute of Nuclear Technology. His research interests include time-domain electromagnetics and ultra-wideband antenna.

Hui Ning was born in Zhejiang, China, in 1969. He received his M.S. and Ph.D. degrees in Nuclear Science and Technology from Tsinghua University, Beijing, China, in 1997 and 2001, respectively. He is currently a Professor at the Northwest Institute of Nuclear Technology, Xi'an China, specializing in time-domain electromagnetics and the pulsed power technique and its applications.

Youjie Yan was born in Henan, China, in 1982. He received his B.S. degree in Electronical Information Science and Technology from Xidian University, Xi'an China, in 2005, his M.S. degree in Electromagnetic Field and Microwave Technology from the Northwest Institute of Nuclear Technology, Xi'an, China, in 2008, and his Ph.D. degree in Plasma Physics from the University of Electronic Science and Technology of China, Chengdu, China. He is currently a Professor-level senior engineer. His research interests include time-domain electromagnetics and electromagnetic compatibility.

Chengyun Cao was born in Qinghai, China, in 1994. He received his B.S. and M.S. degrees in Electromagnetic Field and Microwave Technology from the National Defense University of Science and Technology, Changsha, China, in 2016. He is currently an Engineer at the Northwest Institute of Nuclear Technology, specializing in ultra-wideband antenna.

Meiqi Zhu was born in Jiangsu, China, in 1998. She received her B.S. degree in Electromagnetic Field and Microwave Technology from the National Defense University of Science and Technology, Changsha, China, in 2019. She is currently an Assistant Engineer at the Northwest Institute of Nuclear Technology, specializing in high power pulsers.

Design of a Retransmitted Chipless Tag based on Multi-state Resonators

Nengyu Huang[1,2] and Zhonghua Ma[1,*]

[1]School of Ocean Information Engineering
Jimei University, Xiamen, Fujian 361021, China
*mzhxm@jmu.edu.cn

[2]School of Navigation
Jimei University, Xiamen, Fujian 361021, China
huangny05@163.com

Abstract – In order to increase the encoding capacity and reduce the size of the tag, this paper proposes the frequency sharing method to design a retransmitted chipless tag, which is composed of N resonators, a coupled microstrip transmission line, and the orthogonal transmitting antenna and receiving antenna. A pair of the same size resonators is placed symmetrically on both sides of the coupled microstrip transmission line. M open-ended stubs (OES) with different combinations are embedded in each resonator to obtain different resonance frequencies. The frequency sharing multi-state resonators' chipless tags are designed where N=6, M=4, and the dimension of the tag is 46 mm $\times$ 30 mm, which can generate about 2^{12} codes. Simulation and measurement results show good agreement and feasibility of the tag design. The chipless tag is small in size, has large encoding capacity and is easy to print. This kind of tag has no silicon chip so the cost is low. It can be widely used in logistics, supermarkets and other fields to replace the barcode.

Index Terms – chipless tag, encoding capacity, frequency sharing, radio frequency identification, resonator.

I. INTRODUCTION

The Radio Frequency Identification (RFID) system is one of the core technologies in the field of the Internet of Things (IoT), which is mainly composed of a reader and tags. The reader is composed of a continuous wave transmitting circuit, a modulated wave receiving circuit, and reader antennas to extract the tag's identification (ID) and other data information. The tag is a data carrier that includes a tag antenna and silicon chip [1]. Once the reader is put into use, it does not need to be replaced, so its cost is fixed. However, the tags are attached to items so the quantity is huge. All of the tags are read by the same reader, so the cost reduction of the RFID system mainly depends on the cost of the tags [2]. The cost of the traditional chip-tags mainly depends on the cost of the silicon chip. The cost of silicon material and the production process of the chip are fixed, so the cost of the chip cannot be cut down. The high cost is the key obstacle for the application of the traditional chipped tag in low-price commodities (such as stamps, tickets and envelopes, etc.) [3]. Therefore, many scholars have begun to design chipless tags. The cost of chipless tags depends on the cost of the conductive material that constitutes the resonant circuits. Due to removing the tag's silicon chip, the cost of the chipless tag is drastically reduced, but it has the advantages of traditional chip tags, such as non-line-of-sight (NLOS) reading and automatic identification. This chipless tag system can also work under extreme conditions (such as high temperature and high humidity, etc.). However, it has deficiencies in terms of data capacity and tag size when compared with the traditional tags [4, 5].

Usually chipless tags are divided into two categories: time-domain (TD) [6–12] and frequency-domain (FD) [3, 13–24]. The TD chipless tag is mainly composed of two types, i.e. transmission delay line and surface acoustic wave (SAW) filter. The transmission delay line chipless tag works at the nanosecond level. Signal detection is difficult. At the same time, the encoding capacity is small, only one or a few bits. It is mainly used in anti-theft, access control, etc. [6]. Although a SAW chipless tag has high encoding capacity, it requires high-cost piezoelectric materials and cannot be printed directly [7]. Compared with the TD-based chipless solutions, the FD-based chipless tag has many advantages. In addition to easier signal detection and lower cost of the tag, it also potentially has a larger encoding capacity depending on the tag size and available spectrum.

Chipless tags based on the FD have two working methods: chipless tags extracting Radar Cross Section

(RCS) spectrum characteristics [13–17] and retransmitted chipless tags [3, 18–24]. The chipless tag based on RCS does not require receiving and transmitting antennas, and its RCS spectrum structure is responsible for loading the encoded information. The tag's encoding capacity is increased by adding resonators, but the coupling effect will be introduced at the same time. Theoretically, the reading distance of the RCS chipless tag will be very far, but it is limited by its actual environment and requires a complicated algorithm to separate the RCS signal of the tag in order to decode it. Moreover, other interference may also be introduced in a complex environment, so the chipless tag needs constant calibration. The retransmitted chipless tag requires two orthogonal ultra-wideband (UWB) antennas and relevant resonator circuits. The transmitting and receiving antennas are orthogonally polarized to each other. There is no interference between the receiving signal and transmitting signal of the tag, so the reader has the low bit error rate when reading chipless tags. The reading distance is further than the RCS chipless tag in the actual environment. The number of the traditional retransmitted chipless tag resonators is the same as the number of data bits. Increasing encoding capacity can be implemented by adding the number of resonators. The coupling effect between the resonators can be reduced by adjusting resonator intervals. Previous papers [3, 18] have proposed a 6-bit retransmitted chipless tag with spiral resonators. As the number of spiral resonators increased to 35, the encoding capacity is increased to 35 bits. Furthermore, the size of this chipless tag is enlarged correspondingly.

In order to improve the encoding capacity without increasing the dimension of the tag, the retransmitted chipless tag is proposed in this paper which is composed of frequency sharing multi-state resonators, wherein each resonator can provide more than two states. By using the sharing frequency method, the tag can provide larger encoding capacity with a smaller number of resonators. There is a ground plate on the back of the tag which can isolate the influence of the adhesive objects on the tag's performance. Chipless tags with a retransmitted structure have high sensitivity and long reading distance due to the gain of the antenna and the non-interference between the receiving and transmitting signals of the tag. The communication distance of the chipless tag with this structure is 30 cm. The tag can be widely used in logistics, supermarkets and other fields to replace the barcode.

II. WORKING PRINCIPLE OF THE RETRANSMISSION CHIPLESS TAG

Figure 1 is the working principle diagram of the retransmission chipless tag with multi-state sharing fre-
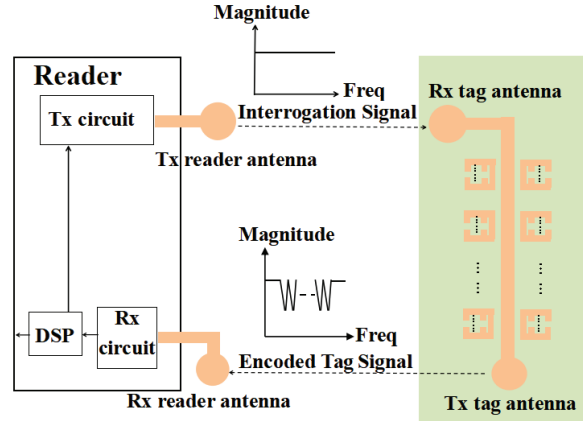
Fig. 1. Working principle of the retransmitted chipless tag with multi-state sharing frequency resonators.

quency resonators. The tag includes a vertically polarized receiving antenna, a horizontally polarized transmitting antenna, multi-state resonators and a coupled microstrip transmission line. The transmitting antenna of the reader transmits the UWB interrogation signal with a uniform spectrum to the chipless tag, and the receiving antenna of the tag receives the UWB interrogation signal and transfers it to the multi-state resonator coupling circuits by the microstrip transmission line. The multi-state resonator coupling circuits adopt cascaded multi-state resonators with M embedded OES to encode the data, which forms a series of spectral signatures in the UWB signal spectrum. At the same time, the data of the chipless tag is loaded into the spectral signatures of the UWB signal. The transmitting antenna of the chipless tag retransmits this UWB signal with encoded spectrum signatures back to the reader; then, the data information can be obtained by the decoding circuit and certain algorithms. The receiving and transmitting antennas of the reader are also orthogonally polarized to avoid the mutual interference between the transmitted signal and the received encoded signal in the reader. The transmitting antenna of the reader and the receiving antenna of the tag have the same polarization characteristic, and the receiving antenna of the reader and the transmitting antenna of the tag have the same polarization characteristic.

III. SIMULATION DESIGN

Figure 2 is the structural parameter diagram of the multi-state resonators of M=4. W_1 is the width of the coupled microstrip transmission line, t is the longitudinal interval between the embedded OES, and g and w_2 are the length and width of the OES, respectively. The length and width of all embedded OES are equal. d_1 is the distance between the resonator and the coupled microstrip

Fig. 2. Structural parameters diagram of the multi-state resonators.

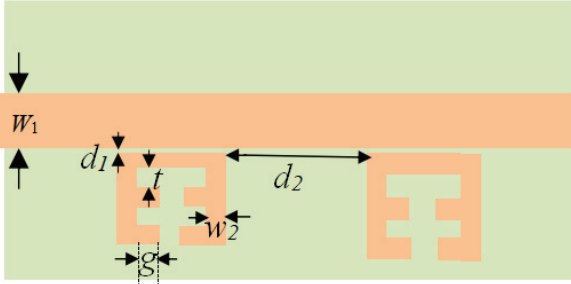transmission line, and d_2 is the distance between adjacent resonators. The RO4350 dielectric substrate has low loss, reasonable cost, small circuit size, good stability and consistency compared with other microwave substrates. The dielectric constant of 3.66 makes the circuit size not too large. The thickness of substrate is 0.508 mm, and a thin substrate can reduce the surface waves. Therefore, Rogers microwave board RO4350 (with ε_r=3.66, tan δ=0.004, h=0.508 mm) is selected as the substrate.

This chipless tag can also be printed directly on other low-cost dielectric substrates, such as packaging cartons, plastic bottles or glass. But the size of the resonator needs to be adjusted and the coding rules are not affected.

The characteristic impedance Z_0 of a single microstrip line in a homogeneous medium is expressed as follows [25]:

$$Z_0 = \frac{\eta}{2\pi\sqrt{\varepsilon_{re}}} \ln\left[\frac{F}{u} + \sqrt{1 + \left(\frac{2}{u}\right)^2}\right], \qquad (1)$$

$$F = 6 + (2\pi - 6)\exp\left[-\left(\frac{30.666}{u}\right)^{0.7528}\right], \qquad (2)$$

where ε_{re} is the effective dielectric constant, $\eta = 120\pi$, Ω is the wave impedance in free space, u is the ratio of the width of the microstrip to the height of the substrate ($u=W_1 / h$), F is a value related to the u, and

$$\varepsilon_{re} = \frac{\varepsilon_r + 1}{2} + \frac{\varepsilon_r - 1}{2}\left(1 + \frac{10}{u}\right)^{-ab}, \qquad (3)$$

where ε_r is the relative dielectric constant, a is a value related to u, and b is a value related to relative dielectric ε_r. The accuracy of this expression applies to $\varepsilon_r \leq 128$ and $0.01 \leq u \leq 10$. The equations of a and b are as follows [26]:

$$a = 1 + \frac{1}{49}\ln\left(\frac{u^4 + \left(\frac{u}{52}\right)^2}{u^4 + 0.432}\right) + \frac{1}{18.7}\ln\left(1 + \left(\frac{u}{18.1}\right)^3\right), \qquad (4)$$

$$b = 0.564\left(\frac{\varepsilon_r - 0.9}{\varepsilon_r + 3}\right)^{0.053}. \qquad (5)$$

From equation (1), the thickness of the dielectric substrate h=0.508 mm and the relative dielectric constant ε_r=3.66, then the width (W_1) of the Z_0=50 Ω microstrip transmission line can be obtained by the program code shown in Fig. 3.

```
10.    double Formula(double w1)
11.    {
12.        double re, a, b, F, a1, a2, F1;
13.        double r=3.66;      //Relative permittivity:r = 3.66
14.        double Z0=50;       //Characteristic impedance: Z0 = 50 Ω
15.        double h=0.508;     //Thickness of substrate: h = 0.508 mm
16.        a1=log((pow(w1/h,4)+pow(w1/(52*h),2))/(pow(w1/h,4)+0.432))/49;
17.        a2=log(1+pow(w1/(18.1*h),3))/18.7;
18.        a=1+a1+a2;
19.        b=0.564*pow((r-0.9)/(r+3),0.053);
20.        F1=exp(-pow((30.666*h/w1),0.7528));
21.        F=6+(2*3.1415-6)*F1;
22.        re=(r+1)/2+((r-1)/2)*pow((1+10*h/w1),(-a*b));
23.        return (60/sqrt(re))*log(F*h/w1+sqrt(1+pow(2*h/w1,2)))-Z0;
24.    }
25.    void Dichotomy(double n, double m)
26.    {
27.        double mid, result;
28.        mid=(n+m)/2;
29.        result = Formula(mid);
30.        if(result > 0.0001)
31.        {
32.            Dichotomy(mid, m);
33.        }
34.        else if(result < -0.0001)
35.        {
36.            Dichotomy(n, mid);
37.        }
38.        else
39.        {
40.            printf("w1=%.2lf mm", mid);
41.        }
42.    }
```

Fig. 3. Relevant code for numerically solving microstrip width.

Figure 3 is the program code for numerically solving the microstrip width. After ensuring the relative dielectric constant of the substrate, the thickness of the substrate and the characteristic impedance of the microstrip, the width W_1 of the microstrip with the characteristic impedance of 50 Ω is 1.11 mm using the dichotomy method. The structure parameters W_1, d_1, w_2, t and g are defined by continuous simulation and optimization through High-Frequency Structure Simulator
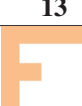
(HFSS) software. After adjusting the structural parameters, the resonant frequency interval of adjacent resonators is more than 250 MHz, which effectively reduces the mutual interference. Adjust the structural parameter d_2 by HFSS software to reduce the coupling effect between adjacent resonators. Through continuous optimization and adjustment of the resonators, the structural parameters of the multi-state resonator tag for frequency sharing are finally determined. The specific values of the structural parameters are shown in Table 1.

Table 1: Structural parameters of the multi-state resonator (unit: *mm*)

W_1	d_1	d_2	g	t	w_2
1.07	0.2	2.2	0.9	1	0.5

Different resonance frequencies can be obtained by various combinations of OES. When the maximum number of OES embedded in a resonator is 4, there are 14 structural combinations, as shown in Table 2. Among them, structures 2 and 3, structures 4 and 5, and structures 6 and 7, etc. are the same size and same resonance signature, respectively. Their equivalent circuits and resonance frequencies are the same as well. Therefore, there are only eight different resonance frequencies. But the adjacent resonance frequencies are quite close

Table 2: Structural combinations of a resonator with various amounts of embedded OES

Structure 1	Structure 2	Structure 3	Structure 4
Structure 5	Structure 6	Structure 7	Structure 8
Structure 9	Structure 10	Structure 11	Structure 12
Structure 13	Structure 14		

and may cause interference. Considering the above factors, for N=1 and M=4, the five structures of 1, 5, 8, 12 and 14 are selected in Table 2, thus five resonance frequencies are obtained correspondingly. N is the number of resonators of different sizes.

The simulation results of the resonator with N=1 and M=4 using an HFSS simulator are shown in Fig. 4, when w_2, g and t are 0.5, 0.9 and 1.0 mm, respectively. The curves with resonance frequencies f_1, f_2, f_3, f_4 and f_5 correspond to the resonators of structures 1, 5, 8, 12 and 14 in Table 2, respectively. The f_1-f_5 resonant frequency point includes 7.97, 8.46, 8.81, 9.22 and 9.58 GHz, which has the maximum notch depth of -20 dB.
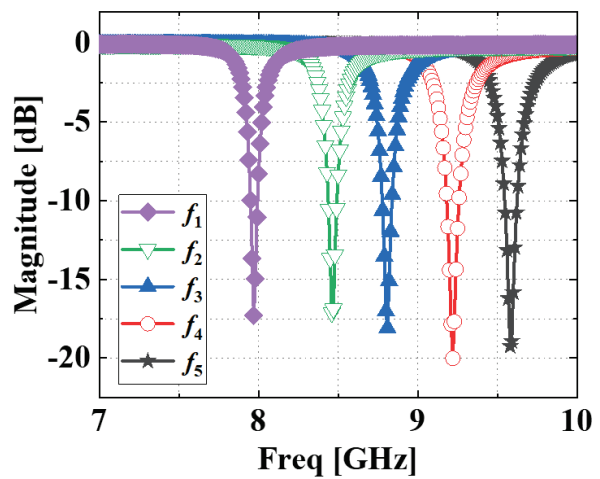
Fig. 4. Response curve of the five-state single resonator structure (N=1, M=4).

When N=3 and M=4, there are 15 resonance frequencies. The schematic diagrams of the structure are shown in Fig. 5. Where f_{NM} is the resonance frequency of the N-th resonator, the number of the embedding OES is M. The resonance curves of simulation for the structure diagram of Fig. 5 with the parameter values of Table 1 are shown in Fig. 6. The intervals between the resonance frequencies corresponding to the spectral signature are within 250-490 MHz. The spectral signatures do not interfere with each other and the notch depth is between -11 dB to -18 dB. There is a weak interference with a notch depth of -3 dB at 9.91 GHz; however, for the resonance frequency f_{15}=9.72 GHz, the notch depth reaches -17 dB, the interference will not affect the encoding state. The set of 15 resonance frequencies in Fig. 6 is shown in Table 3, wherein the maximum and minimum intervals are 490 MHz and 250 MHz between adjacent resonance frequencies.
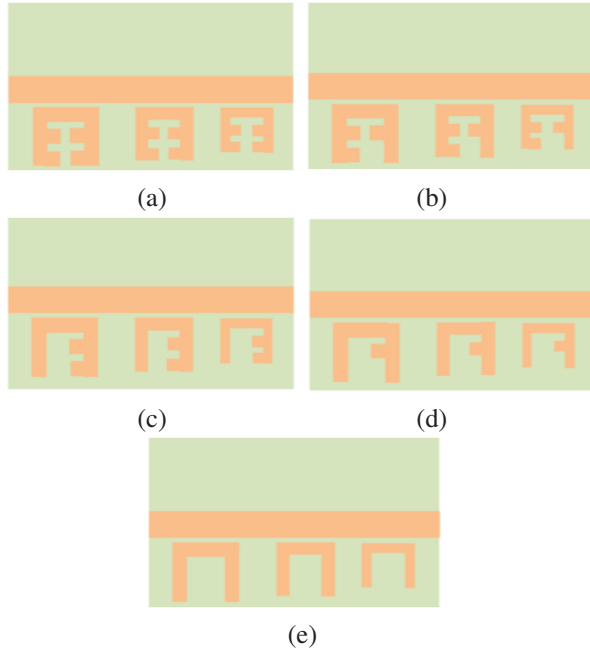
Fig. 5. Schematic diagram of the structure (N=3, M=4): (a) $f_{31}f_{21}f_{11}$; (b) $f_{32}f_{22}f_{12}$; (c) $f_{33}f_{23}f_{13}$; (d) $f_{34}f_{24}f_{14}$; (e) $f_{35}f_{25}f_{15}$.
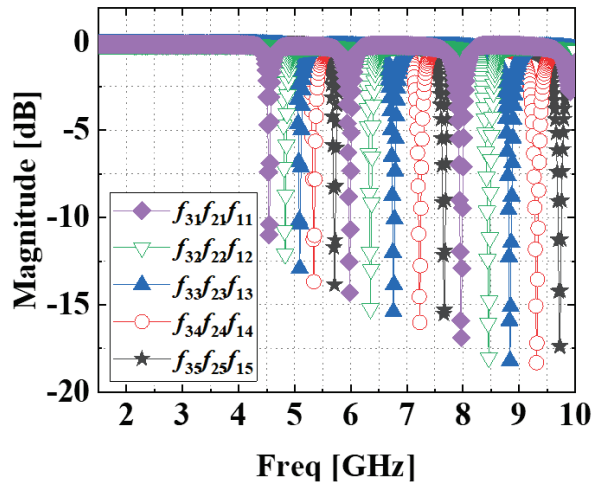
Fig. 6. Resonance curves of the multi-state resonators (N=3, M=4).

Table 3: All resonance frequencies of the three multi-state resonators (unit: GHz)

f_{11}	f_{12}	f_{13}	f_{14}	f_{15}
7.97	8.46	8.84	9.31	9.72
f_{21}	f_{22}	f_{23}	f_{24}	f_{25}
5.98	6.35	6.76	7.23	7.66
f_{31}	f_{32}	f_{33}	f_{34}	f_{35}
4.54	4.83	5.09	5.34	5.71

In order to improve the encoding capacity without increasing the dimension of the tag, using the sharing frequency method, a pair of the same size resonators is placed symmetrically on both sides of the coupled microstrip transmission line. The schematic diagram of the structure is shown in Fig. 7. When N=2, M=4, where N is a pair of the same size resonators, it can provide 15 different resonance frequencies. If a pair of the same size resonators is the resonator as shown in Fig. 5, it can be generated thus:

$$
\begin{bmatrix}
f_1 f_1 & f_1 f_2 & f_1 f_3 & f_1 f_4 & f_1 f_5 \\
f_2 f_1 & f_2 f_2 & f_2 f_3 & f_2 f_4 & f_2 f_5 \\
f_3 f_1 & f_3 f_2 & f_3 f_3 & f_3 f_4 & f_3 f_5 \\
f_4 f_1 & f_4 f_2 & f_4 f_3 & f_4 f_4 & f_4 f_5 \\
f_5 f_1 & f_5 f_2 & f_5 f_3 & f_5 f_4 & f_5 f_5
\end{bmatrix}. \tag{6}
$$

On the frequency axis, $f_1 f_1$, $f_2 f_2$, $f_3 f_3$, $f_4 f_4$ and $f_5 f_5$ are all shown as curves with one resonance notch, and other data are shown as curves with two different resonance notches. However, in the above matrix (6), the data of the upper triangle and the lower triangle are repeated, which will cause data confusion in the tag identification of the item (for example, $f_1 f_2$ and $f_2 f_1$ have the same coding state on the spectrum). Therefore, the frequency combinations of the red or blue triangle box can be encoded. The total of 15 different resonance frequencies can be generated by using the sharing frequency method. For three pairs of resonators, there will be 15^3 codes, which is about 2^{12}. The combination method in mathematics can be used to calculate the number of different resonance frequencies.
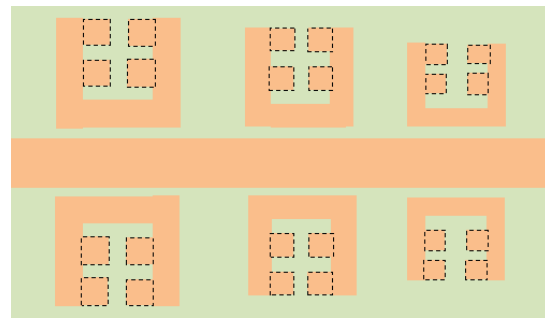
Fig. 7. Schematic diagram of resonators of the same size in pairs (N=6).

Figures 8 (a), (b), (c) and (d) are the resonance curves of tag coding $f_{31}f_{35}f_{21}f_{25}f_{11}f_{15}$, $f_{33}f_{35}f_{23}f_{24}f_{12}f_{14}$, $f_{32}f_{34}f_{22}f_{24}f_{12}f_{13}$ and $f_{32}f_{33}$ $f_{22}f_{23}f_{13}f_{15}$ based on the sharing frequency multi-state resonators. Table 4 shows the combinations of the resonance frequency encoding states of the four

Fig. 8. Resonance curves of four sharing frequency multi-state resonator tags: (a) $f_{31}f_{35}f_{21}f_{25}f_{11}f_{15}$; (b) $f_{33}f_{35}f_{23}f_{24}f_{12}f_{14}$; (c) $f_{32}f_{34}f_{22}f_{24}f_{12}f_{13}$; (d) $f_{32}f_{33}f_{22}f_{23}f_{13}f_{15}$.

Table 4: Resonance frequency of four sharing frequency multi-state resonator tags (unit: GHz)

$f_{31}f_{35}f_{21}f_{25}f_{11}f_{15}$	f_{31}	f_{35}	f_{21}	f_{25}	f_{11}	f_{15}
Frequency Shift Compared With Table 3	4.52	5.76	5.93	7.72	7.97	9.68
	0.02	0.05	0.06	0.06	0	0.04
$f_{33}f_{35}f_{23}f_{24}f_{12}f_{14}$	f_{33}	f_{35}	f_{23}	f_{24}	f_{12}	f_{14}
Frequency Shift Compared With Table 3	5.08	5.73	6.76	7.28	8.47	9.37
	0.01	0.02	0	0.05	0.01	0.06
$f_{32}f_{34}f_{22}f_{24}f_{12}f_{13}$	f_{32}	f_{34}	f_{22}	f_{24}	f_{12}	f_{13}
Frequency Shift Compared With Table 3	4.80	5.45	6.39	7.30	8.46	8.85
	0.03	0.11	0.04	0.07	0	0.01
$f_{32}f_{33}f_{22}f_{23}f_{13}f_{15}$	f_{32}	f_{33}	f_{22}	f_{23}	f_{13}	f_{15}
Frequency Shift Compared With Table 3	4.86	5.16	6.28	6.73	8.82	9.69
	0.03	0.07	0.07	0.03	0.02	0.03

tags. Comparing the simulation results in Table 4 and Table 3, the maximum frequency offset is f_{34} in tag $f_{32}f_{34}f_{22}f_{24}f_{12}f_{13}$, which is 110 MHz. The maximum frequency offset does not exceed the minimum frequency interval of 250 MHz in Table 3, which will not cause error code.

IV. EXPERIMENT RESULTS

In accordance with the simulation results, several chipless tags with sharing frequency multi-state resonators are fabricated, named $f_{31}f_{35}f_{21}f_{25}f_{11}f_{15}$, $f_{33}f_{35}f_{23}f_{24}f_{12}f_{14}$, $f_{32}f_{34}f_{22}f_{24}f_{12}f_{13}$ and $f_{32}f_{33}f_{22}f_{23}f_{13}f_{15}$. Figure 9 is the photograph of the chipless tags with sharing frequency multi-state resonators. It can be seen that the tag is small in size, compared to the dime coin as a reference.

(a)   (b)

(c)   (d)
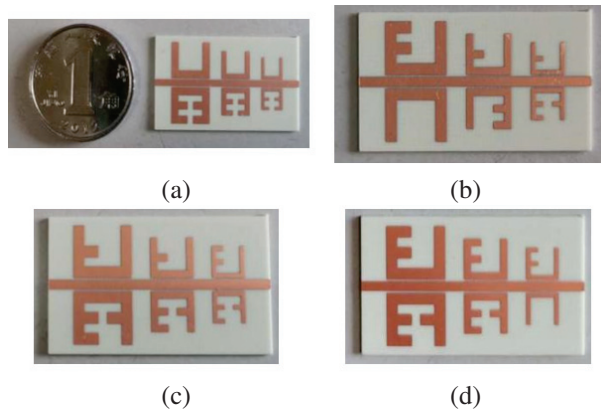
Fig. 9. Photograph of chipless tags with sharing frequency multi-state resonators: (a) $f_{31}f_{35}f_{21}f_{25}f_{11}f_{15}$; (b) $f_{33}f_{35}f_{23}f_{24}f_{12}f_{14}$; (c) $f_{32}f_{34}f_{22}f_{24}f_{12}f_{13}$; (d) $f_{32}f_{33}f_{22}f_{23}f_{13}f_{15}$.

Fig. 10. Test system.

Fig. 11. The AR curve of the UWB disc monopole antenna.

Figure 10 is the test system of a retransmitted chipless tag based on multi-state resonators. Ceyear vector network analyzer 3672D is used as an alternative to the UWB reader. The two ports of the network analyzer are connected to the two UWB disc monopole antennas, which are orthogonal to each other to improve the transceiver isolation of the reader. The chipless tag is also connected to two orthogonal UWB disc monopole antennas through two microwave connectors. In order to prevent the received signal and the transmitted signal of the tag from interfering with each other, the two-sided UWB antennas of the tag are also orthogonal to each other. The reader antennas and the tag antennas are fixed on the foam, and the distance between them is 30 cm.

The UWB disc monopole antenna is designed on RO4350 substrate with the structure of the literature [27], with the relative dielectric constant 3.66, the loss tangent 0.004, and the thickness of the substrate 1 mm. The axial ratio (AR) curve of the disc monopole antenna with a radius of 10 cm is shown in Fig. 11. The AR is much greater than 3 dB within the UWB frequency band, so the UWB disc monopole antenna has linearly polarized radiation. The polarization characteristics of the transmitting antenna of the reader and the receiving antenna of the tag are the same, but as they are orthogonal to the polarization characteristics of the transmitting antenna of the tag, polarization isolation will be formed. The transmitting antenna of the reader will not receive any signal from the tag. However, the receiving antenna of the reader can receive the signal from the tag. Similarly, the polarization characteristics of the receiving antenna of the reader and its transmitting antenna are orthogonal, so they will not affect each other. Just like the transceiver antennas of the reader are orthogonal to each other, the tag's transceiver antennas are also orthogonal to each other. The configuration structure of the transceiver antenna of the reader and the tag's transceiver antenna is shown in Fig. 10.
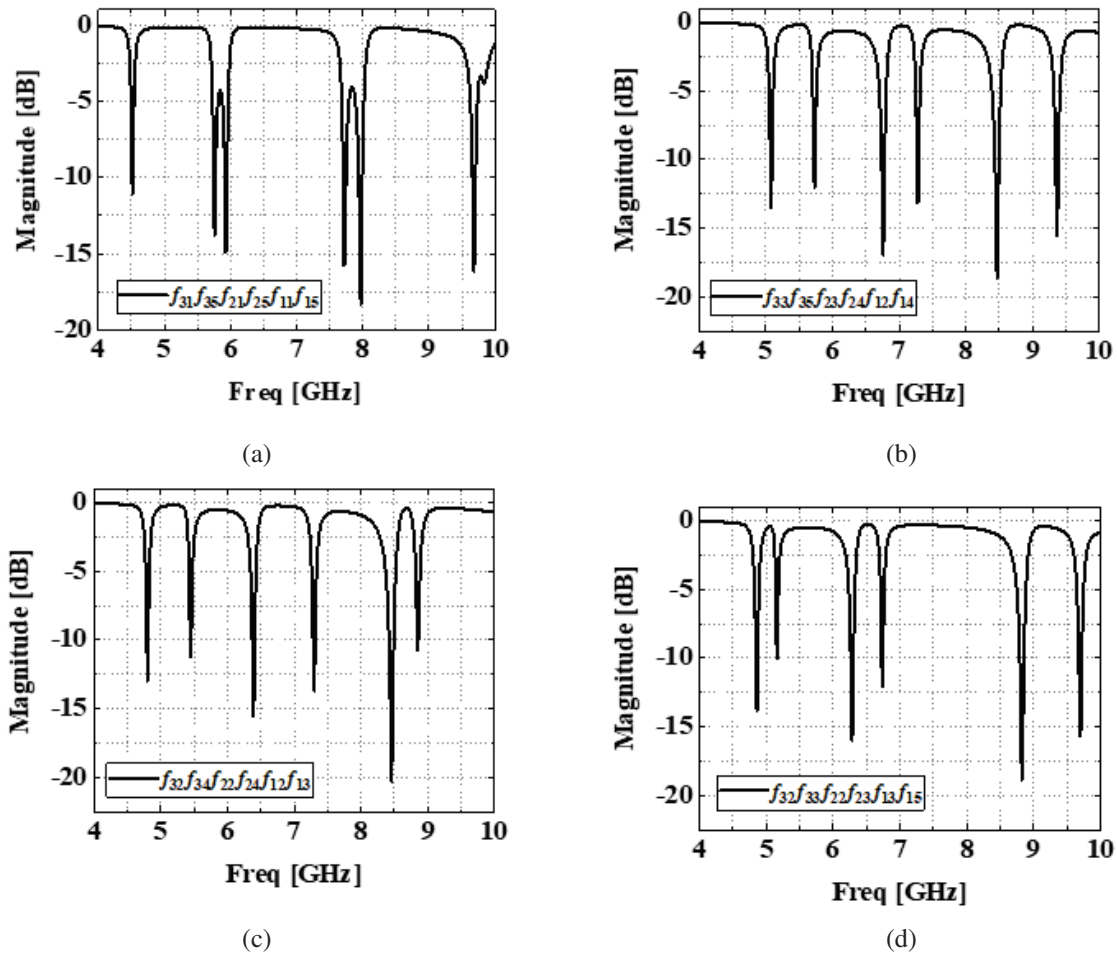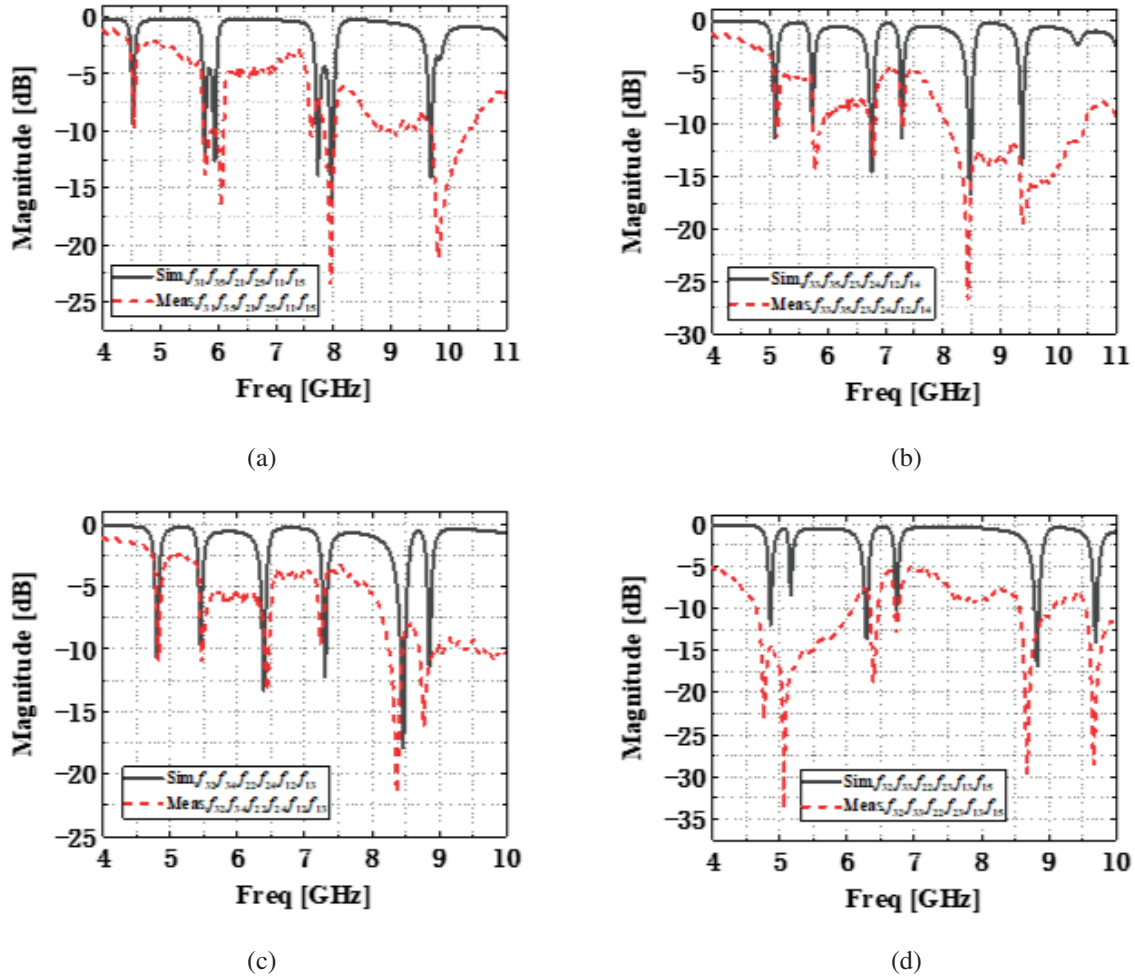
Fig. 12. Simulation and measurement of resonance curves of four sharing frequency multi-state resonators tags: (a) $f_{31}f_{35}f_{21}f_{25}f_{11}f_{15}$; (b) $f_{33}f_{35}f_{23}f_{24}f_{12}f_{14}$; (c) $f_{32}f_{34}f_{22}f_{24}f_{12}f_{13}$; (d) $f_{32}f_{33}f_{22}f_{23}f_{13}f_{15}$.

The UWB disc monopole antennas have the characteristics of omnidirectional radiation. In practical applications, the surrounding environment will definitely affect the chipless tag system. At this time, a UWB linearly polarized directional antenna is needed to reduce the impact of environmental factors on the tag system.

Figures 12 (a), (b), (c) and (d) show the characteristic results of simulation and measurement to the sharing frequency encoded tags. It can be seen from Fig. 12 that the simulation is consistent with the actual measurement. The maximum deviation of the resonance frequency points between the simulation and the measurement is 140 MHz, which is lower than the guard band of single resonance frequencies. The different amplitude between the simulation and measurement of each tag is mainly affected by the two antennas matching the tag and the performance of the UWB antenna. It will not affect the tag's encoding state. The spectral signatures can correctly reflect the tag's encoding data.

V. DISCUSSION

The mutual coupling between the resonance units can be reduced by increasing the spacing between the adjacent resonators. However, the resonance frequency shift may be generated. Figure 13 shows the resonance curve when the resonator spacing d_2 is changed in Fig. 5 (a). When d_2 increases from 1.5 mm to 4.6 mm, the resonator in the middle is affected by the resonators on both sides, and the resonance frequency is slightly shifted. The resonators on both sides are less affected, and the resonance frequency points are almost unchanged. The mutual coupling effect between the resonators can be reduced by adjusting the resonator spacing d_2.

Figures 14 and 15 are the simulated resonance curves of Structure 1 in Table 2 when the width w_2 and length g of the OES are changed, respectively. As w_2 becomes wider and g becomes longer, the resonance frequency becomes smaller, while the bandwidth occupied by the resonator is almost unchanged. As w_2
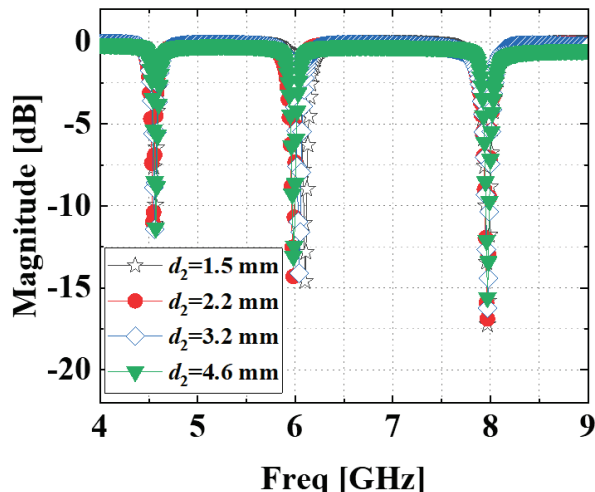
Fig. 13. Resonance curves of the resonator when spacing d_2 is changed from 1.0 mm to 4.6 mm.

Fig. 14. Resonance curves of the structure 1 when w_2 is changed from 0.3 mm to 1.0 mm.

becomes wider, the notch depth of the resonance frequency becomes shallower.

For a tag of N=3 and M=10, a single resonator has 11 different resonance frequencies, and 3 resonators of different sizes have a total of 33 different resonance frequencies. In order that adjacent resonance frequencies do not affect each other, the structural parameters w_2, g and t are adjusted to 0.2 mm, 0.6 mm and 0.4 mm, respectively through simulation. According to the simulation results, the three resonators' working bandwidths are shown as f_{11}-f_{15}, f_{21}-f_{25}, and f_{31}-f_{35} in Table 4. As long as the resonator structures of Figs. 5 (a) and 5 (e) are simulated, the operating bandwidths of the tags can be determined, and the simulation results are shown in

Fig. 15. Resonance curves of the structure 1 when g is changed from 0.5 mm to 1.5 mm.

Fig. 16. Where f'_{NM} is the resonance frequency of the N-th resonator, the number of the embedding OES is M. The operating bandwidths of the three resonators f'_{11}-f'_{111}, f'_{21}-f'_{211}, and f'_{31}-f'_{311} of M=10 are 4.14-5.18, 5.74-8.18 and 8.96-11.46 GHz, respectively. The notch depth is between -5.8 and -15.23 dB. However, the second harmonic of f'_{311} appears at 10.14 GHz in Fig. 16. The notch depth of the 2nd harmonic is -3.65 dB. This interference of the 2nd harmonic on the spectrum signature can be removed by signal processing and certain algorithms. For N=3 and M=10, the total of 33 resonant frequency signatures can generate 11^3 codes, which is about 2^{10}. When the number of resonators is six, the encoding state of the chipless tag based on the
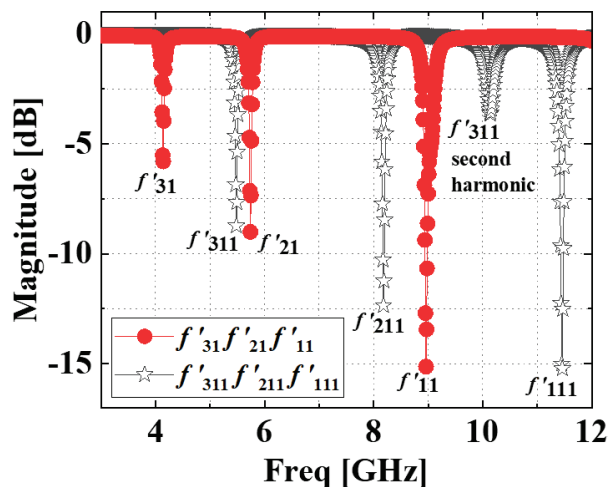
Fig. 16. Operating bandwidth of sharing frequency multi-state resonator tags where N=3, M=10.

Table 5: Comparison of different types of retransmitted chipless tags

Resonator Type	Operating Frequency Band (GHz)	Capacity (bits/cm^2)	Encoding Capacity (bits/cm^2/GHz)	Tag Area (mm^2)	Substrate
Spiral [3]	3-7	0.61	0.15	88×65	Taconic TLX-0
Spiral [19]	5-11	0.33	0.06	108×64	Taconic TF-290
Open Stubs [20]	4-9	0.24	0.05	110×60	Rogers 4003C
Open Loop [22]	3-6	0.25	0.08	85×38	Rogers 5880
Purline Resonators [23]	2.4-4.2	0.09	0.05	150×60	C-MET/LK4.3
Cascades E-shaped [24]	3.3-4.3	0.05	0.05	160×100	C-MET/LK4.3
Multi-state Resonators (N=6, M=4) (Proposed)	4.8-9.7	0.87	0.18	46×30	Rogers 4350

sharing frequency multi-state resonators is 66^3, which is about 2^{18}.

Table 5 shows the comparisons among different retransmitted chipless tags, including the aspects of bandwidth (GHz), capacity (bits/cm^2), encoding capacity (bits/cm^2/GHz), tag area (mm^2) and substrate. It can be seen that the proposed chipless tags show the most promising properties as the retransmitted chipless tag among all the listed results. Although the spiral resonator chipless tag has high capacity, this tag is limited by its large area. The open loop resonator has low encoding capacity of 0.08 bits/cm^2/GHz and a large area compared with this work. The open stubs, purline and cascades E-shaped resonators also have large tag areas and low encoding capacity. In summary, the retransmitted chipless tag of the OES multi-state resonator that we propose in this paper has a small area and large encoding capacity.

VI. CONCLUSION

This paper proposes a chipless tag for sharing frequency multi-state resonators based on the retransmission structure. This work demonstrates a frequency sharing method based on the retransmitted chipless tag. U-shaped microstrip resonators are used to embed some OES lines to implement the frequency sharing, which achieves the purpose of saving spectrum and improving spectrum utilization. The number of different resonance frequencies of the sharing frequency can be calculated using a combination in mathematics. The sharing frequency method aims to realize small size tags with a large encoding capacity. This chipless tag includes U-shaped microstrip resonators, the OES line and a 50 Ω microstrip transmission line. The sharing frequency multi-state resonator chipless tag was fabricated on RO4350 substrate. The operating frequency band of 4.8-9.7 GHz is designed where N=6, M=4, a pair of the same size resonators is placed symmetrically on both sides of the coupled microstrip transmission line. This chipless tag with an area of 46×30 mm^2 can generate about 2^{12} encoding states. The capacity is 0.87 bits/cm^2. The encoding capacity is 0.18 bits/cm^2/GHz. The communication distance is 30 cm. Each resonator has only two states in the traditional retransmitted chipless tag. Six resonators can only realize 2^6 encoding states, whose encoding capacity is less than the multi-state resonators.

Using HFSS software, simulation shows that the intervals between the resonance frequencies corresponding to the spectral signature are within 250-490 MHz, and the spectral signatures do not interfere with each other. The simulation and measurement are in good agreement. This paper increases the number of embedded OES in the U-shaped microstrip resonator to increase the coding capacity. The sharing frequency method is used to improve the spectrum utilization rate. In the future, it is proposed to further increase the coding capacity and solve the key problem of anti-collision of the chipless tag. The cost of this chipless tag is low which means it can be widely used in logistics, supermarkets and other fields to replace the barcode.

REFERENCES

[1] U. Kaiser and W. Steinhagen, "A low-power transponder IC for high−performance identification systems," *IEEE Journal of Solid-State Circuits*, vol. 30, no. 3, pp. 306-310, Mar. 1995.

[2] S. Preradovic and N. C. Karmakar, "Chipless RFID: bar code of the future," *IEEE Microwave Magazine*, vol. 11, no. 7, pp. 87-97, Dec. 2010.

[3] S. Preradovic, I. Balbin, N. C. Karmakar, and G. F. Swiegers, "Multiresonator-based chipless RFID system for low-cost item tracking," *IEEE Transactions on Microwave Theory and Techniques*, vol. 57, no. 5, pp. 1411-1419, May 2009.

[4] C. Herrojo, J. Mata-Contreras, F. Paredes, A. Núñez, E. Ramon, and F. Martín, "Near-field chipless-RFID system with erasable/programmable 40-bit tags inkjet printed on paper substrates," *IEEE Microwave and Wireless Components Letters*, vol. 28, no. 3, pp. 272-274, Mar. 2018.

[5] A. Ali, S. I. Jafri, A. Habib, Y. Amin, and H. Tenhunen, "RFID humidity sensor tag for low-cost applications," *Applied Computational Electromagnetics Society (ACES) Journal*, vol. 32, no. 12, pp. 1083-1088, May 2017.

[6] A. Chamarti and K. Varahramyan, "Transmission delay line based ID generation circuit for RFID applications," *IEEE Microwave and Wireless Components Letters*, vol. 16, no. 11, pp. 588-590, Nov. 2006.

[7] A. Stelzer, S. Scheiblhofer, S. Schuster, and M. Brandl, "Multi reader/Multi-tag SAW RFID systems combining tagging, sensing, and ranging for industrial applications," *IEEE International Frequency Control Symposium*, Honolulu, HI, USA, pp. 263-272, May 2008.

[8] B. Shao, Q. Chen, Y. Amin, S. M. David, R. Liu, and L. Zheng, "An ultra-low-cost RFID tag with 1.67 Gbps data rate by ink-jet printing on paper substrate," *IEEE Asian Solid-State Circuits Conference*, Beijing, China, pp. 1-4, Nov. 2010.

[9] C. S. Hartmann, "A global SAW ID tag with large data capacity," *IEEE Ultrasonics Symposium*, Munich, Germany, vol. 1, pp. 65-69, Oct. 2002.

[10] J. Liu and J. Yao, "Wireless RF identification system based on SAW," *IEEE Transactions on Industrial Electronics*, vol. 55, no. 2, pp. 958-961, Feb. 2008.

[11] S. Haermae, V. P. Plessky, C. S. Hartmann, and W. Steichen, "Z-path SAW RFID tag," *IEEE Transactions on Ultrasonics Ferroelectrics and Frequency Control*, vol. 55, no. 1, pp. 208-213, Jan. 2008.

[12] V. P. Plessky and L. M. Reindl, "Review on SAW RFID tags," *IEEE Transactions on Ultrasonics Ferroelectrics and Frequency Control*, vol. 57, no. 3, pp. 654-668, Mar. 2010.

[13] M. Polivka, J. Havlicek, M. Svanda, and J. Machac, "Improvement in robustness and recognizability of RCS response of U-shaped strip-based chipless RFID tags," *IEEE Antennas and Wireless Propagation Letters*, vol. 15, pp. 2000-2003, Apr. 2016.

[14] M. Svanda, M. Polivka, J. Havlicek, and J. Machac, "Chipless RFID tag with an improved magnitude and robustness of RCS response," *Microwave and Optical Technology Letters*, vol. 59, no. 2, pp. 488-492, Feb. 2017.

[15] M. Svanda, J. Havlicek, J. Machac, and J. Polivka, "Polarisation independent chipless RFID tag based on circular arrangement of dual-spiral capacitively-loaded dipoles with robust RCS response," *IET Microwaves Antennas and Propagation*, vol. 12, no. 14, pp. 2167-2171, Nov. 2018.

[16] N. Chen, Y. Shen, G. Dong, and S. Hu, "Compact scalable modeling of chipless RFID tag based on high-impedance surface," *IEEE Transactions on Electron Devices*, vol. 66, no. 1, pp. 200-206, Jan. 2019.

[17] G. Q. Dong, Y. Z. Shen, H. F. Meng, N. Chen, and W. B. Dou. "Printable chipless tag and dual-CP reader for internet of things," *Applied Computational Electromagnetics Society (ACES) Journal*, vol. 33, no. 5, pp. 494-498, May 2018.

[18] S. Preradovic and N. C. Karmakar, "Design of fully printable planar chipless RFID transponder with 35-bit data capacity," *European Microwave Conference (EuMC)*, Rome, Italy, pp. 13-16, 2009.

[19] S. Preradovic, S. Roy and N. Karmakar, "Fully printable multi-bit chipless RFID transponder on flexible laminate," *Asia Pacific Microwave Conference*, Singapore, pp. 2371-2374, Sep. 2009.

[20] M. A. Ashraf, Y. A. Alshoudokhi, H. M. Behairy, M. R. Alshareef, S. A. Alshebeilim, K. Issa, and H. Fathallah, "Design and analysis of multi-resonators loaded broadband antipodal tapered slot antenna for chipless RFID applications," *IEEE Access*, vol. 5, pp. 25798-25807, Oct. 2017.

[21] Y. F. Weng, S. W. Cheung, T. I. Yuk, and L. Liu, "Design of chipless UWB RFID system using a CPW multi-resonator," *IEEE Antennas and Propagation Magazine*, vol. 55, no. 1, pp. 13-31, Feb. 2013.

[22] V. Sharma and M. Hashmi, "Chipless RFID tag based on open-loop resonator," *IEEE Asia Pacific Microwave Conference (APMC)*, Kuala Lumpur, Malaysia, pp. 543-546, Nov. 2017.

[23] M. Sumi, C. M. Nijas, R. Dinesh, S. Mridula, and P. Mohanan, "Spectral signature-encoded chipless RFID tag with planar multiresonators," *Journal of Electromagnetic Waves and Applications*, vol. 28, no. 18, pp. 2266-2275, Dec. 2014.

[24] M. Sumi, R. Dinesh, C. M. Nijas, S. Mridula, and P. Mohanan, "High bit encoding chipless RFID tag using multiple E shaped microstrip resonators,"

Progress in Electromagnetics Research B, vol. 61, no. 2014, pp. 185-196, Nov. 2014.

[25] E. O. Hammerstad and O. Jensen, "Accurate models for microstrip computer-aided design," *International Microwave Symposium Digest IEEE*, pp. 407-409, May 1980.

[26] E. Q. Hammerstard, "Equations for microstrip circuit design." *IEEE European Microwave Conference*, Hamburg, Germany, pp. 268-272, Sept. 1975.

[27] J. X. Liang, C. C. Chiau, X. D. Chen, and C. G. Parini, "Study of a printed circular disc monopole antenna for UWB systems," *IEEE Transactions on Antennas and Propagation*, vol. 53, no. 11, pp. 3500-3504, Nov. 2005.

Ma Zhonghua was born in Gansu, Republic of China, in 1973. He received his M.S. degree in Information Engineering and Communication and Information Systems in 2004 and his Ph.D degree in Microelectronics in 2018, both from Lanzhou University. His present research interests include antenna techniques, RF circuit design and RFID systems. His current research concerns the field of chipless RFID sensors.

Huang Nengyu received her bachelor's degree from the University of South China in 2019. She is currently working on her M.S. degree in Traffic and Transportation Engineering at Jimei University, Fujian Province, China. Her research interest is radio frequency identification (RFID).

Shaping the Probability Density Function of the Output Response in a Reverberation Chamber

Qian Xu[1], Feng Tian[1], Yongjiu Zhao[1], Rui Jia[2], Erwei Cheng[3], and Lei Xing[1]

[1]College of Electronic and Information Engineering
Nanjing University of Aeronautics and Astronautics, Nanjing 211106, China
emxu@foxmail.com, yjzhao@nuaa.edu.cn, emxinglei@foxmail.com

[2]State Key Laboratory of Complex Electromagnetic Environment Effects on Electronic and Information System
Luo Yang 471003, China
jiarui315@163.com

[3]Department of Engineering Physics, Tsinghua University, Beijing
China and National Key Laboratory on Electromagnetic Environment Effects
Army Engineering University Shijiazhuang Campus, Shijiazhuang 050004, China
ew_cheng@163.com

Abstract – This paper shows that the received power and E-field in a reverberation chamber (RC) can be shaped by tuning the statistical properties of input signals. For a given probability density function (PDF) of an RC response, the Fourier transform method can be applied to find the PDF of the input signal. Numerical and measurement verifications are given to validate the theory. Limitations are also analyzed and discussed.

Index Terms – probability density function, reverberation chamber.

I. INTRODUCTION

A reverberation chamber (RC) is a highly resonant electrically large cavity which is equipped with mechanical stirrers inside (Fig. 1 (a)). The stirrers are used to tune the boundary conditions inside the cavity to generate statistically isotropic and uniform electromagnetic fields. In recent years, RCs have been widely used in electromagnetic compatibility (EMC) and over-the-air (OTA) testing [1, 2]. Unlike an anechoic chamber which is designed as a deterministic system, an RC was born to be a statistical environment. It has been found that for a well-stirred RC, the received power has an exponential distribution and the magnitude of the rectangular E-field component ($|E_x|$, $|E_y|$ or $|E_z|$) has a Rayleigh distribution [3]. In vehicles, ships and planes, when more cavities are cascaded or nested, the E-field magnitude may no longer be Rayleigh distribution.

Due to the inherent statistical properties of an RC, a Rayleigh distribution (or a Rician distribution) can be well emulated, and the K-factors can be tuned statistically
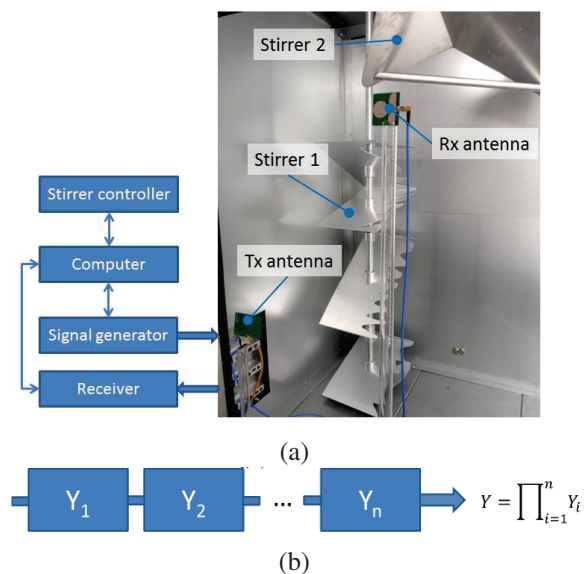
Fig. 1. (a) Typical measurement setup in an RC; the inner dimensions are 0.94 m $\times$ 1.16 m $\times$ 1.44 m. (b) Multi-cavity coupling model.

[4–8]. By combining an RC with a channel emulator, a complex channel response can be emulated [9–11].

However, it does not seem easy to emulate response with arbitrary statistical distributions. If more distribution functions are expected in the channel emulation, refined controls are necessary. This paper proposes a method to control the PDF of RC responses in the frequency domain (FD), which can be used for the emulation of multi-cavity statistics in a single RC instead of actually using multiple connected cavities.

In this paper, Section II presents the theory, Section III starts from a simplified scenario and demonstrates the product of two random variables analytically and experimentally. Limitations and generalizations to multi-cavity models are discussed in Section IV.

II. THEORY

In the FD, when an RC is well-stirred and the magnitude of the input signal is a constant, the magnitude of rectangular E-field ($|E_x|$) inside the RC has a Rayleigh distribution [3]:

$$p_Y(y) = ye^{-\frac{y^2}{2\sigma_y^2}}/\sigma_y^2, \quad y = |E_x|, \tag{1}$$

of which the expected value and the standard deviation are $\sigma_y\sqrt{\pi/2}$ and $\sigma_y\sqrt{2-\pi/2}$, respectively. When the statistical property of the input signal can be controlled, the PDF of the RC response (E_{out}) can be tuned. Generally, the product of two random variables $Z = X \times Y$ can be used to synthesize the output response of a system, where X, Y and Z are the input variable, transfer function and output variable, respectively. Thus, the problem can be mathematically described as: for the given PDFs of random variable Z and Y, and $Z = X \times Y$, what is the PDF of random variable X?

A misleading procedure is to use $X = Z/Y$ to calculate the PDF of X, which is wrong. The result will depend on specific set of Z and Y. This procedure can be understood from the Mellin transform: when using $X' = Z/Y$, the Mellin transform of the PDF of random variable X' can be obtained as $M_Z(s)M_Y(2-s) = M_X(s)M_Y(s)M_Y(2-s)$ which is not equal to $M_X(s)$ (only when $M_Y(s)M_Y(2-s) = 1$) [12]. To find the PDF of X, a direct method is to use the Mellin and inverse Mellin transform, the result can be obtained quickly as $\mathscr{M}^{-1}[M_Z(s)/M_Y(s)]$. However, the numerical Mellin and inverse Mellin transform are not easy to calculate. In this paper, we adopt an approach with Fourier transforms.

From $Z = X \times Y$, we have $\ln Z = \ln X + \ln Y$ when X and Y are positive. Suppose the PDF of $\ln Z$, $\ln X$ and $\ln Y$ are $p_{\ln Z}(z)$, $p_{\ln X}(x)$ and $p_{\ln Y}(y)$, respectively. We have

$$H_{\ln Z}(j\omega) = H_{\ln X}(j\omega)H_{\ln Y}(j\omega), \tag{2}$$

where $H_{\ln Z}(j\omega)$, $H_{\ln X}(j\omega)$ and $H_{\ln Y}(j\omega)$ are the Fourier transforms of $p_{\ln Z}(z)$, $p_{\ln X}(x)$ and $p_{\ln Y}(y)$, respectively. (e.g., $H_{\ln X}(j\omega) = \int_{-\infty}^{+\infty} p_{\ln X}(x)e^{-j\omega x}dx$). Thus, the PDF of the input signal $p_{\ln X}(x)$ can be calculated by using the inverse Fourier transform

$$p_{\ln X}(x) = \mathscr{F}^{-1}[H_{\ln Z}(j\omega)/H_{\ln Y}(j\omega)]. \tag{3}$$

Finally, by applying the variable transform e^X to $\ln X$, the PDF of X (in linear unit) can be obtained.

III. DERIVATIONS AND VERIFICATIONS

When two RCs are nested or contiguous [13], a double-Rayleigh PDF response can be obtained. Suppose we want to emulate a double-Rayleigh PDF response in a single RC. We can control the magnitude of the input signal to have a random excitation. Assume the magnitude of the input signal has a PDF of

$$p_X(x) = xe^{-\frac{x^2}{2\sigma_x^2}}/\sigma_x^2, \quad x = |E_{in}|, \tag{4}$$

and the RC has a transfer function (Y) given in (1), the PDF of the response has been obtained in [13] as

$$p_Z(z) = \frac{z}{\sigma_x^2\sigma_y^2}K_0\left(\frac{z}{\sigma_x\sigma_y}\right), \quad z = |E_{out}|, \tag{5}$$

where $K_0(.)$ is the zero-order modified Bessel function of the second kind, and the expected value and the standard deviation of (5) are $\sigma_x\sigma_y\pi/2$ and $\sigma_x\sigma_y\sqrt{4-\pi^2/4}$, respectively. $|E_{in}|$ and $|E_{out}|$ represent the magnitude of the input signal (E-field) and the output signal (E-field), respectively. From (4), the PDF of $\ln X$ can be obtained as

$$p_{\ln X}(x) = e^{2x}e^{-\frac{e^{2x}}{2\sigma_x^2}}/\sigma_x^2, \quad x = \ln|E_{in}|, \tag{6}$$

of which the mean and the standard deviation are $\ln 2/2 + \ln\sigma_x - \gamma/2$ and $\pi\sqrt{6}/12$, respectively ($\gamma \approx 0.5772$ is the Euler-Mascheroni constant). The Fourier transform of (6) is

$$H_{\ln X}(j\omega) = \left(\sqrt{2}\sigma_x\right)^{-j\omega}\Gamma(1-j\omega/2). \tag{7}$$

The Fourier transform of $p_{\ln Y}(y)$ is the same as (7) but σ_x is replaced by σ_y. It can be verified that the Fourier transform of

$$p_{\ln Z}(z) = \frac{e^{2z}}{\sigma_x^2\sigma_y^2}K_0\left(\frac{e^z}{\sigma_x\sigma_y}\right), \quad z = \ln|E_{out}|, \tag{8}$$

is

$$H_{\ln Z}(j\omega) = \left(2\sigma_x\sigma_y\right)^{-j\omega}\Gamma^2(1-j\omega/2). \tag{9}$$

To verify this procedure numerically, Monte-Carlo simulations are performed with parameters $\sigma_x = 1$ and $\sigma_y = 4$. We solve the PDF of X from Z and Y using the numerical method and compare the results with analytical expressions. 10^6 samples of X and Y are generated with Rayleigh distributions. The output

variable $Z = X \times Y$ can be obtained. The histograms of $\ln Z$ and $\ln Y$ are illustrated in Fig. 2 (a) with analytical expressions. The corresponding Fourier transforms are presented in Fig. 2 (b), in which the numerical Fourier transforms are calculated from the histograms. Finally, the PDF of $\ln X$ is inverted numerically using (3) and compared with original histogram and analytical expression in Fig. 2 (c). It can be observed that the numerical results agree well with analytical solutions with acceptable small differences. These differences are caused by the finite samples used in Monte-Carlo simulations and the truncation errors in the Fourier and inverse Fourier transform.
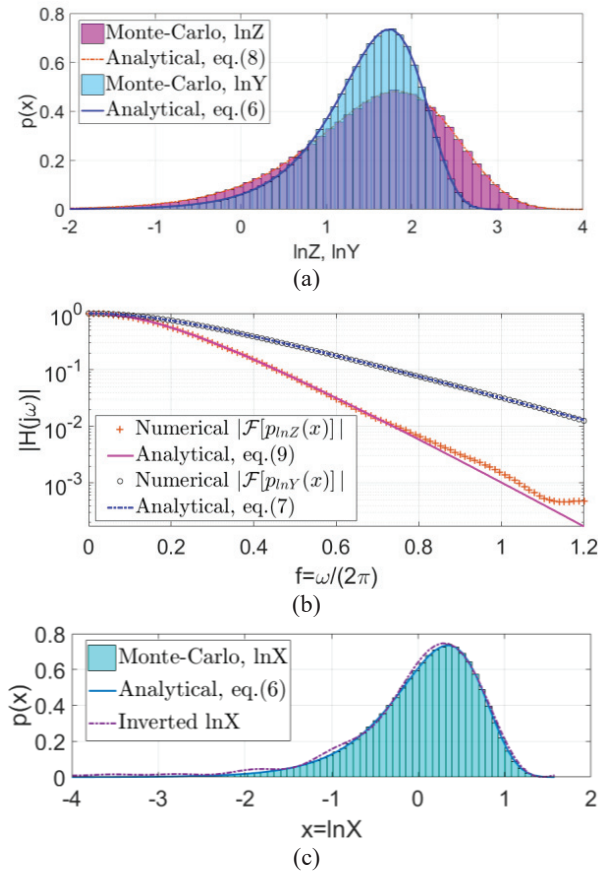
Fig. 2. (a) The PDF plots of $\ln Z$ and $\ln Y$, (b) the magnitude of the Fourier transforms, and (c) the inverted PDF of $\ln X$ and analytical expression.

Instead of using the magnitude of the E-field, the derivations can also be verified using the received power. Suppose

$$p_{X^2}(x) = e^{-\frac{x}{u_x}} / u_x, \quad x = P_x, \quad (10)$$

where the expected value and the standard deviations are both u_x $(u_x = 2\sigma_x^2)$. The power transfer function Y^2 has

a PDF similar with (10). The PDF of the output power $Z^2 = X^2 \times Y^2$ can be obtained as

$$p_{Z^2}(z) = \frac{2}{u_x u_y} K_0 \left(2\sqrt{\frac{z}{u_x u_y}} \right), \quad z = P_{\text{out}}, \quad (11)$$

where $u_y = 2\sigma_y^2$ is the expected value of $p_{Y^2}(y)$. The expected value and the standard deviation of (11) can be derived as $u_x u_y$ and $u_x u_y \sqrt{3}$ respectively.

Measurement verifications were performed in an RC with inner dimensions of 0.94 m × 1.16 m × 1.44 m. Two stirrers were rotated synchronously with 1°/step, and 360 stirrer positions were used. Twenty-one frequency samples were collected in the frequency range of 5.98 GHz – 6.02 GHz at each stirrer position. With 360 stirrer positions, we have 21×360=7560 samples and the PDF of the magnitude of the measured S_{21} is illustrated in Fig. 3 (a). By tuning the magnitude of the input signal at each frequency and each stirrer position, the output PDF can be shaped. Instead of using a constant input magnitude, σ_x is used to control the mean value of the voltage, random voltage samples with a Rayleigh distribution of $\sigma_x = 1$ V/m were generated to excite the RC as shown in Fig. 3 (b). The output histogram and the analytical equation plot are illustrated in Fig. 3 (c).
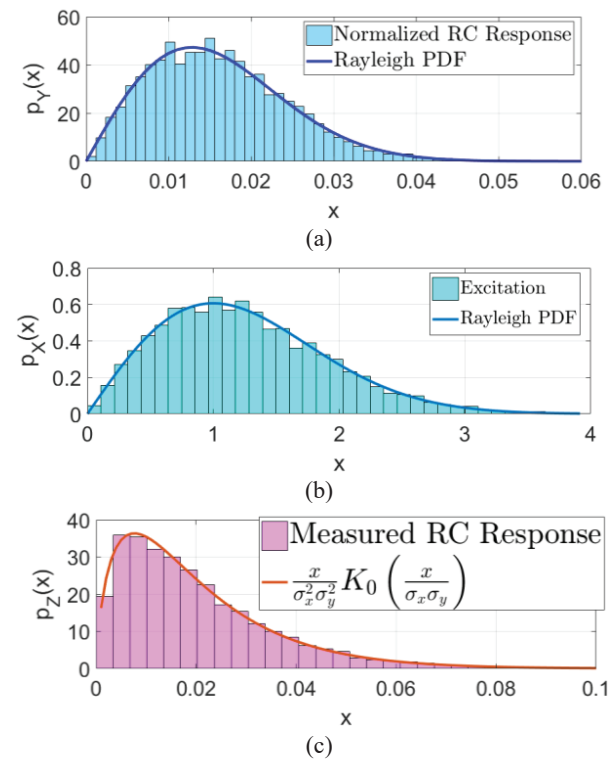
Fig. 3. (a) PDF plot of the measured normalized E-field transfer function, (b) PDF plot of excited samples, and (c) PDF plot of the magnitude of the output E-field.

Not surprisingly, a double-Rayleigh PDF was obtained for the RC response which agrees well with the analytical expression.

IV. LIMITATIONS AND GENERALIZATIONS

We have demonstrated that the PDF of the output of an RC can be synthesized with controlled input. This technique could be applied to scenarios involving channel emulations in multi-cavities. However, the output PDF cannot be arbitrary. Intuitively, one cannot synthesize a constant output (the PDF is $\delta(x-x_0)$) to eliminate the inherent statistical property of an RC. It has been shown that the Fourier transform $H_X(j\omega)$ of a PDF $p_X(x)$ (also named as characteristic function with j replaced by $--j$) has some characteristics [14]:

1) $H_X(0)=1$, it is non-vanishing in a region around zero;
2) $|H_X(j\omega)|\leq 1$, it is bounded;
3) $H_X(-j\omega)=H_X(j\omega)^*$, it is Hermitian.

Thus when two random variables are multiplied, we have $|H_X(j\omega)||H_Y(j\omega)|\leq|H_Y(j\omega)|$ and it is impossible to generate $|H_Z(j\omega)| > |H_Y(j\omega)|$. The inequality for the relative standard deviations can be derived as $\mathrm{std}_{\mathrm{rel}}(Z) = \mathrm{std}_{\mathrm{rel}}(X \times Y) \geq \mathrm{std}_{\mathrm{rel}}(Y)$. The proof is detailed as follows:

From the mean inequality we have $\sqrt{\frac{1}{n}\sum_{i=1}^{n}x_i^2} \geq \frac{1}{n}\sum_{i=1}^{n}x_i$, thus the integral form is $\sqrt{\int_{-\infty}^{+\infty}p_X(x)x^2\mathrm{d}x} \geq \int_{-\infty}^{+\infty}p_X(x)x\mathrm{d}x$. When X and Y are positive random variables (e.g., E-field magnitude, power):

$$\int_0^\infty p_X(x)x^2dx \geq \left(\int_0^\infty p_X(x)xdx\right)^2, \quad (12)$$

$$\int_0^\infty p_X(x)x^2\mathrm{d}x \int_0^\infty p_Y(x)x^2\mathrm{d}x - \left(\int_0^\infty p_X(x)x\mathrm{d}x \int_0^\infty p_Y(x)x\mathrm{d}x\right)^2$$
$$\geq \left(\int_0^\infty p_X(x)x\mathrm{d}x\right)^2\left[\int_0^\infty p_Y(x)x^2\mathrm{d}x - \left(\int_0^\infty p_Y(x)x\mathrm{d}x\right)^2\right], \quad (13)$$

$$\frac{\sqrt{\int_0^\infty p_X(x)x^2\mathrm{d}x \int_0^\infty p_Y(x)x^2\mathrm{d}x - \left(\int_0^\infty p_X(x)x\mathrm{d}x \int_0^\infty p_Y(x)x\mathrm{d}x\right)^2}}{\int_0^\infty p_X(x)x\mathrm{d}x \int_0^\infty p_Y(x)x\mathrm{d}x}$$
$$\geq \frac{\sqrt{\int_0^\infty p_Y(x)x^2\mathrm{d}x - \left(\int_0^\infty p_Y(x)x\mathrm{d}x\right)^2}}{\int_0^\infty p_Y(x)x\mathrm{d}x}, \quad (14)$$

which is $\mathrm{std}_{\mathrm{rel}}(X \times Y) \geq \mathrm{std}_{\mathrm{rel}}(Y)$. This means that the relative standard deviation of the output cannot be reduced when the input is also a random variable.

The results can be generalized to multiple cascading cavities as shown in Fig. 1 (b). When the couplings

between cavities are small and the transfer functions are independent, the output can be expressed in the form of $Y = \prod_{i=1}^{n}Y_i$. If each Y_i has a Rayleigh distribution with parameter σ_i, the PDF of Y can be derived as

$$p_\Pi(y) = 2^{\frac{n^2-4n+2}{2}}y^{3-n}\sigma_\Pi^{n-4}\times$$

$$G\left([[],[]],[[a_1,a_2,\ldots,a_n],[]],\frac{y^2}{2^n\sigma_\Pi^2}\right), \quad (15)$$

where $G(\bullet)$ is the Meijer G-function defined in [15], $a_1 = a_2 = \cdots = a_n = (n-2)/2$ and $\sigma_\Pi = \prod_{i=1}^{n}\sigma_i$. The expected value and the standard deviations are $(\pi/2)^{n/2}\sigma_\Pi$ and $2^{-n/2}\sigma_\Pi\sqrt{4^n-\pi^n}$ respectively. When $n \to \infty$, the relative standard deviation approximates to

$$\lim_{n\to\infty}\frac{2^{-n/2}\sigma_\Pi\sqrt{4^n-\pi^n}}{(\pi/2)^{n/2}\sigma_\Pi} = \lim_{n\to\infty}\frac{2^{-n/2}\sqrt{4^n-\pi^n}}{(\pi/2)^{n/2}} \sim \left(\frac{2}{\sqrt{\pi}}\right)^n. \quad (16)$$

It is interesting to note that the relative standard deviation does not depend on parameters σ_1, σ_2, $\ldots$, σ_n and is only a function of cavity number n. Similarly, when each Y_i^2 has an exponential distribution with parameter u_i, the PDF of the power transfer function $Y^2 = \prod_{i=1}^{n}Y_i^2$ can be obtained as

$$p_{\Pi^2}(y) = y^{2-n}u_\Pi^{n-3}\times$$

$$G([[],[]],[[b_1,b_2,\ldots,b_n],[]],\frac{y}{u_\Pi}), \quad (17)$$

where $b_1 = b_2 = \cdots = b_n = n-2$ and $u_\Pi = \prod_{i=1}^{n}u_i$. The expected value and the standard deviations are u_Π and $u_\Pi\sqrt{2^n-1}$ respectively. Approximately, when n is large, by applying the CLT (Central Limit Theorem), $\ln Y = \sum_{i=1}^{n}\ln Y_i$. $\ln Y$ can be approximated using a normal distribution $N(\mu,\sigma)$. It can be found that $\mu = n(\ln 2 - \gamma)/2 + \ln\sigma_\Pi$ and $\sigma = \pi\sqrt{6n}/12$. By applying the variable transform e^Y to $\ln Y$, a lognormal PDF for Y can be obtained which is [16]

$$p(y) = e^{-\frac{(\mu-\ln y)^2}{2\sigma^2}}/\left(y\sigma\sqrt{2\pi}\right), \quad (18)$$

where the mean value and the standard deviations are $e^{\mu+\sigma^2/2}$ and $\sqrt{e^{2\mu+\sigma^2}(e^{\sigma^2}-1)}$, respectively. It is interesting to note that, although the PDF can be well approximated for $\ln Y$ by using the CLT, because of the exponential function, the mean value from the lognormal PDF is biased, i.e. $e^{\mu+\sigma^2/2} \neq (\pi/2)^{n/2}\sigma_\Pi$.

Note that we have not considered the time domain (TD) response in this work. To shape the power delay profile of the output, we may need to shape the input signal in the TD. This has been achieved by using a channel emulator in [11]. It is also possible to use

a single signal generator to achieve similar results, however, to shape the output statistics in both FD and TD is still challenging. We only emulate FD responses in this paper, when the statistical properties of the FD and TD response of a system are both in constraints, TD operations (deconvolutions with the impulse responses) would be necessary. To emulate this scenario, it would be necessary to use the measured impulse responses from multi-cavities and control the excited impulse signals precisely in the TD if a single cavity is used.

ACKNOWLEDGMENT

REFERENCES

[1] *Electromagnetic Compatibility (EMC) – Part 4-21: Testing and Measurement Techniques – Reverberation Chamber Test Methods*, IEC 61000-4-21, Ed 2.0, 2011.

[2] CTIA, *Test Plan for Wireless Large-Form-Factor Device Over-the-Air Performance*, ver. 1.2.1, Feb. 2019.

[3] D. A. Hill, *Electromagnetic Fields in Cavities: Deterministic and Statistical Theories*, Wiley-IEEE Press, Hoboken, NJ, 2009.

[4] C. L. Holloway, D. A. Hill, J. M. Ladbury, P. F. Wilson, G. Koepke, and J. Coder, "On the use of reverberation chambers to simulate a Rician radio environment for the testing of wireless devices," *IEEE Transactions on Antennas and Propagation*, vol. 54, no. 11, pp. 3167-3177, Nov. 2006.

[5] E. Genender, C. L. Holloway, K. A. Remley, J. M. Ladbury, G. Koepke, and H. Garbe, "Simulating the multipath channel with a reverberation chamber: application to bit error rate measurements," *IEEE Transactions on Electromagnetic Compatibility*, vol. 52, no. 4, pp. 766-777, Nov. 2010.

[6] J. D. Sanchez-Heredia, J. F. Valenzuela-Valdes, A. M. Martinez-Gonzalez, and D. A. Sanchez-Hernandez, "Emulation of MIMO Rician-Fading environments with mode-stirred reverberation chambers," *IEEE Transactions on Antennas and Propagation*, vol. 59, no. 2, pp. 654-660, Feb. 2011.

[7] J. Frolik, T. M. Weller, S. DiStasi, and J. Cooper, "A compact reverberation chamber for hyper-Rayleigh channel emulation," *IEEE Transactions on Antennas and Propagation*, vol. 57, no. 12, pp. 3962-3968, Dec. 2009.

[8] J. D. Sánchez-Heredia, M. A. García-Fernández, M. Grudén, P. Hallbjörner, A. Rydberg, and D. A. Sánchez-Hernández, "Arbitrary fading emulation using mode-stirred reverberation chambers with stochastic sample handling," *Proceedings of the 5th European Conference on Antennas and Propagation (EUCAP)*, pp. 152-154, 2011.

[9] C. Wright and S. Basuki, "Utilizing a channel emulator with a reverberation chamber to create the optimal MIMO OTA test methodology," *Global Mobile Congress*, pp. 1-5, 2010.

[10] J. Kvarnstrand, E. Silfverswärd, D. Skousen, D. Reed, and A. Rodriguez-Herrera, "Mitigation of double-Rayleigh fading when using reverberation chamber cascaded with channel emulator," *12th European Conference on Antennas and Propagation (EuCAP 2018)*, London, UK, pp. 1-5, Apr. 2018.

[11] H. Fielitz, K. A. Remley, C. L. Holloway, Q. Zhang, Q. Wu, and D. W. Matolak, "Reverberation-chamber test environment for outdoor urban wireless propagation studies," *IEEE Antennas and Wireless Propagation Letters*, vol. 9, pp. 52-56, Feb. 2010.

[12] Q. Xu, L. Xing, Y. Zhao, T. Jia, and Y. Huang, "Probability distributions of three-antenna efficiency measurement in a reverberation chamber," *IET Microwaves, Antennas & Propagation*, vol. 15, no. 12, pp. 1545-1552, May 2021.

[13] M. Höijer and L. Kroon, "Field statistics in nested reverberation chambers," *IEEE Transactions on Electromagnetic Compatibility*, vol. 55, no. 6, pp. 1328-1330, Dec. 2013.

[14] F. Oberhettinger, *Fourier Transforms of Distributions and their Inverses,* Academic Press, New York, 1973.

[15] F. W. J. Oliver, D. W. Lozier, R. F. Boisvert, and C. W. Clark, *NIST Handbook of Mathematical Functions*, Cambridge University Press, Cambridge, UK, 2010.

[16] G. Gradoni, J.-H. Yeh, B. Xiao, T. M. Antonsen, S. M. Anlage, and E. Ott, "Predicting the statistics of wave transport through chaotic cavities by the random coupling model: A review and recent progress," *Wave Motion*, vol. 51, pp. 606-621, June 2014.

Qian Xu (Member, IEEE) received the B.Eng. and M.Eng. degrees from the Department of Electronics and Information, Northwestern Polytechnical University, Xi'an, China, in 2007 and 2010, and received the PhD degree in Electrical Engineering from the University of Liverpool, UK, in 2016. He is currently an Associate Professor at the College of Electronic and Information Engineering, Nanjing University of Aeronautics and Astronautics, China.

He was as a RF engineer in Nanjing, China in 2011, an Application Engineer at CST Company, Shanghai, China in 2012. His work at University of Liverpool was sponsored by Rainford EMC Systems Ltd. (now part of Microwave Vision Group) and Centre for Global Eco-Innovation. He has designed many chambers for the industry and has authored the book *Anechoic and Reverberation Chambers: Theory, Design, and Measurements* (Wiley-IEEE, 2019). His research interests include statistical electromagnetics, reverberation chamber, EMC, and over-the-air testing.

Feng Tian received the B.Eng. degree from University of Electronic Science and Technology of China, Chengdu, China, in 2008, and received M.Eng. degree from CETC 14th Institute, Nanjing, China, in 2011. He is currently a PhD student at the College of Electronic and Information Engineering, Nanjing University of Aeronautics and Astronautics, China. His research interests include power amplifier, EMC, and antennas.

Yongjiu Zhao received the M.Eng. and Ph.D. degrees in Electronic Engineering from Xidian University, Xi'an, China, in 1990 and 1998, respectively. Since March 1990, he has been with the Department of Mechano-Electronic Engineering, Xidian University where he was a professor in 2004. From December 1999 to August 2000, he was a Research Associate with the Department of Electronic Engineering, The Chinese University of Hong Kong. His research interests include antenna design, microwave filter design and electromagnetic theory.

Rui Jia received the B.Eng. degrees from the Department of Electronics and Information, Zhengzhou University, Zhengzhou, China, in 2008, and received the M.Eng. and Ph.D. degrees in Electronic Engineering from Mechanical Engineering College, Shijiazhuang, China, in 2010 and 2014, respectively. His research interests include statistical electromagnetics, reverberation chamber, and EMC.

Erwei Cheng received the M.Eng. degrees in Electronic Engineering from Mechanical Engineering College, Shijiazhuang, China, in 2009. He is currently an Associate Professor at the National Key Laboratory on Electromagnetic Environment Effects, Army Engineering University Shijiazhuang Campus, China.

Lei Xing received the B.Eng. and M.Eng. degrees from the School of Electronics and Information, Northwestern Polytechnical University, Xi'an, China, in 2009 and 2012. She received PhD degree in Electrical Engineering and Electronics at the University of Liverpool, UK, in 2015. She is currently an Associate Professor at the College of Electronic and Information Engineering, Nanjing University of Aeronautics and Astronautics, China.

A Novel Method for the Low-detectable Dihedral Corner Utilizing Phase Gradient Metasurface based on Phase Cancellation Mechanism

Qingting He[1], Jianliang Xie[1], Qian Liu[1], Xin Yao[1], Zhi Wang[2], Haiyan Chen[1*], Fengxia Li[3], and Longjiang Deng[1]

[1]National Engineering Research Center of Electromagnetic Radiation Control Materials
Key Laboratory of Multi-Spectral Absorbing Materials and Structures of Ministry of Education
State Key Laboratory of Electronic Thin Films and Integrated Devices
University of Electronic Science and Technology of China, Chengdu, 611731, People's Republic of China
hqt@std.uestc.edu.cn, jlxie@uestc.edu.cn, lq96@std.uestc.edu.cn, 2835025811@foxmail.com,
*chenhy@uestc.edu.cn, dfliang@uestc.edu.cn, denglj@uestc.edu.cn

[2]Glasgow College, University of Electronic Science and Technology of China
Chengdu, 610054, People's Republic of China
2019190503033@std.uestc.edu.cn

[3]School of Physics and Optoelectronic Engineering, Xidian University
Xi'an, 710071, People's Republic of China
lifengxia@xidian.edu.cn

Abstract – In this paper, a phase gradient metasurface (PGM) is proposed to reduce the radar cross-section (RCS) of the dihedral corner based on phase cancellation mechanism. The phase cancellation mechanism is used to derive the formula of the low-detectable dihedral corner for the first time, which is directly used to deal with the wave path difference problem that introduced by the dihedral corner. According to the formula, six sub-cells are designed with a $60°$ phase difference, which is arranged by sub-array along the y-axis. The reflection coefficients of the selected sub-cells are all above 0.8. The RCS reduction of the dihedral corner achieves over 10 dB from 4.9 GHz to 5.14 GHz under an incident angle of $45°$. In particular, the RCS reduction of the low-detectable dihedral corner is 13.97 dB at 5 GHz. Meanwhile, the proposed dihedral corner with PGM also has an excellent performance of angle insensitivity ranging from $0°$ to $75°$. To further verify our design, the dihedral corner with PGM is manufactured by a low-cost printing circuit board technique. The measured results agreed well with the simulations, and both of them show an excellent performance of RCS reduction in the operating frequency band, regardless of any angle within $75°$. Overall, the dihedral corner with PGM that we proposed has the advantages of being low-detectable, low-profile, low-cost, lightweight, and it is easy to design and manufacture. It has wide application prospects in the future.

Index Terms – low-detectable dihedral corner, low-profile metasurface, phase cancellation, phase gradient metasurfaces, radar cross-section, wave path difference.

I. INTRODUCTION

The dihedral corner, which normally forms between the aircraft's tails, is a typical scattering structure of a radar target. Its feature recognition is of crucial significance for detecting complicated targets, and it also serves as the basis for researching the scattering properties of gradual scatters. In the design of low-detectable targets, the dihedral corner is a significant scattering source, and it is critical to regulate its scattering characteristics. At present, the control methods for dihedral corner scattering characteristics mainly include the loading of lossy materials [1–2], optimization of the included angle of the dihedral corner [3–4], passive loading [5–6], etc.

Metasurface [7–9] is a sub-wavelength unit with special manipulability for amplitude, phase, and polarization of electromagnetic (EM) waves, which has been applied in many fields, such as metalenses [10–11], perfect absorbers [12–13], holograms [14–15], polarization controllers [16–17], anomalous reflection [18–19], and radar cross-section (RCS) reduction [20–21]. As an important type of metasurface, phase gradient metasurface (PGM) consists of a series of phase discontinue cells, which were first mentioned

by Yu [22]. In [22], it generates an optical vertices beam by constructing eight different reflection angles. Thenceforth, PGM has gained extensive attention [23–25]. By regulating the phase gradient of PGM, the wavefront of the electromagnetic wave can be changed as needed, so that PGM provides another method for the scattering control of the dihedral corner. However, the research on RCS reduction of PGM is mainly focused on the flat [23–25]. As far as we know, PGM is hardly ever used for the RCS reduction design of the dihedral corner [9]. An approach to achieve RCS reduction of the dihedral corner where the RCS is determined by multiple-bounce mechanisms is proposed [9]. The suggested method additionally makes use of array theory to specify precise guidelines to avoid grating lobes [9]. Nevertheless, they ignored the issue of the wave path difference that the dihedral corner itself introduced. According to the related researches, the wave path difference is particularly important to solve the RCS reduction of the dihedral corner, and it is necessary to carry out this research in-depth.

In this paper, the method of phase cancellation, by combining the wave path difference between two planes of the dihedral corner with the phase gradient of the PGM was presented to control the RCS of the dihedral corner. The formula of the low-detectable dihedral corner, which directly addresses the wave path difference issue that the dihedral corner itself introduces, is derived based on phase cancellation mechanism for the first time. The working principle is given in detail. The RCS reduction of the dihedral corner with PGM achieves over 10 dB between 4.9 GHz and 5.14 GHz at a 45° incidence angle. In particular, the RCS reduction of the low-detectable dihedral corner is 13.97 dB at 5 GHz. Furthermore, the suggested dihedral corner with PGM shows outstanding property in terms of angle insensitivity between 0° and 75°. Above all, simulation and measurement demonstrate that our method can reduce the dihedral corner's RCS. The dihedral corner with PGM has potential applications in reducing the RCS of the dihedral corner.

II. DESIGN AND SIMULATION

The dihedral corner usually consists of two perfect electric conductors (PECs) in xoy and yoz planes, as shown in Fig. 1. When the plane wave is incident on PEC along yoz at 45°, it will be reflected onto the xoy plane according to generalized Snell's law. Due to differing propagation pathways, the phase difference will appear, resulting in a strong scattering far-field, this will increase the possibility of detecting. To solve this problem, PGM is intended to replace PEC in the xoy plane to compensate for wave path difference, providing a sequence of continuous phase abrupt of variable
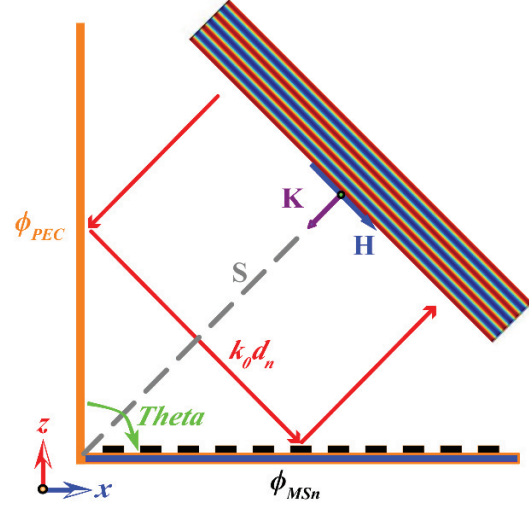
Fig. 1. Schematic of the working principle of the low-detectable dihedral corner.

size. According to the passive cancellation principle, scattering performance will rapidly decrease with a reasonable phase arrangement. The detailed design flows are as follow.

Assuming the periodicity of the sub-unit cell of PGM is p, the distance between the center point of the nth unit cell (xoy plane) and its mirror point (yoz plane) about the symmetry plane S is

$$d_n = \frac{\sqrt{2}(2n-1)}{2}p, \qquad (1)$$

where n is the position of the nth unit cell.

The plane wave incidences dihedral corner at 45°. Using the principle of phase cancellation, we can derive Equation 2,

$$\phi_{MSn} + k_0 d_n - \phi_{PEC} = \pi + 2M\pi, \qquad (2)$$

where ϕ_{MSn} and ϕ_{PEC} are the phases of the metasurface and PEC of the nth cell, respectively, $k_0 = 2\pi/\lambda_0$ is the propagation constant, λ_0 is the wavelength in free space, and M is an integer.

The reflection phase of PEC is $-\pi$, the corresponding phase of the unit cell of the PGM that needs to be designed is deduced as

$$\phi_{MSn} = -\sqrt{2}(2n-1)\pi\frac{p}{\lambda_0} + 2(m+1)\pi. \qquad (3)$$

The phase shift between adjacent cells of PGM can be derived

$$d\phi = \phi_{MS(n-1)} - \phi_{MSn} = 2\sqrt{2}\pi\frac{p}{\lambda_0}. \qquad (4)$$

It can be seen from Equation (3) that we can reduce the RCS of the dihedral corner by adjusting the phase of PGM, and the phase difference between adjacent sub-units can be determined by Equation (4).

A reflective low-profile metasurface is chosen here, which is a typical sandwich structure. The proposed

Fig. 2. Schematic illustration of the unit cell structure of metasurfaces with variable *m*.

unit cell is the type of sub-wavelength structure, and its parameters are shown in Fig. 2. The top layer is a simple copper square patch with conductivity of 5.8×10^7 S/m with length of *m*. The FR-4 substrate backed by PEC plane has thickness of $h = 3$ mm $(0.05\lambda_0)$ with dielectric constant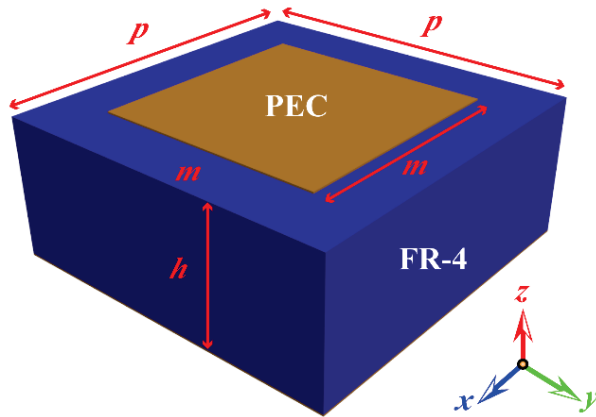 of 4.3 and loss tangent of 0.025, and the period of the cell is $p = 7.07$ mm. The phase of the metasurfaces can be adjusted by changing the parameter *m*.

To get the desired phase gradient, parameter *m* is swept by the numerical calculation software CST Studio Suite. In the simulation setup, the EM waves are incident at a 45° angle. The boundary condition is unit cell along the *x*- and *y*-axis, and open (add space) boundary along the *z*-direction. The reflection phase and the detailed geometrical parameters *m* of six sub-cells are listed at 5 GHz in Table 1. From Table 1, it can be seen that the phase difference between adjacent cells is almost 60°. In the local enlarged image of Fig. 3, the supercell of PGM is composed by these six sub-cells.

Table 1: The reflection phase and the geometrical parameters *m* of the six unit cells at 5 GHz

N	1	2	3	4	5	6
m (mm)	6.7	6.83	7.02	2.72	6.33	6.58
Phase (°)	329.89	269.46	209.90	150.23	89.53	29.95
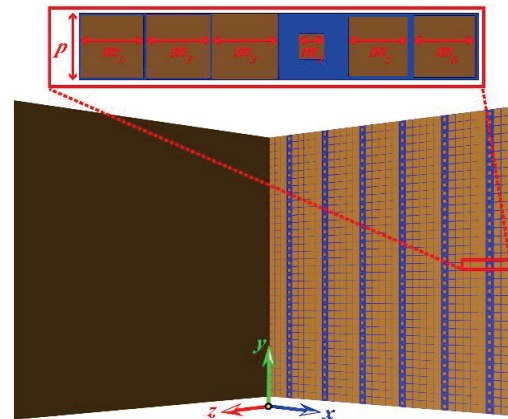
Fig. 3. Schematic diagram of the dihedral corner with metasurface. The local enlarged image corresponding to the red frame above the picture is the supercell of the designed metasurface.

All cells have a strong reflection due to the existence of PEC ground. As illustrated in Fig. 4 (a), the reflection amplitude of six sub-cells exceeds 0.8 in the simulation frequency band. Additionally, the reflection phase can cover 360° by changing the values of *m*, as shown in Fig. 4 (b).

The supercell is periodically arranged to form the PGM with the size of 254.52 mm × 254.52 mm, which is composed of 36 × 36 unit cells. In Fig. 3, we show the
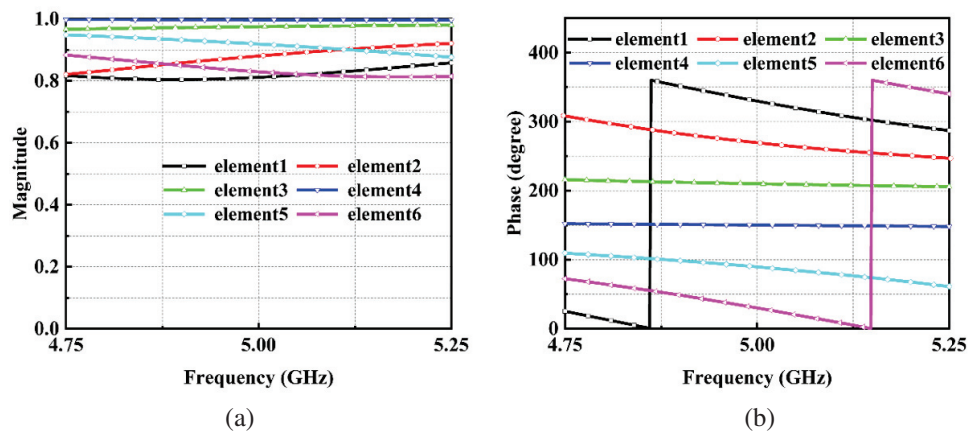
Fig. 4. Simulated reflection coefficients for the unit cells with the change of *m*, at 5 GHz, (a) amplitude and (b) phase.

dihedral corner with PGM, which is composed of PGM in the xoy plane, and the copper plate is designed with the same size in the yoz plane.

III. SIMULATION RESULTS AND DISCUSSION

To better validate the method mentioned above, the RCS of the dihedral corner with and without PGM are simulated. The dihedral corner without PGM serves as the comparison group, which only consists of metal plates. Figure 5 shows the RCS of the dihedral corner with and without PGM under transverse electric (TE) polarization wave impinging at 45°. As seen in Fig. 5, the RCS of the dihedral corner with a low-profile metasurface is significantly lower than the comparison group in the frequency range of 4.75 GHz to 5.25 GHz. The RCS reduction of the dihedral corner achieves over 10 dB from 4.9 GHz to 5.14 GHz. According to Fig. 5, the RCSs of the dihedral corner without and with PGM at 5 GHz are 13.1 dB and -0.87 dB, respectively. This means the RCS reduction of the low-detectable dihedral corner is 13.97 dB at 5GHz. The simulation results demonstrate that over 10 dB RCS reduction (RCSR) is realized at 5 GHz, which is virtually in line with the above estimate.
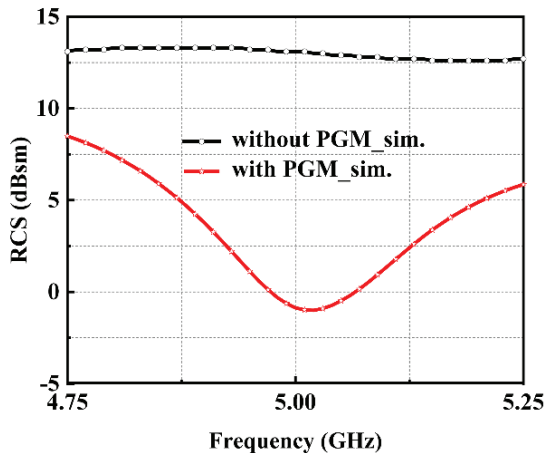
Fig. 5. Simulated RCS of the dihedral corner with and without PGM at 45° oblique incidence at different frequencies.

To further evaluate the RCSR performance, the monostatic RCS under oblique incidence is simulated at 5 GHz. As shown in Fig. 6, RCS is reduced with the variation of the incident angle range from 0° to 75°. As a result, the proposed dihedral corner with PGM has outstanding RCS reduced performance across a specific angle range.

To better understand the mechanism of RCS reduction, the 3D bistatic scattering patterns of the
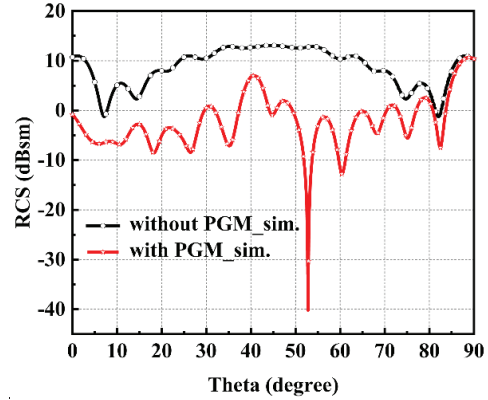
Fig. 6. Simulated RCS of the dihedral corner with and without PGMs at 5 GHz at different azimuth angle.

dihedral corner with and without PGM are illustrated when the incident angle is 45° and the operation frequency is at 5 GHz, as shown in Fig. 7. The RCSs of the dihedral corner without and with PGM are 13.1 dB and -0.87 dB, respectively. The reflected energy of the dihedral corner without PGM is centered on the main lobe, as shown in Fig. 7 (a). On the contrary, the main lobe is split, and the magnitude has a significant reduction when PGM is loaded, as seen in Fig. 7 (b). According to the energy conservation principle, the main lobe of the dihedral corner with PGM is effectively suppressed. Therefore, the dihedral corner with the purposed PGM has the property of RCS reduction.
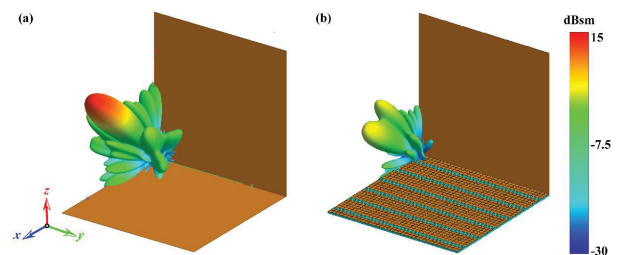
Fig. 7. 3D bistatic scattering pattern of the dihedral corner under oblique incidence angle at 45° at 5 GHz, (a) without metasurface and (b) with metasurface.

IV. MEASUREMENT RESULTS

To further verify our design, a sample with a size of 254.52 mm × 254.52 mm is manufactured by low-cost printing circuit board (PCB) technology. Figure 8 exhibits the photograph of the sample with a zoomed view of the 1 × 6 array of PGM's supercell. The RCS of the sample is measured in the microwave anechoic chamber. The measured results are compared at various frequencies when the plane wave is incident at 45°.
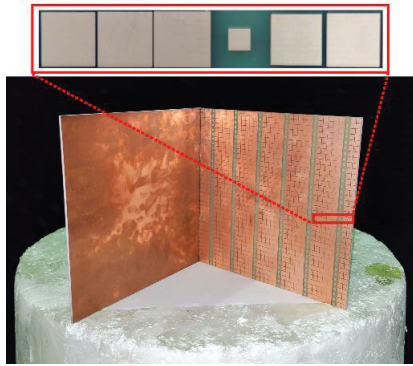
Fig. 8. The photograph of the manufactured sample. The local enlarged image corresponding to the red frame above the picture is the supercell of the designed metasurface.

To verify the accuracy of the measurement, we replot the simulation results in Fig. 9. The experimental results are in good agreement with the simulation results. The experimental results demonstrate that the RCS of the dihedral corner with PGM is obviously lower than the dihedral corner without PGM in the frequency range of 4.75 GHz to 5.25 GHz. The RCS reduction of the dihedral corner achieves over 10 dB from 4.95 GHz to 5.11 GHz. In Fig. 5, the RCSs of the dihedral corner without and with PGM are 12.03 dB and -1.08 dB at 5 GHz, respectively. Namely, the RCS reduction of the low-detectable dihedral corner is 13.05 dB at 5GHz. From Fig. 9, the results of simulations and measurements show that over 10 dB RCSR is achieved at 5 GHz, which is essentially in line with the aforementioned design.

Meanwhile, to assess the RCSR's performance, we measured the RCS of the dihedral corner with and without PGM at 5 GHz at different azimuth angles.
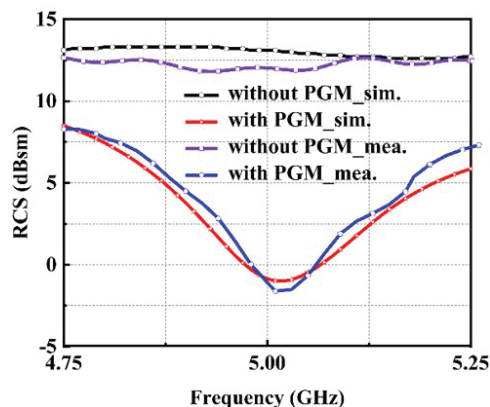
Fig. 9. Simulated and measured RCS of the dihedral corner with and without PGM at 45° oblique incidence at different frequencies.
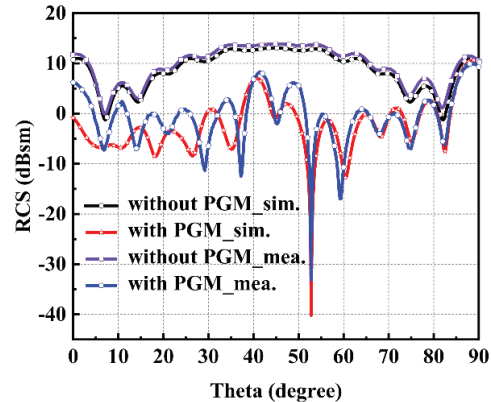
Fig. 10. Simulated and measured RCS of the dihedral corner with and without PGM at 5GHz at different azimuth angles.

Similar to Fig. 9, we display the simulation results in Fig. 10. The sample shows excellent angle insensitivity performance in the range of 0° to 75°, as illustrated in Fig. 10. Both of them agree well with simulation results, with slight deviations due to manufacturing and measurement errors. Above all, the measurements corroborate our method and demonstrate that our design can reduce the RCS of the dihedral corner.

V. CONCLUSION

In this paper, a novel design method has been proposed to reduce the RCS of the dihedral corner according to the principle of phase cancellation combined with PGM. With the loading of a low-profile metasurface $(0.05\lambda_0)$ on the dihedral corner, phase cancellation is performed directly on the wave path difference introduced by the dihedral structure itself, to achieve RCS reduction of the dihedral corner. The guidance formula of a low-detectable dihedral corner based on phase cancellation mechanism is derived for the first time, which directly solves the wave path difference issue due to the dihedral corner structure itself. According to the guiding formula, six different phase reflection sub-cells are designed with 60° phase differences. Low-detectable dihedral corners are demonstrated to be effective in reducing the backscattered power utilizing the simulation of RCS and 3D bistatic scattering patterns. Both simulation and experiment show an excellent RCS reduction over 10 dB at 5 GHz with a 45° incident angle. Moreover, the PGM is still effective when the incidence angle ranges from 0° to 75°. This study provides a novel and meaningful approach to design a low-RCS dihedral corner, which can be applied to complex electromagnetic regulation scenarios. The low-detectable dihedral corner also has the benefit of being lightweight because it only requires one-sided loading with the low-profile metasurface,

which was manufactured by a low-cost PCB technique. To verify the effectiveness of the method, we only show its application in the microwave band. Actually, the method can be used at any frequency. Furthermore, the method does not entail absorbing materials. So, it has the potential to be used in high-temperature settings.

ACKNOWLEDGMENT

REFERENCES

[1] T. Griesser, C. A. Balanis, and K. Liu, "RCS analysis and reduction for lossy dihedral corner reflectors," *Proc. IEEE.*, vol. 77, pp. 806-814, 1989.

[2] Y. Hingcheng and H. Peikang, "Po analysis for RCS of nonorthogonal dihedral corner reflectors coated by RAM," *J. Syst. Eng. Electron.*, vol. 12, pp. 1-6, 2001.

[3] E. Knott, "RCS reduction of dihedral corners," *IEEE Trans. Antennas Propag.*, vol. 25, pp. 406-409, 1977.

[4] D. K. Atwood and L. Thirion-Lefevre, "Polarimetric phase and implications for urban classification," *IEEE Trans. Geosci. Remote Sens.*, vol. 56, pp. 1278-1289, 2018.

[5] A. Y. Modi, C. A. Balanis, C. R. Birtche, and H. N. Shaman, "New class of RCS-reduction metasurfaces based on scattering cancellation using array theory," *IEEE Trans. Antennas Propag.*, vol. 67, pp. 298-308, 2019.

[6] A. Y. Modi, M. A. Alyahya, C. A. Balanis, and C. R. Birtcher, "Metasurface-based method for broadband RCS reduction of dihedral corner reflectors with multiple bounces," *IEEE Trans. Antennas Propag.*, vol. 68, pp. 1436-1447, 2020.

[7] G. Liu, J. Han, X. Gao, H. Liu, and L. Li, "A novel frequency reconfigurable polarization converter based on active metasurface," *Applied Computational Electromagnetics Society (ACES) Journal*, vol. 34, pp. 1058-1063, 2019.

[8] L. N. Nguyen, "A new metasurface structure for bandwidth improvement of antenna array," *Applied Computational Electromagnetics Society (ACES) Journal*, vol. 36, pp. 139-144, 2021.

[9] A. A. Abbas and B. S. Samet, "A compact high gain wideband metamaterial antenna for sub-6 GHz applications," *Applied Computational Electromagnetics Society (ACES) Journal*, vol. 37, pp. 886-89, 2022.

[10] Y. Meng, Y. Chen, L. Lu, Y. Ding, A. Cusano, J. A. Fan, Q. Hu, K. Wang, Z. Xie, Z. Liu, Y. Yang, Q. Liu, M. Gong, Q. Xiao, S. Sun, M. Zhang, X. Yuan, and X. Ni, "Optical meta-waveguides for integrated photonics and beyond," *Light Sci. Appl.*, vol. 10, pp. 235, 2021.

[11] Y. Wang, Q. Chen, W. Yang, Z. Ji, L. Jin, X. Ma, Q. Song, A. Boltasseva, J. Han, V. M. Shalaev, and S. Xiao, "High-efficiency broadband achromatic metalens for near-IR biological imaging window," *Nat. Commun.*, vol. 12, pp. 5560, 2021.

[12] Y. Yao, R. Shankar, M. A. Kats, Y. Song, J. Kong, M. Loncar, and F. Capasso, "Electrically tunable metasurface perfect absorbers for ultrathin mid-infrared optical modulators," *Nano Lett.*, vol. 14, pp. 6526-6532, 2014.

[13] A. Tittl, A.-K. U. Michel, M. Schäferling, X. Yin, B. Gholipour, L. Cui, M. Wuttig, T. Taubner, F. Neubrech, and H. Giessen, "A switchable mid-infrared plasmonic perfect absorber with multispectral thermal imaging capability," *Adv. Mater.*, vol. 27, pp. 4597-4603, 2015.

[14] X. Ni, A. V. Kildishev, and V. M. Shalaev, "Metasurface holograms for visible light," *Nat. Commun.*, vol. 4, Art. no. 2807, 2013.

[15] G. Zheng, H. Mühlenbernd, M. Kenney, G. Li, T. Zentgraf, and S. Zhang, "Metasurface holograms reaching 80% efficiency," *Nat. Nanotechnol.*, vol. 10, pp. 308-312, 2015.

[16] N. K. Grady, J. E. Heyes, D. R. Chowdhury, A. R. Dalvit, and A. Chen, "Terahertz metamaterials for linear polarization conversion and anomalous refraction," *Science*, vol. 340, pp. 1304-1307, 2013.

[17] B. Kamal, J. Chen, Y. Yingzeng, J. Ren, S. Ullah, and W. U. R. Khan, "High efficiency and ultra-wideband polarization converter based on an L-shaped metasurface," *Opt. Mater. Express.*, vol. 11, pp. 1343-1352, 2021.

[18] G. Dong, Z. Jiang, and Y. Li, "Large asymmetric anomalous reflection in bilayer gradient metasurfaces," *Opt. Express.*, vol. 29, pp. 16769-16780, 2021.

[19] M. B. Soley, K. N. Avanaki, and E. J. Heller, "Reducing anomalous reflection from complex absorbing potentials: A semiclassical approach," *Phys. Rev. A.*, vol. 103, Art. no. L041301, 2021.

[20] T. J. Cui, M. Q. Qi, X. Wan, J. Zhao, and Q. Cheng, "Coding metamaterials, digital metamaterials and programmable metamaterials," *Light Sci. Appl.*, vol. 3, e218-e218, 2014.

[21] Y. Liu, Y. Hao, K. Li, and S. Gong, "Wideband and polarization-independent radar cross section reduction using holographic metasurface," *IEEE*

Antennas Wirel. Propag. Lett., vol. 15, pp. 1028-1031, 2015.

[22] N. Yu, P. Genevet, M. A. Kats, F. Aieta, J. Tetienne, F. Capasso, and Z. Gaburro, "Light propagation with phase discontinuities: Generalized laws of reflection and refraction," *Science*, vol. 334, pp. 333-337, 2011.

[23] Y. Li, J. Zhang, S. Qu, J. Wang, H. Chen, L. Zheng, Z. Xu, and A. Zhang, "Achieving wideband polarization-independent anomalous reflection for linearly polarized waves with dispersionless phase gradient metasurfaces," *J. Phys. D: Appl. Phys.*, vol. 47, Art. no. 425103, 2014.

[24] Y. Li, J. Zhang, S. Qu, J. Wang, H. Chen, Z. Xu, and A. Zhang, "Wideband radar cross section reduction using two-dimensional phase gradient metasurfaces," *Appl. Phys. Lett.*, vol. 104, Art. no. 221110, 2014.

[25] F. Yuan, G.-M. Wang, H.-X. Xu, T. Cai, X.-J Zou, and Z.-H. Pang, "Broadband RCS reduction based on spiral-coded metasurface," *IEEE Antennas Wirel. Propag. Lett.*, vol. 16, pp. 3188-3191, 2017.

Qingting He received the B.S. degree in Electronic Science and Technology from the Chengdu College of University of Electronic Science and Technology of China, Chengdu, China, in 2016. She is currently working toward the Ph.D. degree in Electronic Science and Technology at the University of Electronic Science and Technology of China, Chengdu, China.

Her recent research interests have focused on the numerical modeling of novel metamaterials and their applications in wave modulation, RCS reduction and wave absorbers.

Jianliang Xie received the Ph.D. degree in Material Physics and Chemistry from the University of Electronic Science and Technology of China (UESTC), Chengdu, China, in 2008.

He has worked as a Full Professor with the National Engineering Research Center of Electromagnetic Radiation Control Materials, UESTC. His research interests include magnetic material and devices, functional macromolecules, high-quality adherence systems, and electromagnetic absorbing structures.
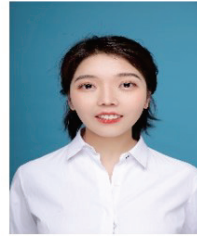
Qian Liu received the B.S. degree in Materials Science and Engineering from Leshan Normal University, Leshan, China, in 2018. She received Master of Engineering in Electronic Science and Technology from the University of Electronic Science and Technology of China (UESTC), Chengdu, China, in 2021. She is currently working toward the Ph.D. degree in Microelectronics and Solid States Electronics at the University of Electronic Science and Technology of China (UESTC), Chengdu, China.

Her recent research interests include the structural design of novel metamaterials and their applications in electromagnetic wave modulation, orbital angular momentum, RCS reduction and wave absorbers.

Xin Yao received the B.S. degree in Electronic Science and Technology from Chongqing University of Posts and Telecommunications (CQUPT), Chongqing, China, in 2020. He is currently working toward the Ph.D. degree in Electronic Science and Technology at the University of Electronic Science and Technology of China (UESTC), Chengdu, China.

His recent research interests include the structural design of novel metamaterials and their applications in RCS reduction, de-coupling and sidelobe suppression for antenna arrays.

Zhi Wang is currently working toward the B.S. degree in Electronics and Electric Engineering with Information Engineering from University of Electronic Science and Technology of China (UESTC), Chengdu, China.

His recent research interests include RCS reduction and wave absorbers based on digital image processing, machine learning and smart heating in smart homes.

Haiyan Chen received the PH.D. degree in Microelectronics and Solid States Electronics from the University of Electronic Science and Technology of China (UESTC), Chengdu, China, in 2011. In 2015, he received the CSC (Chinese Scholarship Council) scholarship, and pursued study at the department of Engineering, University of Kentucky, Lexington, KY, USA, as a Visiting Scholarship.

Since 2012, he has been with the National Engineering Research Center of Electromagnetic Radiation Control Materials, UESTC, where he is now an Associate Professor. His research interests include artificial electromagnetic material and electromagnetic radiation control materials, particularly the study of electromagnetic discontinuous repair materials.

Fengxia Li received the B.S. degree in Electronic Information Science and Technology from Henan Polytechnic University, Jiaozuo, China, in 2015, and the Ph.D. degree in Microelectronics and Solid States Electronics from the National Engineering Research Center of Electromagnetic Radiation Control Materials, UESTC, in 2021.

Since 2021, she has been working with the School of Physics and Optoelectronic Engineering, Xidian University, as a Lecturer.

Her recent research interests include the structural design of novel metamaterials and their applications in electromagnetic wave modulation, frequency selective surfaces, RCS reduction, and wave absorbers.

Longjiang Deng received the M.S. degree in Electronic Material and Device from the University of Electronic Science and Technology of China (UESTC), Chengdu, China, in 1987.

Since then he has been working with UESTC, as a Lecturer, Associate Professor, and a Full Professor. He has authored/coauthored about 200 papers in peer-reviewed international journals and industry publications, and given many invited talks in international conferences. His research interests include electromagnetic wave absorbing material, infrared low emissivity and selective emissivity thin film, and microwave magnetic material.

Prof. Deng is a member of the Branch of Chinese Institute of Electronics on Microwave Magnetism, the Vice Director of the Special Committee of Chinese Institute of Electromagnetic Material, and a Member of the Editor Committee of *Chinese Journal of Functional Material*.

An Ultra-small Heated Area Masked Microwave Hyperthermia Therapy Scheme in Fresnel Region

Tamer G. Abouelnaga[1] and Maha R. Abdel-Haleem[2]

[1]Microstrip Circuits Department, Electronics Research Institute ERI, Cairo, Egypt
Tamer@eri.sci.eg

[2]Banha Faculty of Engineering, Banha University, Banha, Egypt

Abstract – This paper introduces a localized masked thermal therapy method for only the breast through the Fresnel region. A pyramidal horn antenna has been used as a hyperthermia system applicator. The antenna is fed by a Yagi array and resonates at 4.74 GHz. A metal plate with a square slot masked the breast phantom. The antenna irradiates the breast phantom for 5 and 10 minutes with input power of 10 and 20 watts (W). Thermal and specific absorption rate (SAR) distributions are studied under the same conditions for a fair comparison between masked and unmasked system performance. The square slot dimensions are altered, and their effects are studied considering the phantom heated area. Moving from unmasked to masked hyperthermia scenarios, a heated area size reduction of 99.87 % is achieved along with a very considerable SAR value reduction. The masked scenario elevates the breast temperature to 43 $^{\circ}$C in a very concentrated area. The proposed system can elevate only an area of 2×2 mm^2 of the breast tissue to a temperature of 40 $^{\circ}$C in 5 minutes, and that is a very promising result in hyperthermia therapy applications.

Index Terms – antenna, array, hyperthermia, near-field, SAR.

I. INTRODUCTION

Hyperthermia is a therapeutic procedure used for the treatment of some cases of cancer [1, 2]. To destroy the cancerous cell, the tumor temperature is raised to a higher value than the surrounding normal body tissues. It involves achieving and maintaining temperatures of the order of 42-45°C for several minutes at the tumor location. A higher level of water content present in tumor cells increases their conductivity, leading to higher absorption of electromagnetic energy. It has been shown [3, 4] that hyperthermia treatment increases the effectiveness of chemotherapy and radiotherapy. Hyperthermia can be performed on the whole body, or be regional or localized, depending on the size of the tissue region to be heated. In localized hyperthermia, only the local tumor region is heated and is mainly used for the treatment of superficial tumors. Providing uniform heating and not overheating the surrounding healthy tissue region are the two most important challenges associated with hyperthermia.

Based on the mechanism used for heating, the hyperthermia applicator's exposure region can be classified into near- and far-field. In far-field exposure, a directive antenna is used under free space conditions for exposing biological samples [5–7]. Many techniques have been applied to analyze the power density distribution in the sample under test [7]. Far-field exposures have low exposure efficiency (10-15%). For an antenna to achieve high power density, there are two possible ways: Increase the output power [6, 7], or add an extra parameter for enhancing power transfer to the tissue [5]. Hence recent research has moved to near-field exposure which offers better exposure efficiency and results in high power density levels absorbed by the biological sample. A literature review of antenna arrays used for hyperthermia treatment and operating in the near-field region is introduced and summarized in Table 1. The comparison considers the frequency of operation (f$_o$), the antenna type and area, the distance from the phantom (D), and the targeted tissue region. In addition, it shows whether any matching medium was used with the applicator or not.

In this paper, a masked electromagnetic near-field effect over a human voxel model for different power and exposure time values is described. Human breast phantom is chosen for investigating near-field exposure effects on hyperthermia therapy efficiency. Firstly, the system performance is tested in the applicator's Fresnel region at a distance with a maximum value of normalized power density. Then, it is masked by 12×12 cm^2 of conducting metal sheet. The sheet has a square slot at its center. The square slot dimensions are altered and its effect on the breast phantom heated area is investigated. SAR and thermal results are obtained using the computer simulation technology (CST) simulator under the same

Table 1: Different hyperthermia applicators

Ref.	[8]	[9]
f_o (GHz)	0.915	0.433
Tissue	Arm	Fat
Applicator	8-dipole array	4×2 planar array
Area cm^2	22×22	56×50
D (cm)	2	17.4
Matching med.	Water bolus	Water bolus
Results	E-field	SAR
Ref.	[10]	[11]
f_o (GHz)	2.45	1.8
Tissue	Breast	Breast
Applicator	water-loaded diagonal horns	16 flexible planar antennas
Area cm^2	15×15×0.2	2.336× 3.921
D (cm)	0	0
Matching med.	Water bolus	Customized liquid
Results	E-field and SAR	Heat and SAR
Ref.	[12]	[15]
f_o (GHz)	4.86	2.45
Tissue	Breast	Breast
Applicator	Rectangular grid array	Circular grid array
Area cm^2	15×17.5	170 x 250
D (cm)	6	8.7
Matching med.	No	No
Results	Heat	SAR and Heat

condition for a fair comparison. The breast phantom is exposed to the antenna's electromagnetic wave for 5 and 10 minutes and with different input power (10 W and 20 W) at the applicator input. The suggested system can raise only a 2×2 mm^2 patch of breast tissue to a temperature of 40 °C in 5 minutes, which is a highly encouraging finding for applications of hyperthermia treatment.

II. HYPERTHERMIA THERAPY IN FRESNEL REGION

In this section, the applicator and its parameters are investigated. The proposed hyperthermia setup with and without the metal mask is presented.

A. Dielectric loaded Yagi fed dual band pyramidal horn applicator

The main goal of designing a hyperthermia applicator is to destroy the cancerous tissue with minimal damage to the healthy cells. A narrow beamwidth and low sidelobe level pyramidal horn antenna at 4.74 GHz based on placing a ten directors Yagi array as an exciter have been introduced in [13]. The dimensions of the rectangular waveguide, with ($b \leq a$) and $L = 0.75\lambda g = 0.75c/f$, as shown in Fig. 1 (a), are given by equation (1)

where λg is the guided wavelength, and μ, ε, and c are the medium permeability, permittivity, and speed of the light respectively.

$$f_c = \frac{1}{2\sqrt{\mu\varepsilon}}\sqrt{\left(\frac{m}{a}\right)^2+\left(\frac{n}{b}\right)^2}. \qquad (1)$$

For air-filled waveguide, operating frequency $f = 4.74\ GHz$ and cutoff frequency $f_c = 3\ GHz$, the waveguide dimensions a, b, and λ_g are found to be 5 cm, 3 cm, and 19.16 cm, respectively, considering the Transverse Electric TE_{10} mode. The pyramidal horn antenna is fed by the Yagi array. The design equations for the pyramidal horn antenna are given by:

$$G = 10log_{10}\ G_o. \qquad (2)$$

The desired antenna gain G_o is assumed to be 15 dB:

$$a_1 = \sqrt{3\lambda\rho_h}, \qquad (3)$$
$$b_1 = \sqrt{2\lambda\rho_e}. \qquad (4)$$

The pyramidal horn slant height is determined by:

$$l_e = (b_1-b)\sqrt{\left(\frac{\rho_e}{b_1}\right)^2 - \frac{1}{4}}. \qquad (5)$$

Antenna sectorial E and H-Plane are provided by:

$$\psi_e = \sin^{-1}\frac{b_1}{2\rho_e}, \qquad (6)$$
$$\rho_e = x_1\lambda\ \lambda \qquad (7)$$
$$\psi_h = \sin^{-1}\frac{a_1}{2\rho_h}, \qquad (8)$$
$$\rho_h = \frac{\lambda G^2}{8x_1\ \pi^3}, \qquad (9)$$
$$x_1 = \frac{G}{2\pi\sqrt{2\pi}}. \qquad (10)$$

The calculated and simulated antenna dimensions are given in Table 2.

Table 2: Pyramidal horn antenna dimensions

Dimension	a_1 (cm)	b_1 cm)	l_e cm)	ψ_e(deg)
Calculated	16.11	12.22	7.62	31.18
Simulated	11.37	9.37	10.88	16.59

A Teflon rectangular parallelepiped is used as a dielectric material where the Yagi array is placed for horn feeding purposes, as shown in Fig. 1 (a). Directors' length, position, separation, and number are chosen carefully to obtain a high gain performance. Antenna gain of 13.4 dBi, a side lobe level of −25.4 dB, and a 3 dB beamwidth of 39.3° are obtained at 4.74 GHz, as shown in Fig. 2 (a), for the E-plane. For the H-plane, gain of 13.4 dBi, a side lobe level of −25.6 dB, and a 3 dB beamwidth of 37.9° are obtained at 4.74 GHz. The co- and cross-polarization patterns are shown in Fig. 2 (b). The antenna has a minimum cross-polarization of 16 dB compared to the co-polarization pattern as
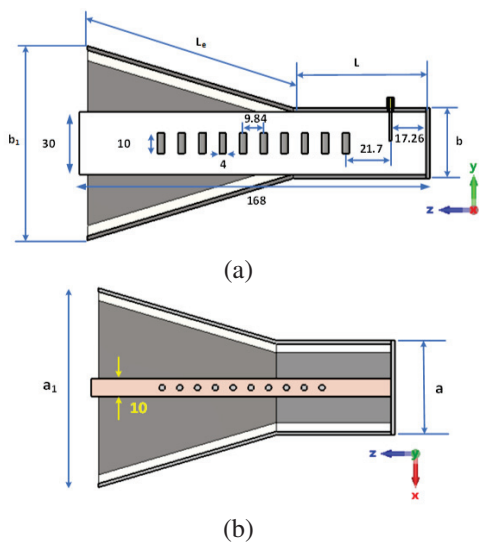
Fig. 1. Dielectric loaded pyramidal horn antenna. (a) Side view. (b) Top view.

$-90° \leq \theta \leq 90°$. The 3D radiation pattern is shown in Fig. 2 (c). The applicator is fabricated and measured for validation purposes. The measured S-parameter agreed with the simulated result with an acceptable discrepancy due to the manual assembly process of the antenna, as shown in Fig. 3. The simulated antenna bandwidth is extended from 3.65 GHz to 5.55 GHz in case of not using the Yagi fed but with a sidelobe level of -13.3 dB at 4.74 GHz. Using the Yagi fed, the sidelobe level becomes -25.6 dB at 4.74 GHz. The simulated bandwidth is extended from 3 GHz to 3.6 GHz, and from 4.6 GHz to 4.87 GHz. The antenna has a very directive beam, low side lobe level, and high-power capability, which make it very good candidate for the proposed hyperthermia application.

The depth of focus, focal plane width, and sidelobe levels are the three most crucial characteristics that may be used to describe a near-field focused (NFF) antenna [14]. The distance between two -3 dB points at the point of maximum power density in a direction normal to the
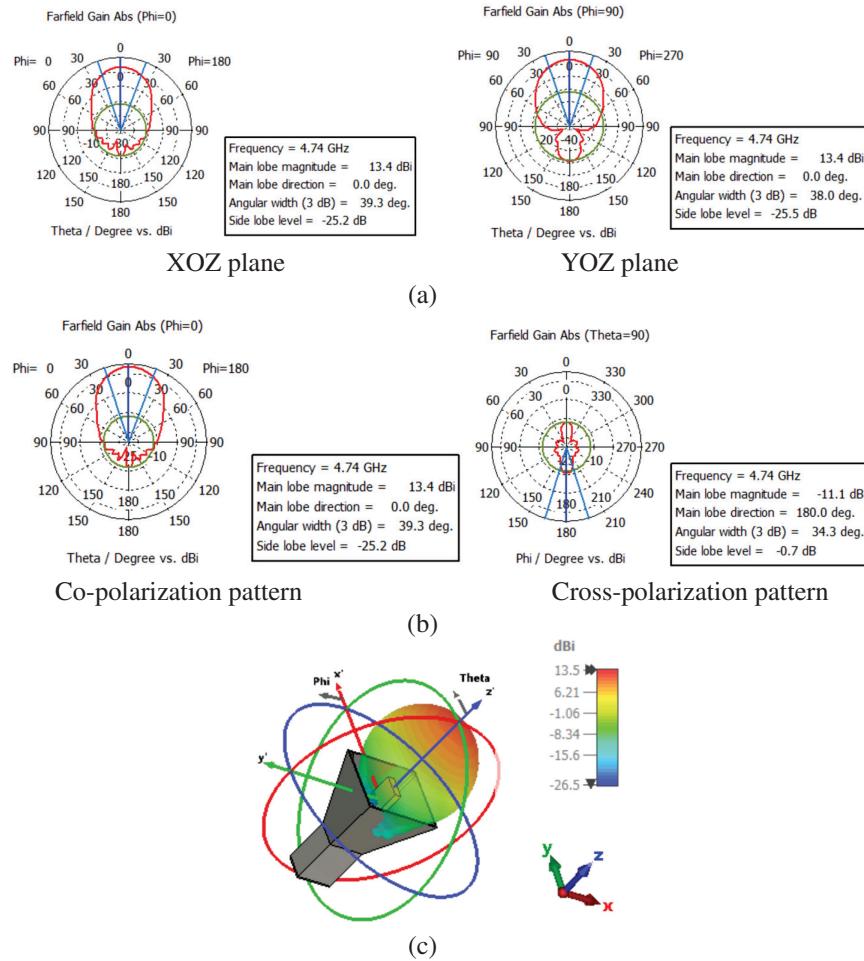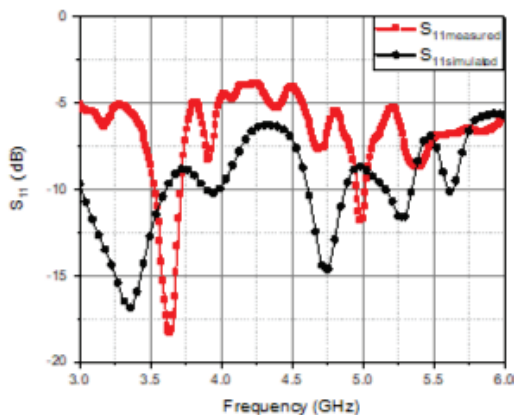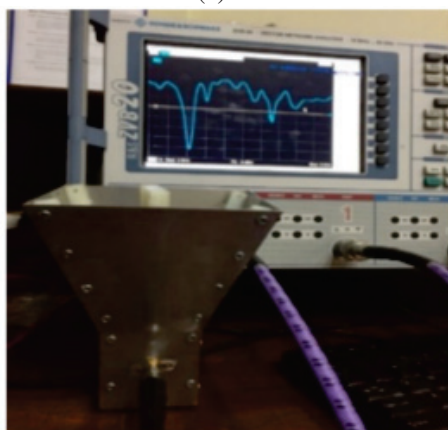

Fig. 2. (a) Simulated E-plane and H-plane. (b) Co- and cross-polarization pattern. (c) 3D radiation patterns at 4.74 GHz.

(a)

(b)

Fig. 3. (a) Simulated and measured S_{11} parameter of the dielectric pyramidal horn antenna. (b) Fabricated dual band dielectric loaded pyramidal horn antenna photo.

antenna aperture is known as the depth of focus. The term "focal plane width" refers to the area surrounding the focus point, on a plane perpendicular to the antenna aperture, where the maximum power density is larger than -3 dB on a normalised scale. For optimum hyperthermia therapy performance within the near-field exposure region, the breast phantom should be located at the distance with maximum power density. The normalised power density in the Z direction from the antenna aperture is displayed as shown in Fig. 4 with the antenna in free space. The power density in free space reaches its peak at 20 mm from the antenna aperture. The distance between the two -3 dB points on either side of the greatest power density (the depth of focus) is determined to be 125 mm. A contour map of the power density was created at the greatest power density point at $Z=20$ mm from the antenna aperture in order to determine the breadth of the focal plane spot region. As shown in Fig. 5, the focal plane's width in the XY plane is determined to be 60 by 60 mm.
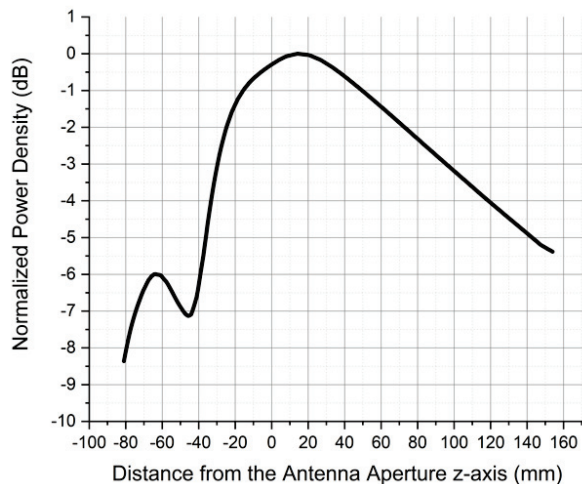
Fig. 4. Near-field normalized power density.
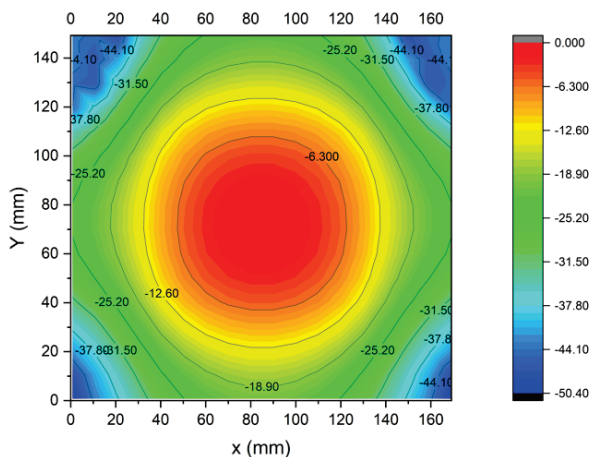
Fig. 5. Normalized power density contour at 20 mm from the antenna aperture.

B. Unmasked hyperthermia therapy setup

In medical applications, the width of the focal plane is very important where the electromagnetic energy is mostly concentrated. The tumor region should be located at the focal plane to avoid healthy tissues damage. Depending on normalized power density results, as shown in Fig. 4, the human breast phantom has been located at 20 mm along the z-axis from the antenna aperture. An ambient temperature of 38°C is considered. The breast tissue is irradiated for 5 and 10 minutes. Thermal and SAR distribution are studied at an antenna input power of 10 W and 20 W. As shown in Fig. 6, the simulated infected region temperature increases from 38 °C to 40.38 °C and 41.3 °C after an exposure time of 5 minutes and 10 minutes, respectively, with 10 W input power. While at 20 W input power, the temperature reached 43.3 °C and 45.2 °C after 5 and 10 minutes,

(a)

(b)

(c)

Fig. 6. Simulated unmasked near field. (a) Heat distribution at 5 minutes. (b) Heat distribution at 10 minutes. (c) SAR at 10 W input power.

respectively, as illustrated in Fig. 7. SAR values inside the phantom reached 0.868 and 1 W/Kg over 1 g volume for 10 W and 20 W respectively, as shown in Figs. 6 (c) and 7 (c). In contrast, it exceeded the maximum value (1.6 W/Kg averaged over 1 g volume by Federal Communication Commission FCC [16–17]) at limited points at the expense of a small (−3 dB) spot area.

C. Masked hyperthermia therapy setup

In this section, the width of the focal plane that is irradiated in the infected region of the breast is controlled

(a)

(b)

(c)
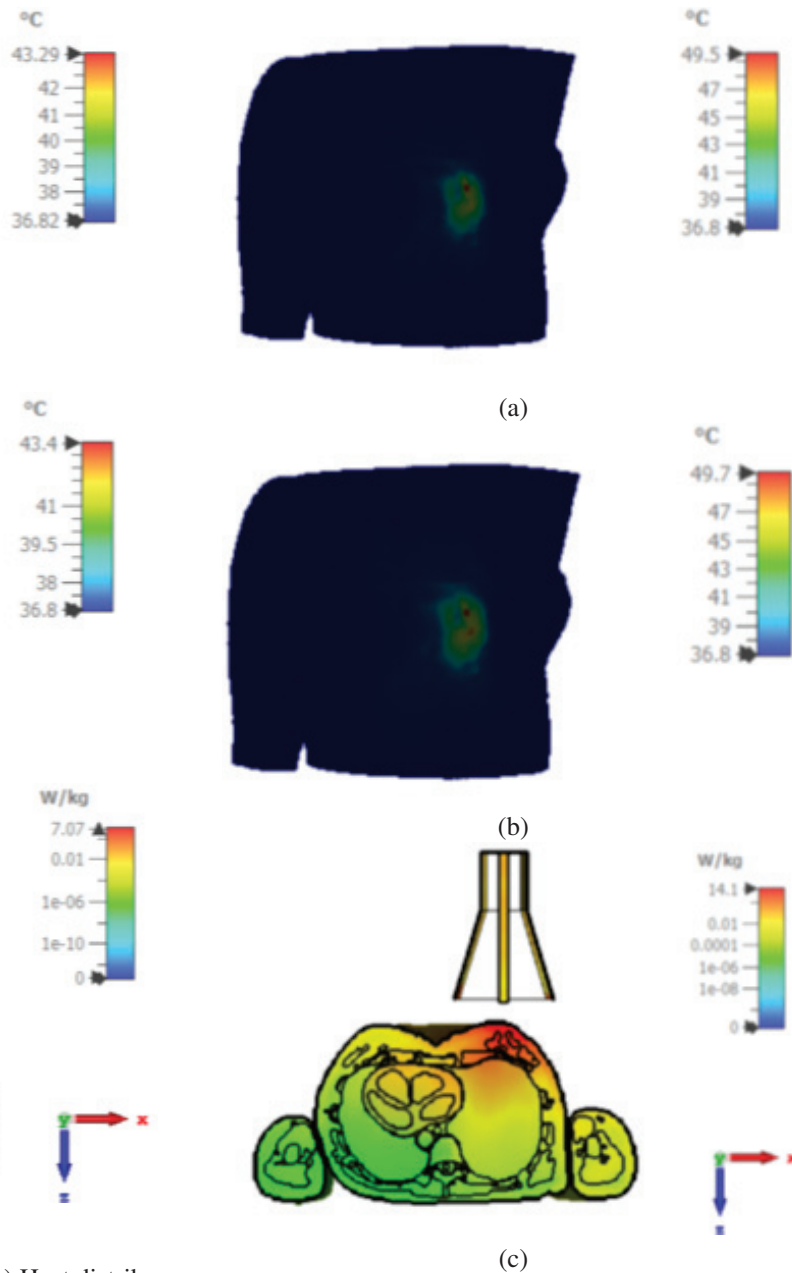
Fig. 7. Simulated unmasked near field. (a) Heat distribution at 5 minutes. (b) Heat distribution at 10 minutes. (c) SAR at 20 W input power.

by a centered slotted metal sheet with dimensions of 12×12 cm^2. The square slot is aligned with the tumor-infected area, as shown in Fig. 8 (a). The metal sheet is 20 mm from the antenna aperture and is in contact with the breast. The square slot dimensions are altered and its effect on the breast phantom heated area is given in Table 3.

Figures 8–10 show the effect of input power and exposure time on the temperature of the infected breast

(a)

(b)

(c)

(d)

Fig. 8. Simulated masked near field. (a) Scheme. (b) Heat distribution at 5 min. (c) Heat distribution at 10 min. (d) SAR at 10 W input power and mask slot dimension of 4×4 cm^2.

(a)

(b)

(c)
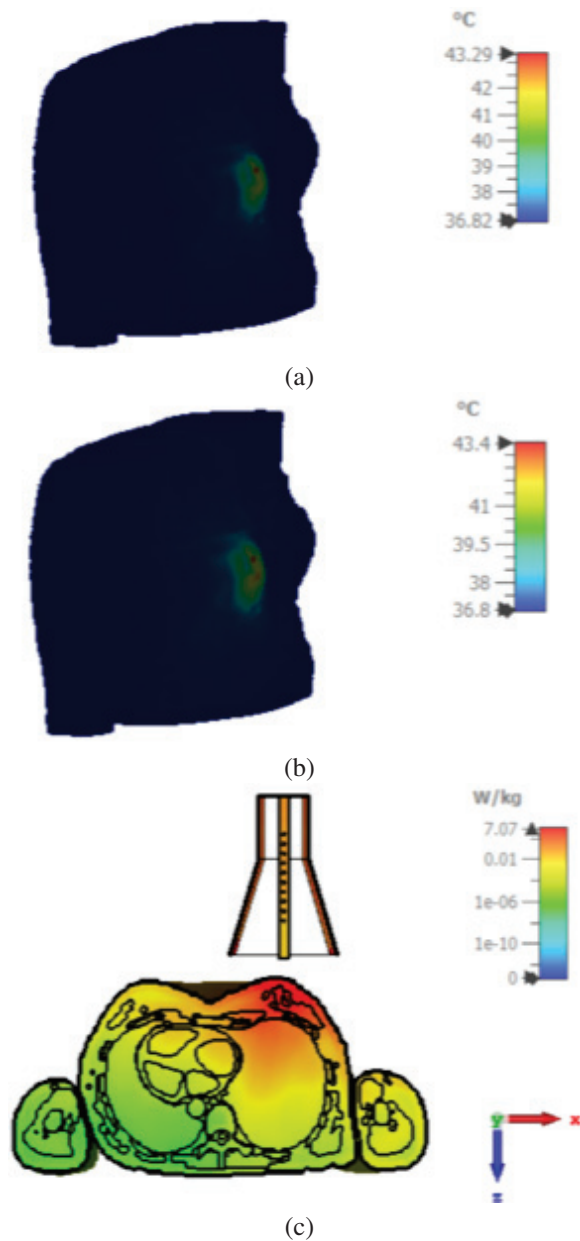
Fig. 9. Simulated masked near field. (a) Heat distribution at 5 minutes. (b) Heat distribution at 10 minutes. (c) SAR at 20 W and mask slot dimension of 4×4 cm^2.

area considering the masked scenario. The heated area is calculated considering a reference temperature of 40 °C. Considering the unmasked scenario, the heated area is 50×60 mm^2. That area is reduced to 27×35 mm^2, 15×12 mm^2, and 2×2 mm^2 considering the masked scenario and slot dimensions of 40×40 mm^2, 20×20 mm^2, and 10×10 mm^2, respectively. Input power of 20 W and exposure time of 5 min is considered in both masked and unmasked scenarios. A heated area size reduction of 99.87 % is obtained considering the masked scenario with a slot area of 10×10 mm^2. As

Table 3: Slot area effect on masked and unmasked hyperthermia schemes

Scheme	Power/Time (W/min)	Area (mm^2)	T_{min} (°C)	T_{max} (°C)
Unmasked	20 /5	50 x 60	40	49.5
Unmasked	20 /10	53 x73	40	49.7
Unmasked	10 /5	24 x 38	40	43.29
Unmasked	10 /10	54 x 36	40	43.4
Slot area = 40 × 40 mm^2				
Masked	20 /5	27 x 35	40	43.15
Masked	20 /10	30 x 38	40	43.79
Masked	10 /5	5 x 12	40	40.26
Masked	10 /10	16 x 15	40	40.26
Slot area = 20 × 20 mm^2				
Masked	20 / 5	15 x 12	40	43.78
Masked	20 /10	15 x 21	40	44.07
Slot area = 10 × 10 mm^2				
Masked	20 / 5	2 x 2	40	40.81
Masked	20 /10	4 x 3	40	40.87

(a)

(b)

Fig. 10. Simulated masked near field. (a) Heat distribution at 5 min. (b) Heat distribution at 10 min at 20 W and mask slot dimension of 2 ×2 cm^2.

(a)

(b)
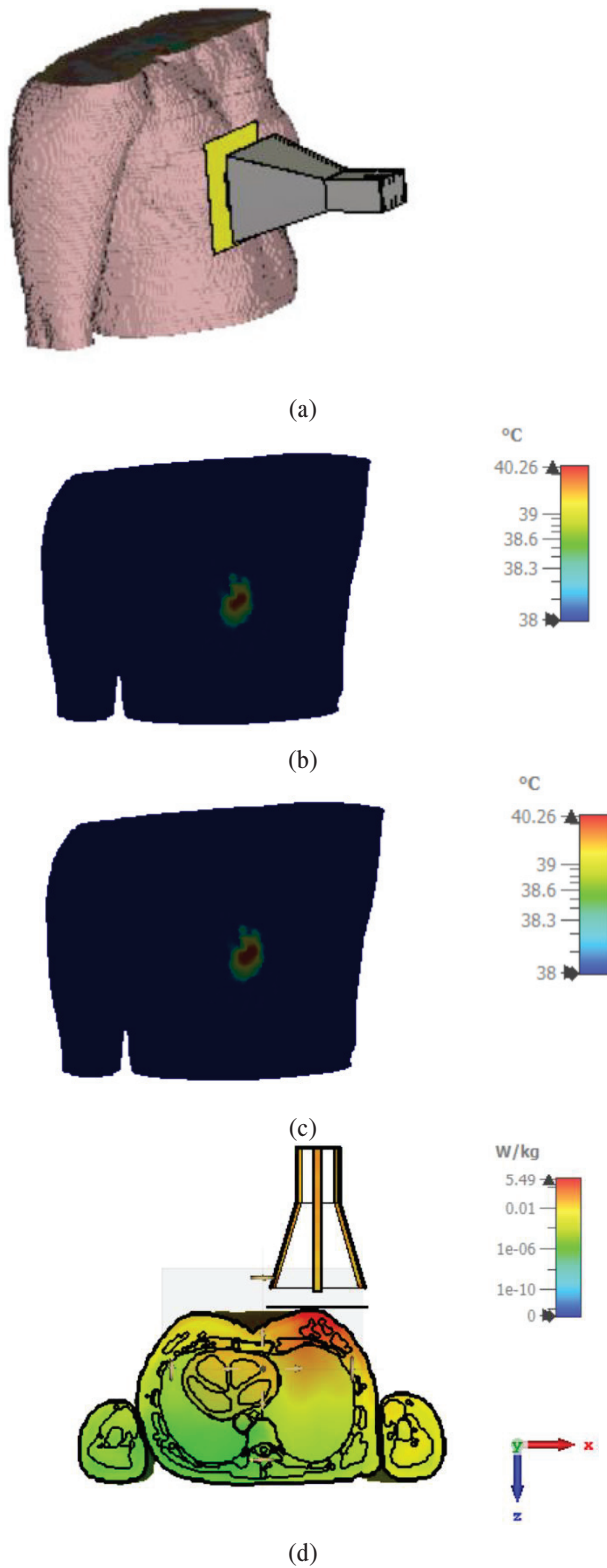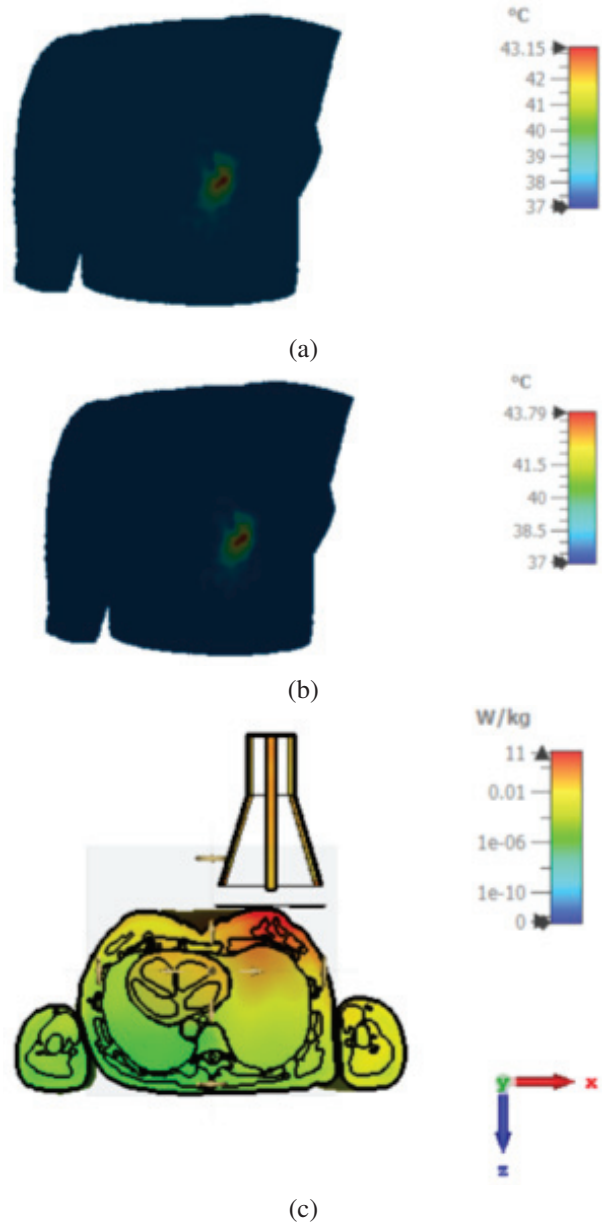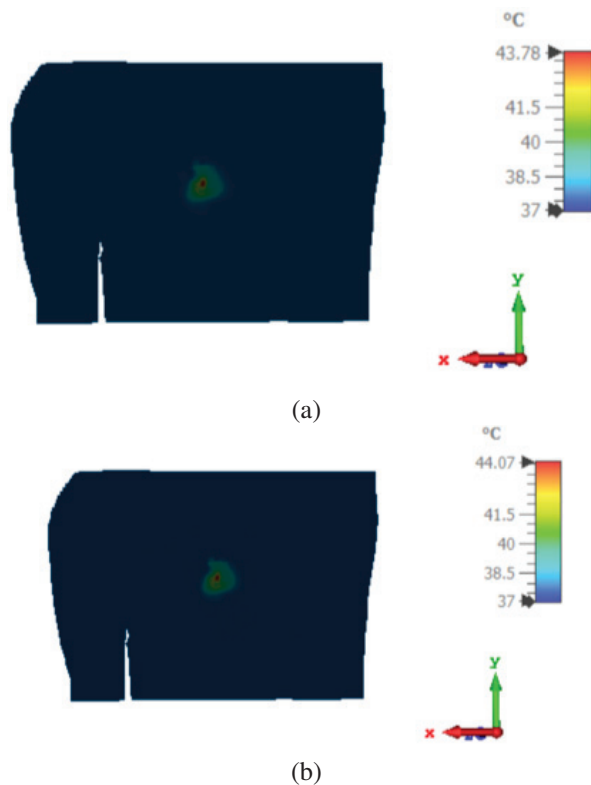
Fig. 11. Simulated masked near field. (a) Heat distribution at 5 min. (b) Heat distribution at 10 min at 20 W and mask slot dimension of 1×1 cm^2.

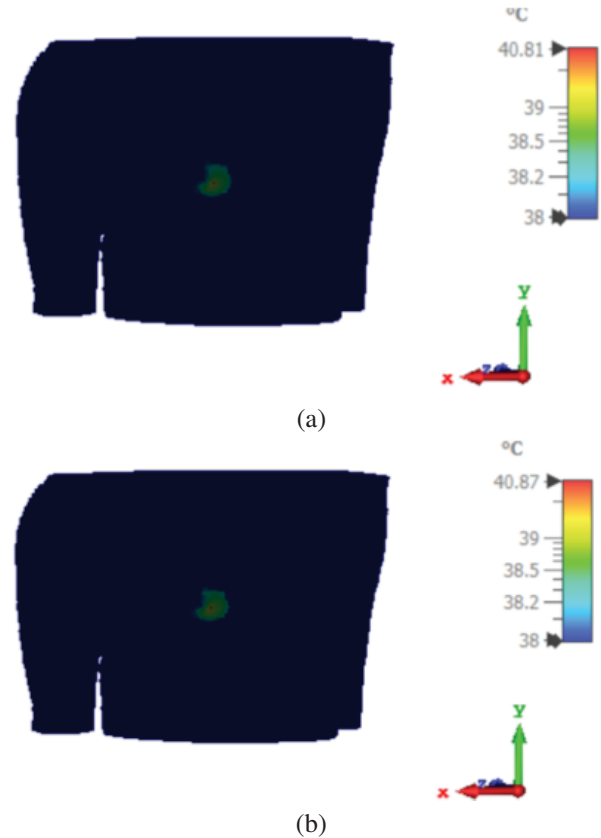the exposure time increases from 5 to 10 min, the heated area size reduction of 99.69 % is obtained. The highest SAR value decreases from 7.07 W/kg in the unmasked situation to 5.49 W/kg in the masked scenario, and from 14.1 W/kg in the unmasked scenario to 11 W/kg in the masked scenario when input power is 10 W and 20 W, respectively. The veiled situation cannot reach 49 °C, however temperatures between 40 °C and 43 °C are still sufficient for hyperthermia treatment.

III. CONCLUSION

A masked near-field localized thermal therapy method was introduced. A 4.74 GHz pyramidal horn antenna was used as a hyperthermia system applicator. The antenna irradiated a breast phantom for 5 and 10 minutes with input power of 10 and 20 W. Thermal and SAR distributions were investigated. Considering the masked scenario with input power of 20 W and exposure time of 5 min and 10 min, a heated area size reduction of 99.87 % and 99.69 % were obtained, respectively. Moving from an unmasked to a masked scenario, the maximum SAR value was reduced from 7.07 W/kg, to 5.49 W/kg with input power of 10 W and from 14.1 W/kg to 11 W/kg, with an input power of 20 W. The masked scenario elevated the temperature to 43 °C in a very concentrated area and that is very promising in hyperthermia therapy applications.

REFERENCES

[1] B. Uysal, "Hyperthermia and breast cancer: A short review," *Journal of Radiology and Oncology*, vol. 1, no. 3, pp. 079-082, Oct. 2017.

[2] N. Nizam-Uddin, W. Alkadri, W. A. Malik, I. Elshafiey, and A. F. Sheta, "Towards wideband hyperthermia treatment system," *Applied Computational Electromagnetics Society (ACES) Journal*, vol. 9, no. 32, pp. 769-780, Jan. 2017.

[3] P. Faridi, T. B. Shrestha, M. Pyle, M. T. Basel, S. H. Bossmann, P. Prakash, and B. Natarajan, "Temperature estimation for MR-guided microwave hyperthermia using block-based compressed sensing," *42nd Annual International Conference of the IEEE Engineering in Medicine & Biology Society (EMBC)*, Montreal, QC, Canada, pp. 5057-5060, July 2020.

[4] O. Debnath, K. Saito, K. Ito, and M. Uesaka, "Breast cancer treatment by combining microwave hyperthermia and radiation brachytherapy," *International Symposium on Antennas and Propagation (ISAP)*, Okinawa, Japan, pp. 472-473, Oct. 2016.

[5] H. P. Kok and J. Crezee, "Progress and future directions in hyperthermia treatment planning," *2017 First IEEE MTT-S International Microwave Bio Conference (IMBIOC)*, Gothenburg, Sweden, pp. 1-4, May 2017.

[6] M. Abdel-Haleem, T. Abouelnaga, M. Abo-Zahhad, and S. Ahmed, "Enhancing microwave breast cancer hyperthermia therapy efficiency utilizing fat grafting with horn antenna," *International Journal of RF and Microwave Computer-Aided Engineering*, vol. 31, no. 6, Apr. 2021.

[7] M. Abdel-Haleem, T. Abouelnaga, M. Abo-Zahhad, and S. Ahmed, "A preclinical system for enhancing the efficiency of microwave breast cancer hyperthermia therapy using dielectric matched layer and convex lenses," *Progress in Electromagnetics Research C*, vol. 109, pp. 153-168, Jan. 2021.

[8] P. Nguyen, A. Abbosh, and S. Crozier, "Three-dimensional microwave hyperthermia for breast cancer treatment in a realistic environment using particle swarm optimization," *IEEE Transactions on Biomedical Engineering,* vol. 64, no. 6, pp. 1335-1344, June 2017.

[9] E. Lekka, D. Konstantinos, and A. George, "Phased array design for near field focused hyperthermia based on reciprocity theorem," *International Workshop on Antenna Technology: Small Antennas, Innovative Structures, and Applications (IWAT)*, Athens, Greece, pp. 277-280, Mar. 2017.

[10] H. Xiaoping, W. Geyi, and S. Wang, "Optimal design of focused arrays for microwave-induced hyperthermia," *IET Microwaves, Antenna and Propagation*, vol. 9, no. 14, pp. 1605-1611, Nov. 2015.

[11] S. Singh and S. P. Singh, "Investigation on improved water-loaded diagonal horn applicators for hyperthermia," *Journal of Electromagnetic Waves and Applications,* vol. 30, no. 14, pp. 1836-1857, Aug. 2016

[12] A. Dadzadi and R. Faraji-Dana, "Breast cancer hemispheric shaped hyperthermia system designed with compact conformal planar antenna array," *IEEE Asia-Pacific Microwave Conference (APMC)*, Singapore, pp. 1107-1109, Dec. 2019.

[13] M. Tayel, T. Abouelnaga, and A. Elnagar, "Pencil beam grid antenna array for hyperthermia breast cancer treatment system," *Circuits and Systems*, vol. 8, no. 5, pp. 122-133, May 2017.

[14] M. Tayel, T. G. Abouelnaga, and A. Elnagar, "Dielectric loaded Yagi fed dual band pyramidal horn antenna for breast hyperthermia treatment," *5th International Conference on Electrical and Electronic Engineering (ICEEE)*, Istanbul, Turkey, pp. 323-328, May 2018.

[15] P. Nepa and A. Buffi, "Near-field-focused microwave antennas: Near-field shaping and implementation," *IEEE Antennas and Propagation Magazine*, vol. 59, no. 3, pp. 42-53, June 2017.

[16] S. Suseela and P. Wahid, "Breast cancer hyperthermia using a grid array applicator," *Southeast Conference*, Raleigh, NC, USA, pp. 1-4, Mar. 2020.

[17] M. Tayel, T. G. Abouelnaga, and A. Desouky, "UWB high gain antenna array for SAR based breast cancer detection system," *5th IEEE International Conference on Electrical and Electronic Engineering (ICEEE)*, Istanbul, Turkey, pp. 311-316, 2018.

Tamer Gaber Abouelnaga was born in November 1976. He received the B.Sc. (Hons.) degree in Electronics Engineering in 1999 from Menofiya University, Egypt. He gained the M.Sc. and Ph.D. degrees in 2007 and 2012, respectively, in Electronics and Communications from Ain Shams University. From 2012 to 2017 he worked as a Researcher, and since 2018 has been an Associate Professor in the Microstrip Circuits Department, Electronics Research Institute, Egypt. From 2018 to 2022 he was Students Affairs and Environmental Development Vice Dean at the Higher Institute of Engineering and Technology, Kafr Elsheikh City. He is currently Students Affairs Vice Dean at the Faculty of Industry and Energy Technology at New Cairo Technological University. He has published 47 papers, 33

papers in peer-refereed journals, and 14 papers in international conferences regarding antennas, couplers, filters, and dividers for different microwave applications. His current interest is in microwave usage in biological applications.

Maha R. Abdel-Haleem was born in 1989. She received the B.S. degree in Electrical Engineering from Benha University, Egypt, in 2011, and the M.S. degree from the School of Electronics, Communications, and Computer Engineering, Egypt-Japan University of Science and Technology, Alexandria, Egypt, in 2016. She is currently an Assistant Professor in the Faculty of Engineering, Banha University. Her research interests include wave propagation and biomedical engineering.

Sectional Modular Technology for Reducing Detent Force of Linear Unit in Linear-rotary Flux-switching Permanent-magnet Generator for Wind-wave Combined Energy Conversion

Guozhen Zhang[1], Rui Nie[1], Jikai Si[1], Xiaohui Feng[2], and Changli Wang[3]

[1]School of Electrical and Information Engineering
Zhengzhou University, Zhengzhou, 450001, China
zhanggz18312@126.com, nierui@zzu.edu.cn, sijikai527@126.com

[2]School of Mechanical and Electrical Engineering
North China Institute of Science and Technology, Beijing, 101601, China
fengxh@ncist.edu.cn

[3]School of Computer Science
North China Institute of Science and Technology, Beijing, 065201, China
wangcl@ncist.edu.cn

Abstract – A linear-rotary flux-switching permanent magnet (FSPM) generator (LRFSPMG) is a potential candidate for a wind-wave combined energy conversion (WWCEC) system. The linear unit of the LRFSPMG is a tubular FSPM linear generator (TFSPMLG), which like other permanent magnet linear generators, has an inherent detent force problem. To alleviate this problem, a sectional modular technology scheme is investigated to reduce the detent force of the TFSPMLG. Firstly, the structure is briefly introduced and the detent force analyzed. Secondly, the sectional modular TFSPMLGs are presented and their feasibility verified with respect to the stator of the TFSPMLG being split into two and three sections, forming Modulars I and II, respectively. After that, the detent force suppression principle, and the effects that the sectional modular structures exert on the detent force are analyzed. According to the analysis results, two methods are presented to suppress the detent force: one is to suppress the magnetic coupling effect; the other is to reduce the remaining harmonics. Finally, the three TFSPMLGs, including the initial TFSPMLG, Modular I, and Modular II, are comparatively analyzed by finite-element analysis (FEA). The results show that both the detent forces are greatly reduced without sacrificing the back electromotive force (EMF) and average electromagnetic force, thereby proving the effectiveness of the TFSPMLG with a sectional modular structure.

Index Terms – detent force, flux-switching, sectional modular technology, tubular permanent-magnet linear generator.

I. INTRODUCTION

Wind energy and wave energy are significant sources of renewable energy and have attracted considerable attention owing to the advantages of high energy density, environmental protection, and wide distribution with large reserves [1, 2]. More recently, wind-wave combined energy conversion (WWCEC) systems employing a linear-rotary generator have emerged and developed rapidly since they can harvest both these energy sources to generate electrical energy simultaneously through a single generator, thus improving the efficiency and economy of such systems [3].

As one of the core components of WWCEC systems, linear-rotary generators are expected to provide high power and efficiency with high operational reliability in harsh offshore environments [4]. Since flux-switching permanent magnet (FSPM) generators inherit the merits of conventional permanent magnet (PM) generators (high power) and switched reluctance generators (robust structure) [5], the FSPM generator is considered to be a promising candidate for WWCEC systems. Accordingly, a linear-rotary FSPM generator, comprising linear and rotary units, is proposed for WWCEC systems [6, 7]. However, the linear unit, which is a tubular FSPM linear generator, suffers from the detent force caused by slot effect and end effect, thereby leading to the deterioration of the electrical generation capability. Hence, reducing the detent force is a key aim in order to improve the performance of the TFSPMLG.

Existing methods indicate that the problem of detent force can be largely resolved by reducing the cogging

force, e.g., by skewing the pole or slot, asymmetrical distribution of stator teeth [8, 9], optimizing the tooth pitch, or optimizing the shape of PMs [10, 11]. However, these methods are unsuited to a TFSPMLG since the end force has a greater impact on the FSPM machine [12]. Another approach involves suppressing the end effect by methods such as adding assistant teeth or auxiliary poles, adjusting the width and length of end teeth, and optimizing the slot structure [13, 14]. These measures can improve the flux distribution around the ends to suppress the end effect, thus effectively reducing the detent force. Meanwhile, compensation windings are also widely employed to reduce the detent force by injecting proper current into compensation coils and combining control strategy [15, 16]. However, this measure generally needs to be combined with other measures to achieve better results.

Recently, a modular technology scheme was put forward and implemented in various machines to reduce the detent force [17–21]. In [17], each slot of the machine was dispersed, and the detent force was greatly reduced by the mutual influence between the single primary units. In [18, 19], the primary iron was divided into two sections to form a modular structure. In that situation, the fundamental and odd-order harmonics components in the detent force can be eliminated. At the same time, the primary component with a three-section structure was also adopted, in which only the third and its multiple harmonics remained in detent force, and other harmonics components were offset [20, 21]. Moreover, this method does not add to the manufacturing complexity. The above modular technology scheme therefore suggests a new approach to reducing detent force, and in terms of the existing research findings, can achieve better results in PM linear machines. As a type of linear machine, whether the modular technology scheme works for a TFSPMLG needs further investigation.

Accordingly, this paper presents a sectional modular TFSPMLG approach to reducing detent force. The paper is organized as follows. In Section II, the structure of the TFSPMLG is briefly introduced and the detent force is analyzed. Then, the sectional modular TFSPMLG is presented in terms of its feasibility, the principle of detent force suppression, and analysis of the effects that the sectional modular structures exert on the detent force. In Section III, detent force minimization methods are conducted based on the analysis results. The three TFSPMLGs, including the initial TFSPMLG, Modular I, and Modular II, are analyzed comparatively by two-dimensional finite-element analysis (2D-FEA) in Section IV. Finally, the conclusions are summarized in Section V.

II. INITIAL AND SECTIONAL MODULAR STRUCTURE OF TFSPMLG AND THE DETENT FORCE

A. Initial structure and detent force of the TFSPMLG

Figure 1 (a) show the structure of the LRFSPMG, which is composed of a linear unit and a rotary unit. Ignoring the influence between the linear unit and rotary unit, the detent force of the LRFSPMG can be regarded as that of the linear unit. In the interest of simplicity analysis, the following research focuses on the linear unit in order to investigate the detent force of the LRFSPMG. It can be observed from Fig. 1 (b) that, for the linear unit, it is a 12s/14p TFSPMLG. Both PMs and armature windings are placed in the stator, and the mover only consists of the iron core. PMs with opposite magnetization are sandwiched between dumbbell-shaped laminated segments, which are wound by toroidal-shaped coils. Since the magnetic circuit is imbalanced due to the end effect existing, the end teeth are adopted at the end sides of the stator. The major parameters of the TF-SPMLG are listed in Table 1.
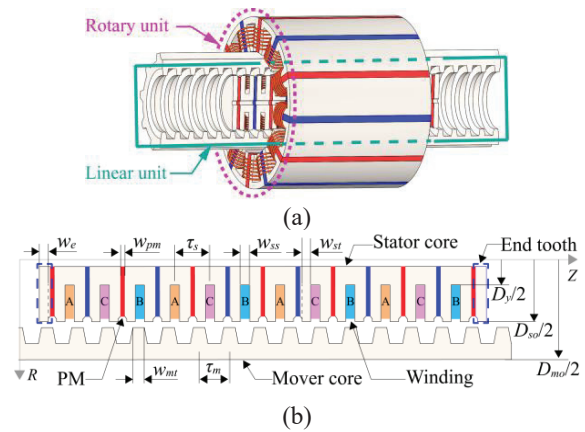
Fig. 1. Structure of generator: (a) LRFSPMG; (b) two-dimensional structure of linear unit in *RZ* coordinate system.

The default mover velocity is 1 m/s and the default load is 10 Ω in this simulation. The detent force and electromagnetic force of the TFSPMLG are simulated by 2D-FEA, as shown in Fig. 2. The variation trend of the electromagnetic force is consistent with the detent force. Meanwhile, in a fluctuating period of one mover pole pitch τ_m, the fluctuation amplitude of the electromagnetic force is close to that of the detent force, which indicates that the fluctuation of the electromagnetic force is mainly affected by the detent force. Thus,

Table 1: Parameter of the TFSPMLG

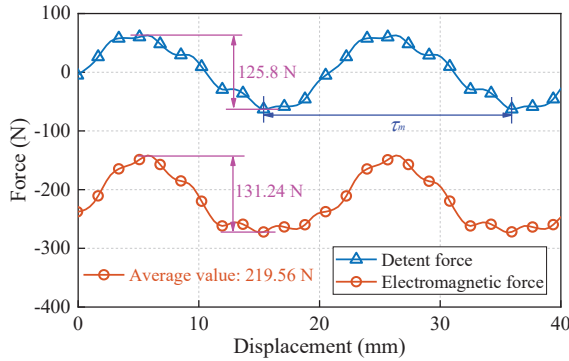| Item	Symbol	Value
Outer diameter of mover	D_{mo}	118 mm
Outer diameter of stator	D_{so}	73 mm
Diameter of stator yoke	D_y	25 mm
Stator pole pitch	τ_s	24 mm
Mover pole pitch	τ_m	$\tau_s*12/14$
Number of slots	N_s	12
Number of poles	N_p	14
Width of stator teeth	w_{st}	6 mm
Width of slot	w_{ss}	6 mm
Width of PM	w_{pm}	4 mm
Width of mover teeth	w_{mt}	6 mm
Width of end teeth	w_e	6 mm

Fig. 2. Detent force and electromagnetic force of the TF-SPMLG.

the electromagnetic force ripple can be effectively suppressed by reducing the detent force.

B. Sectional modular structure of the TFSPMLG

For the purpose of suppressing the detent force, this paper proposes the adoption of a sectional modular technology structure. If the coils in each section are the same, the stator can be divided into two, three, four, six, and twelve sections. However, too many sections may lead to the waste of the stator volume, which results in reduced force density [20]. Hence, this study only considers the case where two or three sections are selected.

Based on the above description, the TFSPMLG stator can adopt either a two-section structure, three-section structure, or both, in which the stator is split into two sections and three sections, named Modular I and Modular II respectively, as shown in Fig. 3. The flux barrier, which can be made of air or nonmagnetic material, is set between two sectional stators. Each sectional stator in Modular I/II is the same and combines with the mover forming a unit generator. According to the design principle of mutual offset detent force between generator units [22], the TFSPMLG with the two-section and three-section structures needs to satisfy equations (1) and (2),

respectively:

$$L_{\mathrm{I}-s}+L_{\mathrm{I}-fb}=\frac{2k\pm1}{2}\tau_m, \tag{1}$$

$$L_{\mathrm{II}-s}+L_{\mathrm{II}-fb}=\frac{3k\pm1}{3}\tau_m, \tag{2}$$

where L_{I-s} and L_{II-s} are the length of the sectional stator, L_{I-fb} and L_{II-fb} are the length of the flux barrier for the Modular I and II, respectively, τ_m is the mover pole pitch, and k is a positive integer.

However, irrespective of which structure scheme is selected, the sectional modular TFSPMLG, while meeting the offset of detent force, should also meet the design principle requirements of the complementary structure. To verify the feasibility of the sectional modular technology scheme, the design principle of the sectional modular TFSPML is analyzed with two-section and three-section structures.

For the non-modular FSPM linear machine, the complementary structure of the windings requires satisfying two conditions [23]. Firstly, the relative distance λ_1 between the two adjacent coils of one phase should satisfy:

$$\lambda_1=\left(k\pm1/2\right)\tau_m. \tag{3}$$

Secondly, the displacement λ_2 between the two coils of the adjacent two phases should satisfy:

$$\lambda_2=\left(k\pm1/3\right)\tau_m \ \ \text{or} \ \ \lambda_2=\left(k\pm1/6\right)\tau_m. \tag{4}$$

Therefore, under the condition that the complementary winding characteristics are met, the spacer coils distance λ of one phase should satisfy the following relationships:

$$\lambda=k\tau_m. \tag{5}$$

Meanwhile, if the spacer coils are wound reversely or the magnetization directions of PMs on both sides of them are different, the electrical angle difference between spacer coils of one phase is 180°, i.e., the distance difference being $\tau_m/2$. Consequently, the preceding analysis indicates that the relative distance λ between spacer coils of one phase can be expressed as:

$$\lambda=j\tau_m\pm\frac{m}{2}\tau_m, \tag{6}$$

where j and m are positive integers.

For the sectional modular TFSPMLG shown in Fig. 3, the lengths of the sectional stator and flux barrier have the following relationship with λ:

$$L_{i-s}+L_{i-fb}+n\tau_s=\lambda, \tag{7}$$

where L_{i-s} and L_{i-fb} are the length of the sectional stator and flux barrier, respectively, i is I or II, which indicates Modular I or II, τ_s is the stator pole pitch, and n is a positive integer.

Substituting equation (6) into equation (7) and combining with pole pitch ratio τ_s/τ_m of 14/12, the sum of the sectional stator length and flux barrier length can be expressed as:

$$L_{i-s}+L_{i-fb}=j\tau_m\pm\frac{m}{2}\tau_m\pm\frac{n}{6}\tau_m. \tag{8}$$
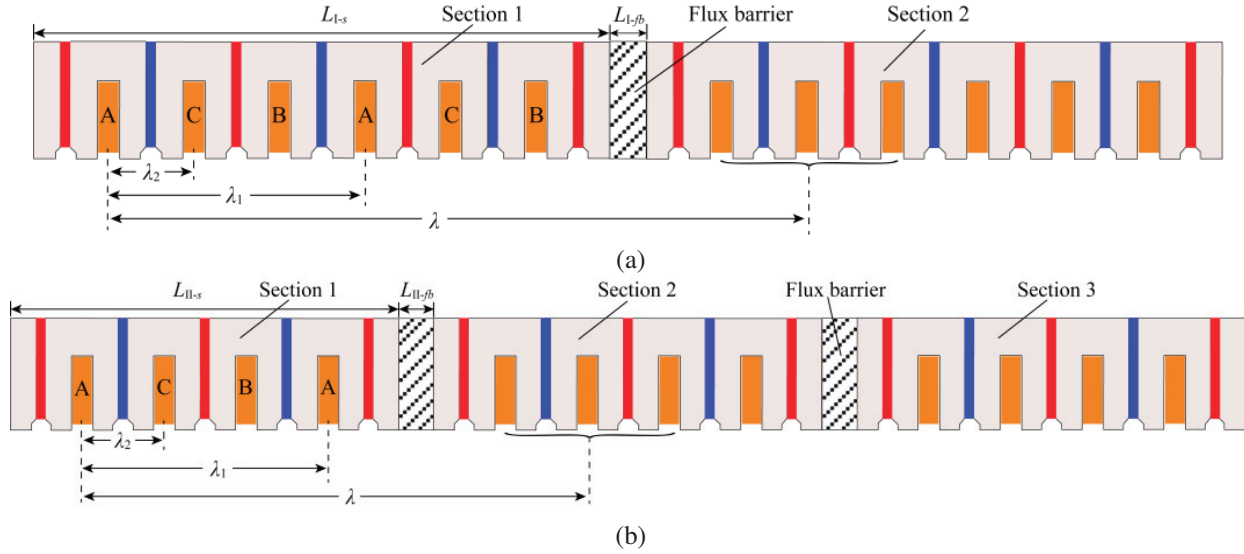
Fig. 3. Sectional modular structure of the TFSPMLG: (a) Modular I; (b) Modular II.

Comparing equations (1), (2), and (8), it can be found that (1) and (2) are special forms of (8); i.e., *n* is 0 and *m* is 0 ($n = 2, 8, 14, \ldots$), separately. In other words, while satisfying equations (1) and (2), the complementary structure of the sectional modular TFSPMLG is also satisfied, which verifies the feasibility of the TFSPMLG with two-section and three-section structures. Hence, for sectional modular TFSPMLG, the two-section structure and three-section structure can both be applied. Accordingly, both sectional modular structures are investigated in this paper.

C. Theoretical analysis of detent force of the sectional modular TFSPMLG

For the sectional modular TFSPMLG, the unit detent force of each unit generator can be expressed by Fourier series expansion as follows:

$$f_{\text{detent}\_i}(x) = \sum_{n=1}^{\infty} F_{dn-i} \sin\left(\frac{2n\pi}{\tau_m}x + \theta_{dn-i}\right), \quad (9)$$

where F_{dn-i} and θ_{dn-i} are the amplitude and phase of the *n*th component respectively, *i* is I or II, and *x* is the mover position.

Ignoring the magnetic coupling effect between sectional stators, each unit generator is independent. In that case, the amplitudes of the unit detent force are the same, but their phases are different. Considering the relative distance between the unit generators, the whole detent forces of the sectional modular TFSPMLGs can be expressed as:

$$f_{w\_I} = f_{\text{detent}\_I}(x) + f_{\text{detent}\_I}(x + L_{I-s} + L_{I-fb}), \quad (10)$$

$$\begin{aligned} f_{w\_II} = &f_{\text{detent}\_II}(x) + f_{\text{detent}\_II}(x + L_{II-s} + L_{II-fb}) \\ &+ f_{\text{detent}\_II}(x + 2L_{II-s} + 2L_{II-fb}) \end{aligned}, \quad (11)$$

where f_{w_I} and f_{w_II} are the whole detent force of Modular I and II, respectively.

According to the design principle of mutual offset detent force in Section II-B, the whole detent force can be calculated as:

$$f_{w\_I} = \sum_{n=2,4,6,\ldots}^{\infty} 2F_{dn-I} \sin\left(\frac{2n\pi}{\tau_m}x + \theta_{dn-I}\right), \quad (12)$$

$$f_{w\_II} = \sum_{n=3,6,9,\ldots}^{\infty} 3F_{dn-II} \sin\left(\frac{2n\pi}{\tau_m}x + \theta_{dn-II}\right). \quad (13)$$

According to equations (12) and (13), after setting the sectional modular structure, the fundamental and some higher harmonics in unit detent force can be offset. For Modular I, the whole detent force consists of the remaining second and its multiple harmonics, while the whole detent force is composed of the remaining third and its multiple harmonics for Modular II.

D. Detent force of the sectional modular TFSPMLG

In the initial design, the sectional stator lengths L_{I-s} and L_{II-s} satisfy:

$$L_{I-s} = 63\tau_m/8 \quad L_{II-s} = 133\tau_m/24. \quad (14)$$

By substituting equation (14) into equations (1) and (2), the flux barrier lengths L_{I-fb} and L_{II-fb} can be equal to $5\tau_m/8$ or $13\tau_m/8$ and $\tau_m/8$, $19\tau_m/24$, or $9\tau_m/8$, respectively.

Figure 4 show the whole detent forces of Modular I and II under the different lengths of the flux barrier. For Modular I and II, both the whole detent forces are decreased as the flux barrier lengths are increased, which
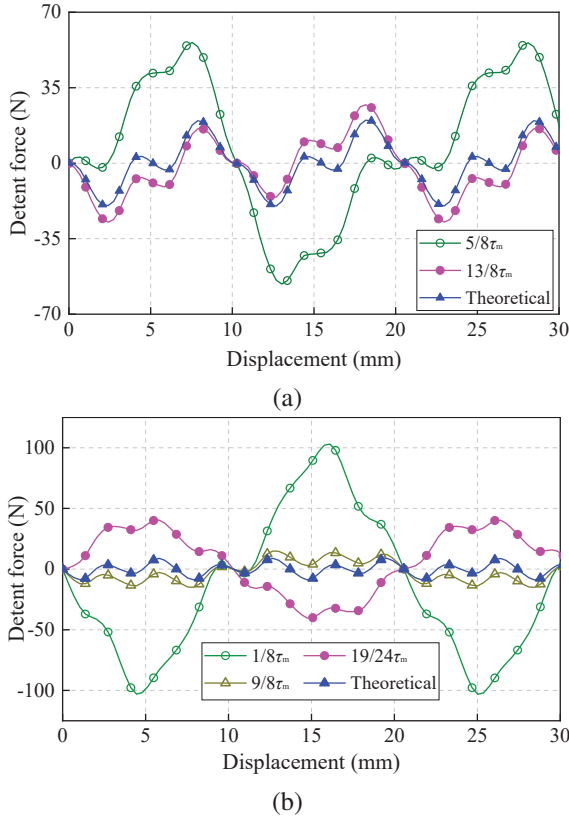
(a)

(b)

Fig. 4. Whole detent force: (a) Modular I; (b) Modular II.

indicates that the magnetic coupling effect exists between unit generators and exerts a negative effect on the whole detent force. Hence, the flux barrier length should reach a certain length to reduce the influence of the magnetic coupling effect. When the flux barrier length of Modular I is $13\tau_m/8$ and that of Modular II is $9\tau_m/8$, the whole detent force is 27.39 N and 15.01 N, which is 35.86% and 67.71% higher than the theoretical value of 20.16N and 8.95 N, respectively. This means that the magnetic coupling effect needs to be further suppressed by other methods under a certain flux barrier length.

Moreover, the Fourier analysis results of unit detent force, as shown in Fig. 5, indicate that the second and its
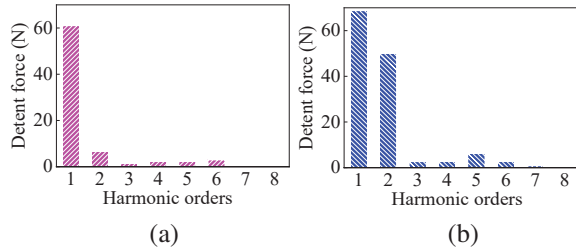

(a)   (b)

Fig. 5. Harmonics distribution of unit detent force: (a) Modular I; (b) Modular II.

multiple components for Modular I are relatively large, and the third and its multiple components of Modular II are relatively little. So, according to the relationship between the whole detent force and the unit detent force in Section II-C, the theoretical whole detent force of the Modular I is relatively large, and that of the Modular II is relatively little, which are 20.16 N and 8.95 N, respectively. Hence, the actual whole detent force of Modular I is greater than that of Modular II, although the magnetic barrier length of Modular I is larger than that of Modular II, for example, when the magnetic barrier length is $13\tau_m/8$ and $9\tau_m/8$, respectively. Consequently, the whole detent force can be diminished by the reduction of the remaining harmonics in the unit detent force.

From the aforementioned analysis, it can be found that the whole detent force results from the magnetic coupling effect and remaining harmonics in the unit detent force. If both these contributing elements decrease, the whole detent force will decrease, and this can guide the optimization needed to reduce the detent force.

III. DETENT FORCE MINIMIZATION

In this section, the whole detent force is further reduced. Based on the analysis above, the whole detent forces of Modular I and Modular II are large, which are due not only to the magnetic coupling effect between unit generators but also to the remaining harmonic components in the unit detent force. Therefore, the whole detent force can be further reduced by suppressing the magnetic coupling effect, as well as reducing the remaining harmonics components.

A. Suppression of the magnetic coupling effect

The magnetic coupling effect exists between unit generators. Set Modular I with a flux barrier length of $13\tau_m/8$ as an example with which to analyze the magnetic coupling effect. The magnetic flux line distribution of the flux barrier is shown in Fig. 6 (a). The magnetic flux lines indicated by blue ellipses pass through the flux barrier or mover and connect the two adjacent unit generators, resulting in magnetic coupling. This is because the PMs on both sides of the flux barrier are magnetized in the same direction, and thus the equivalent magnetomotive force between two ends increases, which leads to the enhancement of the connection between adjacent unit generators. Hence, these magnetic flux lines can be suppressed by changing the magnetization direction of one of the PMs. Figure 6 (b) shows the magnetic flux line after changing the magnetization direction, i.e., reversed magnetization. The magnetic flux lines in the flux barrier are greatly suppressed, which indicates that the magnetic coupling effect is weakened.

Table 2 lists the comparison of the whole detent force of Modular I under two different magnetization directions. Compared with the whole detent force with
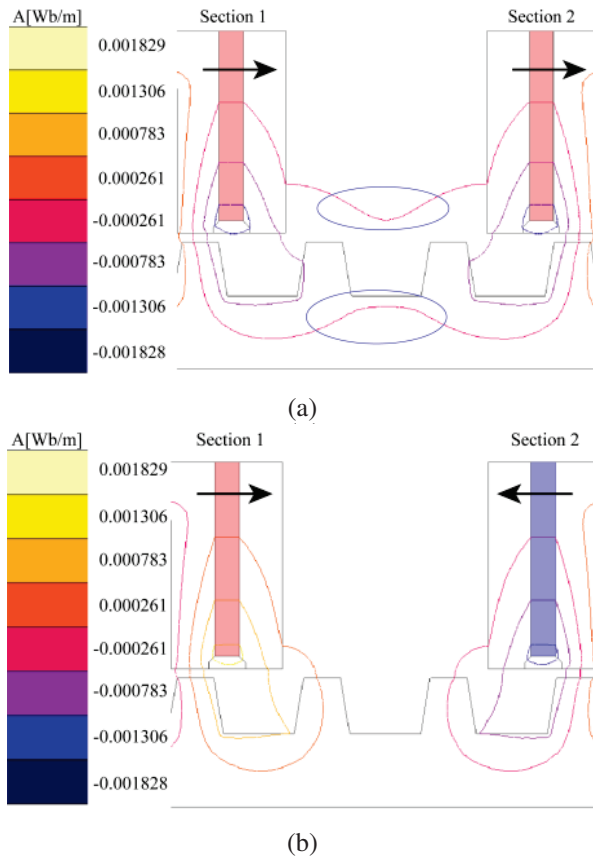
(a)

(b)

Fig. 6. Magnetic flux line distribution: (a) same magnetization; (b) reversed magnetization.

Table 2: Comparison of the whole detent force

Flux Barrier Length	Same Magnetization	Reversed Magnetization	Theoretical
$5/8\tau_s$	56.05 N	31.35 N	20.16N
$13/8\tau_s$	27.39 N	23.60 N	

the same magnetization, when the flux barrier length is $5\tau_m/8$ and $13\tau_m/8$, the whole detent force with the reversed magnetization declines by 44.07 and 13.84% respectively, but it is still greater than the theoretical value. It proves that the above method can suppress the magnetic coupling effect to a certain extent.

B. Reduction of remaining harmonics

Without considering the magnetic coupling effect, the whole detent force is the superposition of the remaining harmonics in the unit detent force. Thus, the whole detent force can be reduced through the diminishment of the remaining harmonics, which are the second and its multiple harmonics and the third and its multiple harmonics for Modular I and Modular II, respectively. Ac-

cording to the aforementioned literature, the end teeth width w_e and mover teeth coefficient k_{st} ($k_{st} = w_{mt}/w_{st}$: the ratio of the mover teeth width w_{mt} to the stator teeth width w_{st}) have a great influence on the detent force [23, 24]. Therefore, the above two parameters should be adjusted to reduce the remaining harmonics in the unit detent force.

Figure 7 show the whole detent force of Modular I calculated by equation (12), and that of Modular II calculated by equation (13). For Modular I, when the end teeth width and mover teeth coefficient are 9 mm and 1.3 respectively – indicated by a magenta dot in Fig. 7 (a) – the minimum amplitude of the whole detent force is 2.46N. The corresponding flux barrier length can then be determined, although theoretically there are countless values for the flux barrier length because of k in equation (1) with countless values. According to equation (1), the flux barrier length can be $\tau_m/3$, $4\tau_m/3$, or $7\tau_m/3$ ($k = 8$, 9, and 10), etc. Considering a certain flux barrier length to suppress the magnetic coupling effect and the stator volume limitation, the flux barrier length is selected as $4\tau_m/3$ ($k=9$). For Modular II, under the same mover teeth
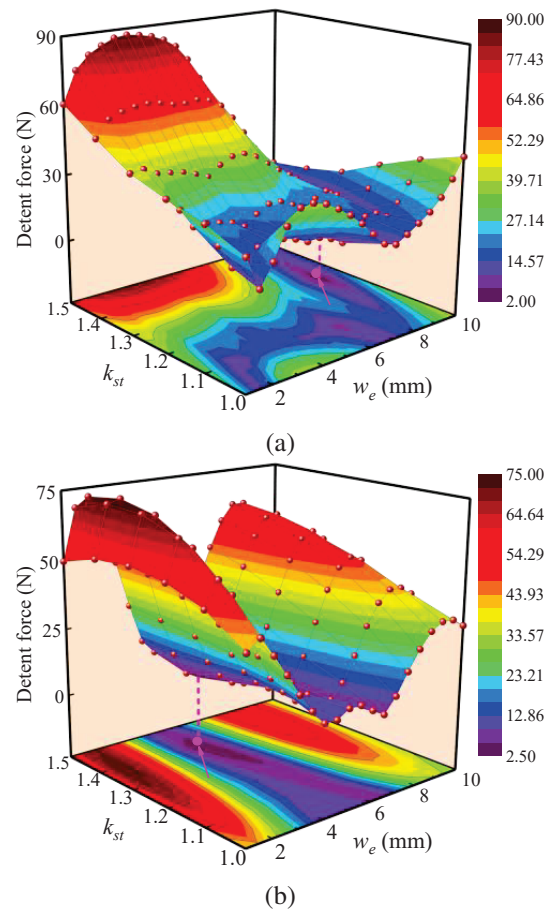

(a)

(b)

Fig. 7. Whole detent force: (a) Modular I; (b) Modular II.

coefficient, the whole detent force initially decreases and then rises with the increase of the end teeth width. Within the end teeth width range from 4 mm to 6 mm, the whole detent force is relatively small, in which the minimum value is 2.65N when the end teeth width and mover teeth coefficient are 5 mm and 1.4 respectively, as shown by the magenta dot in Fig. 7 (b). Then, according to the determined end teeth width and combined with equation (2), the flux barrier length of Modular II is equal to $2\tau_m/9$, $8\tau_m/9$, $11\tau_m/9$, or $17\tau_m/9$ ($k = 6$ and 7), and so on. Finally, under comprehensive consideration, the flux barrier length is determined to be $11\tau_m/9$, with $k = 7$ and minus sign in equation (2).

IV. COMPARATIVE ANALYSIS

In this section, the three TFSPMLGs, including the initial TFSPMLG, Modular I, and Modular II, are analyzed comparatively by 2D-FEA. Apart from the end teeth width and mover teeth coefficient, all other parameters are identical.

A. Winding arrangement of the sectional modular TFSPMLG

The winding arrangements need to be determined first. The electrical degrees α between two adjacent coil-EMF vectors can be calculated by [25]:

$$\alpha = \frac{360°}{N_s} N_p, \tag{15}$$

where N_s and N_p denote the number of stator slots and mover poles, respectively. In this paper, the α of the 12s/14p PMLSM is 60°, thus the phase sequences of the initial TFSPMLGs are A-C-B-A-C-B-A-C-B-A-C-B, as shown in Fig. 1 (b).

The coil connection in the sectional modular TF-SPMLG is different from the traditional one, due to the existence of the flux barrier. In Fig. 3, there are six and four coils in each section, and the phase sequences of the coils in Section 1 are A-C-B-A-C-B and A-C-B-A, respectively, which is the same as that of the corresponding part in the initial TFSPMLG. However, the coil connections of Sections 2 and 3 need to be adjusted to obtain symmetrical three-phase complementary windings.

For Modular I, the sum of the sectional stator and flux barrier length satisfies equation (7), which means that the relative positional difference between the first coil of Sections 1 and 2 is $\tau_m/2$, corresponding to an electrical angle of 180°. In addition, to weaken the magnetic coupling effect in Section III-A, the magnetization direction of the PMs is changed, which again results in the shift of the coil-EMF vector, with an electrical angle of 180°. Hence, the coil-EMF vector of the two sections is the same, and the phase sequence in Section 2 of Modular I is also A-C-B-A-C-B. The phase coil vector and the winding arrangement can be determined, as shown in

Figs. 8 and 10 (a), where coil X and X' in Fig. 8 represent opposite polarity.
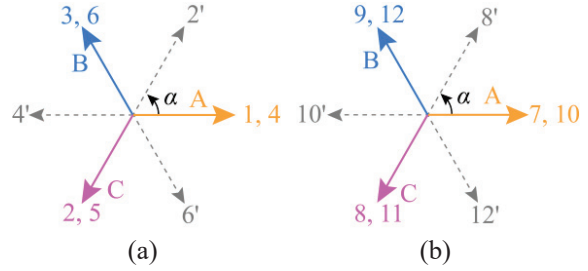

Fig. 8. Phase coil vector of Modular I: (a) Section 1; (b) Section 2.

For Modular II, the sum of the sectional stator and flux barrier length satisfies equation (2) with $k = 7$ and minus sign, which indicates that the first coil of Section 2 (the 5th one) lags behind that of Section 1 by the electrical angle of 120°. Likewise, the first coil of Section 3 (the 9th one) also lags 120° behind that of Section 2. Therefore, in consideration of the magnetization direction of the PMs, the coil-EMF vector of Sections 2 and 3 can be determined as shown in Figs. 9 (b) and (c), respectively. It can be found from Fig. 9 that coils No. 1, 4, 7', and 10, coils No. 2, 5', 8', and 11, and coils No. 3, 6', 9, and 12 all have the same electrical angles, and the phase difference between them is a 120° electrical angle. Meanwhile, coils No. 5, 6, 7, and 8 in Section 2 are with opposite polarity, which are marked with apostrophes, thus they are wound reversely. So, the coil connection in Sections 2 and 3 are Z-Y-X-Z and B-A-C-B, respectively, and Fig. 10 (b) shows its winding arrangement. The idealized arrangement of both the three-phase complementary windings confirm that the theoretical analysis in Section II-B is correct.
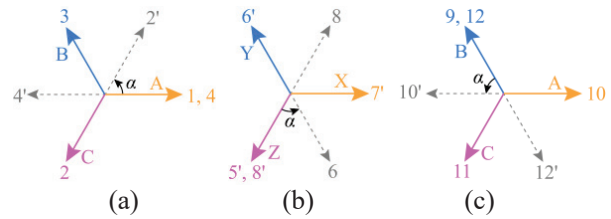

Fig. 9. Phase coil vector of Modular II: (a) Section 1; (b) Section 2; (c) Section 3.

B. Performances comparison

Figure 11 shows the detent force curves of three TFSPMLGs, of which the amplitudes are 63.09, 8.97, and 5.41 N, separately. Compared with the initial structure, the latter two structures are reduced by 85.78% and 91.42%, respectively. It is clear that for TFSPMLG, the
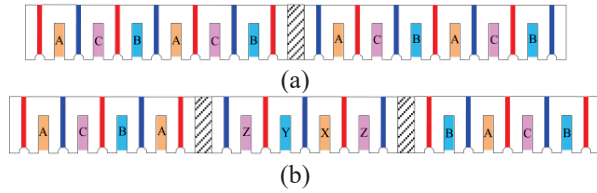
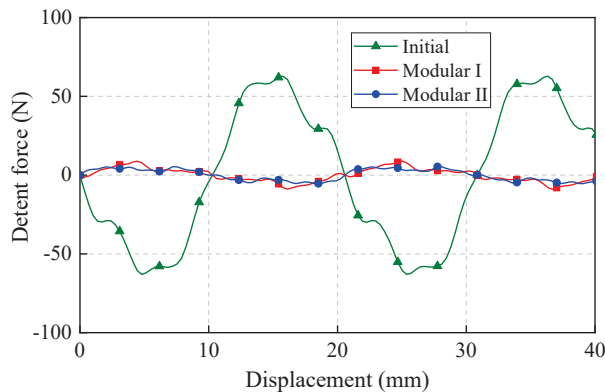Fig. 10. Winding arrangements: (a) Modular I; (b) Modular II.

Fig. 11. Detent force curves of three TFSPMLGs.

detent force can be significantly suppressed by adopting the sectional modular structure scheme. In addition, though both the actual detent forces of the Modulars I and II are larger than the theoretical detent forces with the amplitude 2.46 and 2.65 N due to the magnetic coupling effect, they are at an acceptable level. It proves the effectiveness of the sectional modular technology scheme for the TFSPMLG.

The back-EMF curves of three TFSPMLGs are shown in Fig. 12. It is worth noting that, for Modulars I and II, the back EMFs are the sum of that of each section. From the picture, the three back-EMF curves almost coincide, with very little difference between the three. The Fourier analysis results show that the fundamental components are 42.94, 43.17, and 44.29 V, with the total harmonic distortion (THD) 2.42%, 4.08%, and 1.47%, respectively. It can be found that, compared with the initial TFSPMLG, the THD of Modular I is increased greatly, whereas that of Modular II is decreased.

For Modular I, the main reasons can be described as follows: on the one hand, the winding arrangement of Section 2 is the same as that of Section 1 – see Fig. 10 (a) – with the result that the middle phase (phase C) is always in the middle of the sectional stator, and the side end phase (phases A and B) are always at the ends; on the other hand, the two-section structure is adopted to double the number of ends from 2 to 4; finally, the magnetic circuit of the three-phase windings is more unbalanced
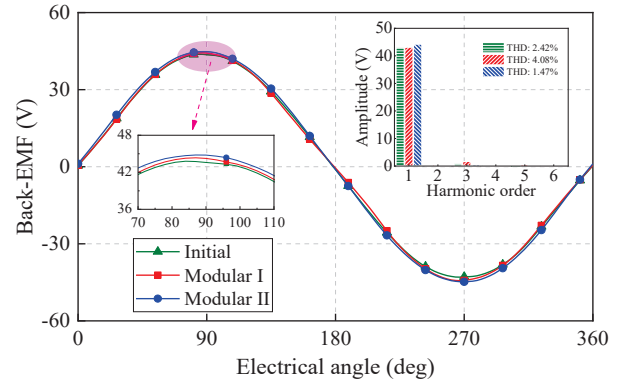

Fig. 12. Back EMF of three TFSPMLGs.

in such way that the corresponding THD increases. Different from that of Modular I, the arrangement of three-phase windings for Modular II, shown in Fig. 10 (b), is spatially symmetrical in that the numbers of each phase coil located on the side ends are the same, leading to the decrease of THD. Therefore, Modular II has better back-EMF characteristics.

The electromagnetic forces of three TFSPMLGs are compared in the resistive load with 10 Ω, as shown in Fig. 13. The average electromagnetic forces are 219.56, 220.85, and 230.01 N, and the electromagnetic force ripples, which is the ratio of the peak-to-peak value to the average value of electromagnetic force, are 59.78%, 30.21%, and 5.81%, respectively. Compared with the initial TFSPMLG, the electromagnetic force ripples of the sectional modular TFSPMLGs are suppressed due to the drop of detent force without sacrificing the average electromagnetic force.
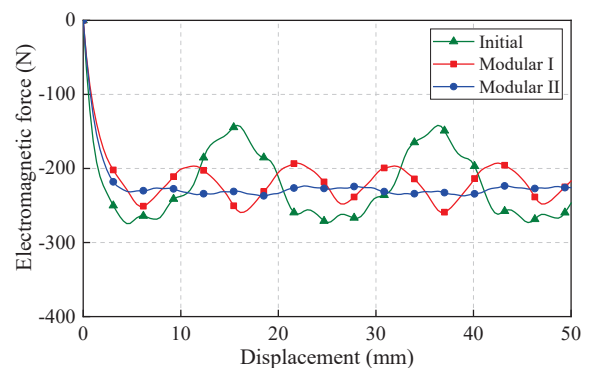

Fig. 13. Electromagnetic force curves of three TFSPMLGs.

However, according to the above analysis results for Modular I, the reduction degree of the electromagnetic force ripple is much lower than that of the detent force. This is because the force ripple is not only related to the detent force but is also associated with the harmonics in

Table 3: Comparison summary

Item	Initial	Modular I	Modular II
Amplitude of detent force (N)	63.09	8.97	5.41
Back-EMF (V)	42.94	43.17	44.29
THD (%)	2.42	4.08	1.47
Average electromagnetic force (N)	219.56	220.85	230.01
Electromagnetic force ripple (%)	59.78	30.21	5.81
Core losses (W)	5.95	6.85	7.23
Copper losses (W)	8.86	8.91	9.28
Efficiency (%)	93.43	93.07	93.04

the back EMF [18]. For Modular II, both the detent force and back-EMF THD are declined, thus the electromagnetic force ripple is small.

The efficiency η of three TFSPMLGs is calculated only considering the copper and core losses as:

$$\eta = \frac{P_e - P_c}{P_e + P_f} \times 100\%, \tag{16}$$

where η, P_e, P_c, and P_f are efficiency, electromagnetic power, copper loss, and core loss, respectively. The electromagnetic power is the product of the electromagnetic force and the mover velocity, and copper loss and core loss are computed by 2D-FEA, thus efficiency can be obtained.

Table 3 lists the comparison results of three TFSPMLGs. Based on the analysis of the detent force, back-EMF, and electromagnetic force, Modular II not only reduces the detent force most effectively, but also possesses the optimal back-EMF and electromagnetic force characteristics, with nearly the same efficiency. In addition, each sectional stator structure in Modular II is the same, thus the manufacture is simple. Hence, the proposed Modular II is a better choice for the TFSPMLG.

V. CONCLUSION

In this paper, sectional modular TFSPMLGs are proposed and investigated to reduce the detent force by adopting two-section and three-section structures, respectively. The sectional modular technology applies the particular harmonics in the unit detent force of each section to mutually offset, thereby reducing the whole detent force. First, the topology of TFSPMLG is described, and its detent force is analyzed. Then, the feasibility, detent force suppression principle, and the effects that the sectional modular structures exert on the detent force are investigated for the two sectional modular TFSPMLGs.

In addition, to suppress the magnetic coupling effect and reduce the remaining harmonics, two minimiza-

tion methods are presented. Finally, electromagnetic performance comparisons between the initial TFSPMLG, Modular I, and Modular II are conducted based on 2D-FEA with respect to detent force, EMF, and electromagnetic force. The results show that the sectional modular technology structure is proved to effectively reduce the detent force without sacrificing the back-EMF and average electromagnetic force, especially with respect to Modular II.

ACKNOWLEDGMENT

REFERENCES

[1] O. Farrok, M. R. Islam, M. R. I. Sheikh, Y. Guo, and J. G. Zhu, "A split translator secondary stator permanent magnet linear generator for oceanic wave energy conversion," *IEEE Trans. Ind. Electron.*, vol. 65, no. 9, pp. 7600-7608, Sep. 2018.

[2] C. Zheng, C. Li, J. Pan, M. Liu, and L. Xia, "An overview of global ocean wind energy resource evaluations," *Renewable Sustain. Energy Rev.*, vol. 53, pp. 1240-1251, Jan. 2016.

[3] L. Xu, C. Zhang, and X. Zhu, "Decoupling control of a dual-stator linear and rotary permanent magnet generator for offshore joint wind and wave energy conversion system," *IET Elect. Power Appl.*, vol. 14, no. 4, pp. 561-569, Apr. 2020.

[4] L. Szabó, "On the use of rotary-linear generators in floating hybrid wind and wave energy conversion systems," *Proc. 21st IEEE Int. Conf. AQTR*, Cluj-Napoca, Romania, pp. 1-6, May 2018.

[5] J. Wang, W. Wang, K. Atallah, and D. Howe, "Design considerations for tubular flux-switching permanent magnet machines," *IEEE Trans. Magn.*, vol. 44, no. 11, pp. 4026-4032, Nov. 2008.

[6] G. Zhang, R. Nie, J. Si, C. Gan, and Y. Hu, "Optimal design of a novel double-stator linear-rotary flux-switching permanent-magnet generator for offshore wind-wave energy conversion," *Proc. IEEE Energy Convers. Congr. Expo.*, Vancouver, BC, Canada, pp. 4300-4305, Oct. 2021.

[7] R. Nie, J. Si, S. Xu, G. Zhang, Z. Li, and Z. Cheng, "Optimization of a novel linear-rotary permanent magnet generator for wind-wave combined energy conversion via TOPSIS decision making,"

Proc. 13th Int. Symp. Linear Drives for Ind. Appl., Wuhan, China, pp. 1-6, July 2021.

[8] Q. Liu, H. Yu, M. Hu, C. Liu, J. Zhang, L. Huang, and S. Zhou, "Cogging force reduction of double-sided linear flux-switching permanent magnet machine for direct drives," *IEEE Trans. Magn.*, vol. 49, no. 5, pp. 2275-2278, May 2013.

[9] S. Zhou, H. Yu, M. Hu, C. Jiang, and L. Hao, "Reduction of cogging force in a linear flux-switching permanent-magnet brushless AC machine for direct-drive applications," *IEEE Trans. Magn.*, vol. 47, no. 10, pp. 3252-3255, Oct. 2011.

[10] S. Ali, J. Ikram, C. P. Devereux, S. S. H. Bukhari, S. A. Khan, N. Khan, and J.-S. Ro, "Reduction of cogging torque in AFPM machine using elliptical-trapezoidal-shaped permanent magnet," *Applied Computational Electromagnetics Society (ACES) Journal*, vol. 36, no. 8, pp. 1090-1098, Aug. 2021.

[11] S. Amin, S. Madanzadeh, S. Khan, S. S. H. Bukhari, F. Akhtar, and J.-S. Ro, "Effect of the magnet shape on the performance of coreless axial flux permanent magnet synchronous generator," *Electrical Engineering*, vol. 104, no. 2, pp. 959-968, Apr. 2022.

[12] R. Cao, D. Shen, and W. Hua, "Research on detent force characteristics of a linear flux-switching permanent-magnet motor," *IEEE Trans. Energy Convers.*, vol. 36, no. 4, pp. 2998-3006, Dec. 2021.

[13] C.-F. Wang, J.-X. Shen, Y. Wang, L.-L. Wang, and M.-J. Jin, "A new method for reduction of detent force in permanent magnet flux-switching linear motors," *IEEE Trans. Magn.*, vol. 45, no. 6, pp. 2843-2846, June 2009.

[14] S. Wang, Y. Wang, C. Liu, G. Lei, J. Zhu, and Y. Guo, "Detent force minimization of a tubular flux-switching permanent magnet motor using un-equal width stator slots based on Taguchi method," *IEEE Trans. Appl. Supercond.*, vol. 30, no. 4, June 2020.

[15] J. Zhao, Q. Mou, K. Guo, X. Liu, J. Li, and Y. Guo, "Reduction of the detent force in a flux-switching permanent magnet linear motor," *IEEE Trans. Energy Convers.*, vol. 34, no. 3, pp. 1695-1705, Sep. 2019.

[16] B. Li, J. Zhao, X. Liu, Y. Guo, H. Hu, and J. Li, "Detent force reduction of an arc-linear permanent-magnet synchronous motor by using compensation windings," *IEEE Trans. Ind. Electron.*, vol. 64, no. 4, pp. 3001-3011, Apr. 2017.

[17] T. Yao, W. Zhao, F. Bian, L. Chen, and X. Zhu, "Design and analysis of a novel modular-stator tubular permanent-magnet Vernier motor," *IEEE Trans. Appl. Supercond.*, vol. 28, no. 3, Art. no. 0601105, Apr. 2018.

[18] X. Huang, Z. Qian, Q. Tan, J. Li, and B. Zhou, "Suppressing the thrust ripple of the permanent magnet linear synchronous motors with different pole structures by setting the modular primary structures differently," *IEEE Trans. Energy Convers.*, vol. 33, no. 4, pp. 1815-1824, Dec. 2018.

[19] J. Li, X. Huang, B. Zhou, H. Yu, and Q. Huang, "Design principle of a 16-pole 18-slot two-sectional modular permanent magnet linear synchronous motor with optimisation of its end tooth," *IET Elect. Power Appl.*, vol. 14, no.3, pp. 441-447, Mar. 2020.

[20] X. Z. Huang, J. Li, Q. Tan, Z. Y. Qian, C. Zhang, and L. Li, "Sectional combinations of the modular tubular permanent magnet linear motor and the optimization design," *IEEE Trans. Ind. Electron.*, vol. 65, no. 12, pp. 9658-9667, Dec. 2018.

[21] Q. Tan, M. Wang, L. Li, and J. Li, "Research on noninteger pole number for segmental permanent magnet linear synchronous motor," *IEEE Trans. Ind. Electron.*, vol. 68, no. 5, pp. 4120-4130, May 2021.

[22] Q. Tan, X. Huang, L. Li, and M. Wang, "Magnetic field analysis and flux barrier design for modular permanent magnet linear synchronous motor," *IEEE Trans. Ind. Electron.*, vol. 67, no. 5, pp. 3891-3900, May 2020.

[23] R. Cao, M. Cheng, and W. Hua, "Investigation and general design principle of a new series of complementary and modular linear FSPM motors," *IEEE Trans. Ind. Electron.*, vol. 60, no. 12, pp. 5436-5446, Dec. 2013.

[24] R. Cao, M. Cheng, C. C. Mi, and W. Hua, "Influence of leading design parameters on the force performance of a complementary and modular linear flux-switching permanent-magnet motor," *IEEE Trans. Ind. Electron.*, vol. 61, no. 5, pp. 2165-2175, May 2014.

[25] J. T. Chen and Z. Q. Zhu, "Winding configurations and optimal stator and rotor pole combination of flux-switching PM brushless AC machines," *IEEE Trans. Energy Convers.*, vol. 25, no. 2, pp. 293-302, June 2010.

Guozhen Zhang was born in Anhui province, China, in 1996. He received the B.S. degree in Electrical Engineering from the Henan University of Technology in 2020. He is currently working toward the M.S. degree in Electrical Engineering with the School of Electrical and Information Engineering, Zhengzhou University, Zhengzhou, China. His current research interests include the design and optimization of two-degree-of-freedom machines and linear machines.

Rui Nie received the B.S. degree in Electrical Engineering from Henan Polytechnic University, Jiaozuo, China, in 2015, and the Ph.D. degree in Electrical Engineering from the China University of Mining and Technology, Xuzhou, China, in 2020. She is currently an assistant research fellow at Zhengzhou University. Her current research interests include two-degree-of-freedom machines, linear motor design and control, and renewable energy generation technology.

Jikai Si received the B.S. degree in Electrical Engineering and Automation from the Jiaozuo Institute of Technology, Jiaozuo, China, in 1998; the M.S. degree in electrical engineering from Henan Polytechnic University, Jiaozuo, China, in 2005; and the Ph.D. degree in Power Electronics and Power Drives from the School of Information and Electrical Engineering, China University of Mining and Technology, Xuzhou, China, in 2008. He is currently a Distinguished Professor with the School of Electrical and Information Engineering, Zhengzhou University. He has authored and co-authored more than 160 technical papers in these areas. His main research interests include the theory, application, and control of the special motor. Dr. Si is a Member of the Green Motor System Professional Committee, China.

Xiaohui Feng received the B.S. degree in Electrical Engineering and automation from the Jiaozuo Institute of Technology, Jiaozuo, China, in 1998, and the M.S. degree in Electrical Engineering from Henan Polytechnic University, Jiaozuo, China, in 2004. She is currently an associate Professor with the School of Electrical Engineering, North China Institute of Science and Technology. Her main research interests include linear motor design and control, control theory, and control engineering.

Changli Wang received the M.S. degree in Software Engineering from the University of Electronic Science and Technology of China, Chengdu, China, in 2009. He is currently a senior engineer with the School of Computer Science, North China Institute of Science and Technology. His main research interests include software engineering.